Manipulating Light on Wavelength Scale

Manipulating Light on Wavelength Scale

A dissertation presented
by
Yinan Zhang
to
The School of Engineering and Applied Sciences

in partial fulfillment of the requirements
for the degree of
Doctor of Philosophy
in the subject of
Electrical Engineering

Harvard University
Cambridge, Massachusetts
December 2012

Thesis advisor: Marko Loncar Yinan Zhang

Manipulating Light on Wavelength Scale

Abstract

Light, at the length-scale on the order of its wavelength, does not simply behave as "light ray", but instead diffracts, scatters, and interferes with itself, as governed by Maxwell's equations. A profound understanding of the underlying physics has inspired the emergence of a new frontier of materials and devices in the past few decades. This thesis explores the concepts and approaches for manipulating light at the wavelength-scale in a variety of topics, including anti-reflective coatings, on-chip silicon photonics, optical microcavities and nanolasers, microwave particle accelerators, and optical nonlinearities.

In Chapter 1, an optimal tapered profile that maximizes light transmission between two media with different refractive indices is derived from analytical theory and numerical modeling. A broadband wide-angle anti-reflective coating at the air/silicon interface is designed for the application of photovoltaics.

In Chapter 2, a reverse design method for realizing arbitrary on-chip optical filters is demonstrated using an analytical solution derived from Chapter 1. Example designs are experimentally verified on a CMOS-compatible silicon-on-insulator (SOI) platform. Among this device's many potential applications, the use for ultrafast on-chip pulse shaping is highlighted and numerically demonstrated.

In Chapter 3, the concept of tapering is applied to the design of photonic crystal cavities. As a result, the scattering losses of cavities are suppressed, and light can be localized in a wavelength-scale volume for a long life-time.

In Chapter 4, photonic crystal cavity-based nanolasers with low power consumption are demonstrated with two different prototypes -photonic crystal nanobeams and photonic crystal disks. The use of graphene is also explored in this chapter for the purpose of electrically-driven nanoscale light-emitting devices.

In Chapter 5, photonic crystal cavities at millimeter wavelength for particle acceleration applications are developed.

In Chapter 6, a novel design of dual-polarized mode photonic crystal cavities, and its potential for difference-frequency generations are examined.

Contents

Included publications

Chapter 1 includes:

Y. Zhang, C. Li, M. Loncar, "Optimal broadband anti-reflective taper," *Optics Letters* Vol. 38, pp. 646 (2013)

Chapter 2 includes:

I. Frank*, Y. Zhang*, M. Loncar, "Arbitrary on-chip optical filters for ultrafast pulse shaping," in preparation to submission (2013) (*Equal contribution to the work)

Chapter 3 includes:

Y. Zhang, M. Loncar, "Submicrometer diameter micropillar cavities with high Quality factors and ultrasmall mode volumes," *Optics Letters*, Vol. 34, 902 (2009) [Selected for the April 27, 2009 issue of *the Virtual Journal of Nanoscale Science and Technology*]

Y. Zhang, M. Loncar, "Design and simulation of nanowire-based high Quality factor nanocavities," *Proc. SPIE*, Vol. 7223, 72230W (2009)

Y. Zhang, M. Loncar, "Ultra-high quality factor optical resonators based on semiconductor nanowires," *Optics Express*, Vol. 16, pp. 17400-17409 (2008)

Chapter 4 includes:

Y. Zhang, M. Loncar, "Photonic crystal lasers," in Alexei Baranov and Eric Tournie, *Semiconductor lasers: fundamentals and applications*, Cambridge, Woodhead Publishing (2012).

Y. Zhang, M. Khan, Y. Huang, J. H. Ryou, P. B. Deotare, R. Dupuis, M. Loncar, "Photonic crystal nanobeam lasers," *Applied Physics Letters*, Vol. 97, 051104 (2010) [Selected for the August 16, 2010 issue of the Virtual Journal of Nanoscale Science and Technology]

Y. Zhang, C. Hamsen, J. T. Choy, Y. Huang, J. H. Ryou, R. Dupuis, M. Loncar, "Photonic crystal disk lasers," *Optics Letters*, Vol. 36, pp. 2704-2706 (2011)

Chapter 5 includes:

Y. Zhang, I. Bulu, T. Botto, W. M. Tam, B. Levitt, M. Loncar, "High Q/V air-mode photonic crystal cavities at microwave frequencies," *Optics Express*, Vol. 19, pp. 9371-9377 (2011)

Chapter 6 includes:

Y. Zhang, M. W. McCutcheon and M. Loncar, "Ultra-high-Q dual-polarized photonic crystal nanocavities," *Optics Letters*, Vol. 34, 2694 (2009) [Selected for the September 28, 2009 issue of *the Virtual Journal of Nanoscale Science and Technology*]

I. B. Burgess*, Y. Zhang*, M. W. McCutcheon*, A. W. Rodriguez, J. Bravo-Abad, S. G. Johnson, and M. Loncar, "Efficient terahertz generation in triply resonant nonlinear photonic crystal microcavities," *Optics Letters*, Vol. 17, 20099 (2009) (*Equal contribution to the work)

Listing of figures

To my mom and dad.

Acknowledgments

Today is September 2, 2012. I am typing the first few words of my doctoral thesis; a gleam of late-summer sunshine, calm and serene, illuminates my keyboard. I lean away from my laptop, pause, and rejoice. I cannot help but recall the first day when I arrived in Cambridge, five years ago, also a day with sunshine. I was walking around Harvard Square. An old man was playing guitar in front of Au Bon Pain, calm and serene. I stopped in the midst of the pedestrian flow, paused, and rejoiced. In reflection, that very moment was likely a harbinger of the five-year journey that was to follow.

I recall, the big smile Mughees had on his face, after I told him the nano-pattern he made with e-beam lithography the previous night vanished, because I decided to "wash" the sample with sonication; I recall, the truce handshake with a pat on my shoulder from Tancredi, following a heated discussion between us on designing high-Q microwave cavities; I recall, the huge hug with Birgit at eight in the morning inside the cleanroom, when I was completely powered-off after an overnight fabrication work; I recall, Edgar charting our secretive career plan on a whiteboard for the next decade, as if he were composing a music score of two orchestrated instruments.

At moments like these, I pause in the pursuit of happiness, and rejoice. For experiencing moments like these, I wake up with happiness and work with a whistle in my soul. Because of moments like these, the scientific research including this thesis becomes possible and more meaningful. Therefore, I am profoundly grateful for everyone in the past five years, who made me pause and rejoice, who

I learnt from, whom I viewed as role models, who instructed me with insight and wisdom, who did cleanroom fabrication with me shoulder-to-shoulder, whom I shared laughter and tears with, whom I could speak straightforwardly to without being judged. These people are my advisor, my professors, my mentors, my colleagues, my friends, and my family, whom I thank here.

I thank Marko Loncar, my advisor.

Marko offered me an opportunity that I will treasure for a lifetime. I still remember the day when I first spoke to Marko, I was at my home in Beijing watching a football game. Real Madrid was leading, the phone rang, my mom picked it up, and she could not understand a word on the line. "Probably it was for you," she told me. In five seconds, I realized the call was a phone interview with Marko. It was one of the few moments in my life I was petrified (or "stoned"). I quickly went through the formulation of Maxwell Equations three times in my head (which was the only scientific information I could remember at that moment). Fortunately, Marko did not test my scientific knowledge at all. Instead, he told me what his research interests were, and kindly invited me to come to Harvard. I did not understand much about the research part, but I did not hesitate long in accepting the Harvard offer. Growing up in a middle-class Chinese academic family, I had little freedom of choice anyway. If I said no to Harvard, my grandparents would probably kill me.

Marko has invested invaluably hard work in mentoring me, which I really appreciate. I am not a conventional Asian student: not very low-key, and difficult to be micro-managed; on the other hand, I have inherited the Asian nature of showing complete deference to professors. Even right now, I am still intimidated to open my mouth when meeting with Marko. Additionally, I had almost no experience in scientific research when I joined the group. Hence, from every perspective, it does not seem to be a simple job to instruct a student like myself. But Marko has been consistently passionate about and devoted to my research and me, despite his insanely busy schedule. He has thrown a million ideas at me, and realizing a tiny portion of them has been sufficient to graduate. He has always had faith in me,

even when things were not going well for an extended period of time. He never allowed me to be concerned about financial support. "Just go and do it," was his motto. And, moreover, he left room for me to learn, to grow, and to mellow, as a scientist.

I also thank Marko for being an exemplary group manager. He recruited a fabulous "first-generation" team, and I was honored to be one of them. We joined the group with diverse backgrounds, started the lab from scratch, and worked hard (many times, I found the entire CNS cleanroom occupied by the Loncar group), all inspired by Marko who worked harder than any of us.

I thank the entire Loncar group, a group that never lacks for positive dynamics, close collaborations, and great friendships. And within the group, specially,

I thank Mughees Khan, who did e-beam lithography for the photonic crystal nanobeam laser project. Mughees taught me all the fabrication techniques, hand-by-hand, when I started as a rookie. I will never forget his patience with all my amateur mistakes, being a fabrication guru himself. Mughees is an extremely humble person, which makes him my role model.

I thank Irfan Bulu, who collaborated with me in the microwave high-Q cavity project. Irfan was my first officemate, and taught me to perform FDTD simulations. Irfan is one of those rare people, who derive purely joy from solving a quantum optics problem with pencil and paper on a Saturday afternoon, with the aid of three Diet Cokes, of course. Irfan has also given me many valuable pieces of advice on becoming a quality scientist, which he most certainly is.

I thank Murray McCutcheon, who co-authored five academic papers with me, and taught me a great deal about nonlinear optics. Additionally, Murray is my role model of professional ethics. Murray once told me that he rejected an invitation to co-author a paper to be published on Nature Photonics, because he was not convinced that he contributed enough to the work.

I thank Parag Deotare, who helped build and align the optical setup for testing the nanolasers. Moreover, he is the one, whom I bothered the most for help in

debugging problems in my research. He has been like an academic elder brother to me. We also went to many conference trips together, in California, in Sydney, and in Spain, with many good memories brought back as souvenirs. I am sure he will be a brilliant professor in the near future, because he is already brilliant.

I thank Raji Shankar, an encyclopedia of knowledge. I have learnt a lot from Raji, with knowledge ranging from mid-infrared silicon photonics to geography, Shakespeare English, British politics, and many other "irrelevant" fields. Raji has also been a very generous and faithful friend from the very first time I met her, freely sharing her judgment and wisdom with me. Our friendship, like a support group, has carried us through ups and downs in our respective PhDs. And together through this friendship, we have seen each other grow up.

I thank Jennifer Choy. To me, Jen is beyond a diligent and competent scientist. I knew Jen before she joined the group, and ever since then, I have been worshiping her unmatched kindness, her extreme humility, and her altruism. Blessed with such virtues, Jen has made people around her, including me, be blessed through her.

I thank Birgit Hausmann. Many moments I spent with Birgit, reminded me of the movie "Le fabuleux destin d'Amélie Poulain", a movie we both like a lot. The innocent joy of life, which she has brought to my and many others' lives, is forever treasured. The pursuit of PhD is not always like being in a comedic movie though. There were also some rainy days, and even tsunamis. When a tsunami took place in my life, Birgit was there, helping me overcome the storm, lending me a shelter, and delivering her Amélie optimism to me, for which I cannot thank her enough.

I thank Ian Frank, who is currently collaborating with me on the programmable integrated filter project. Every time we have a discussion, Ian can grasp my point from the first sentence, which makes our meeting never last long. To me, it has always been a pleasure to sit next to a colleague like Ian, who is much smarter than me.

I thank Thomas Babinec. Tom and I worked together on the diamond nanowire project. I am also grateful for his efforts in organizing the lab, when the lab just started up. In addition, Tom was one of my guides to American culture.

I thank Ian Burgess, a prodigy, who worked together with me on the TE/TM dual-polarized cavity project. We have also collaborated on developing high-Q cavities based on low-index polymers. I have admired Ian from the beginning. As a young graduate student, he published like Virgil, assembled a team like Scipio, and presented his results like Cicero. I was convinced he was able to start his own group before he graduated.

I thank Haig Atikian. Haig and I have been working together on the graphene-contacted microdisk project for the past two years. He has demonstrated a wide spectrum of expertise, spanning electronics and photonics. When he started his PhD, he already had more experience than most of the senior PhD graduates, including me. I also thank him to be a really fun person, as a colleague and as a friend.

I thank Mehmet Dundar, Christoph Hamsen, Eric Graves, and Changlin Li, who have worked closely with me, as research interns. Mehmet, a good friend of mine, helped with e-beam lithography for making nanobeam cavities. Unfortunately we did not produce results by the time he left. Chris was a catalyst for the graphene-contacted microdisk project, as well as a catalyst for me to grow up. Eric helped transfer graphene films on semiconductor chips. Changlin provided some valuable positive feedback to the theory of broadband anti-reflective coatings.

I would also like to thank many people outside the group. Without their support and help, this thesis would not become possible.

Prof. Russell Dupuis (Georgia Institute of Technology) and his students Yong Huang and Jae-Hyun Ryou helped grow the III-V semiconductor quantum well wafers for the nanolasers.

Tancredi Botto (Schlumberger Doll Research Center) was a close collaborator on the microwave high-Q cavity project. He is a serious engineer I truly respect, and has also offered me a lot of personal guidance, inside and outside the project. I am also a big fan of his straightforwardness. Wai-Ming Tam and Ben Levitt at the same institute also provided assistance in measuring the device.

Prof. Jing Kong (MIT) and her students Yi Song and Hyesung Park helped grow

and transfer graphene films for the graphene-contacted microdisk project. They have also provided much constructive advice on my research.

Prof. Steven Johnson (MIT), Alexandro Rodriguez, and Jorge Bravo-Abad helped develop the nonlinear optics theory based on the TE/TM dual-polarized cavities.

Prof. Vladimir Bulovic (MIT) offered his valuable insight on the high-Q micropillar cavity project, for its applications to coupling to J-aggregate polymer.

Prof. Federico Capasso (Harvard) kindly allowed us the use of his spectrometer for testing the photonic crystal disk lasers.

Again, I thank Prof. Federico Capasso, Prof. Vladimir Bulovic, and Prof. Michael Aziz to serve on my thesis committee, and for providing useful advice.

Most of the devices in the thesis have been fabricated at Harvard Center for Nanoscale Systems (CNS). I would like to acknowledge the support provided by Harvard CNS staff -Jiangdong Deng (JD), Steve Paolini, Steven Hickman, Yuan Lu, Jason Tresback, Ling Xie, and Ed Macomber.

The work in this thesis was financially supported, in part by the National Science Foundation (NSF) grant, and the NSF Nanoscale Science and Engineering Center at Harvard University. I was also supported by the Graduate Consortium on Energy and Environment Fellowship at Harvard University for one year.

Last but not least, a long list of people have supported this thesis, in very valuable ways not directly related to the scientific results.

I thank the "the family" -Edgar Barroso, Rosario Hubert, Viridiana Rios, and Nicolas Chevrier, who I met at the graduate school orientation. Since then, we have been friends, and their friendships have reshaped me, profoundly. I learnt the secret of living a meaningful and happy life, and the wisdom of oceanism from Edgar; I learnt the value of empathy with a compassionate soul, and a classy sense of humor from Rosa; I started to examine my time management, and worked more efficiently, since I worked together with Viri at the library; and Nico's attitude to life is a model to live my own life.

I need to specially thank Edgar, “the guey”, for the uncountable time we have spent together in the past five years, through which I was enlightened, in many different ways.

I thank Prof. Arakawa, Prof. Iwamoto, Yasutomo Ota (Tokyo University), Prof. Baba (Yokohama National University), and Prof. Xue Feng (Tsinghua University), who have invited me to present my work to their group, and have given me useful advice on my thesis project.

I thank Mikhail Kats (Capasso group, Harvard), whose enthusiasm and devotion in science have consistently inspired me.

I thank Jonathan Lee (Hu group, Harvard), who offered me a great amount of moral support and encouragement with his loyal friendship, and urged me to finish my thesis before it was too late.

I thank many other friends at Harvard, Daniel Floyd, Daniel Ramos, Michael Burek, Ray (Jia Hong) Ng, Kirsten Smith, Dongwan Ha, Fatih Degirmenci, Nan Niu, John Joo, and Vikas Lonakadi. I also thank the following people, Chong Liu, Yuan Yang, Ji Cheng, Guan Pang, Xi Chen, and Chenhui Li, with whom I have been friends since high school.

I thank Uncle Peter who has given me lots of life and career advice as a mentor to me, and who has also invited me to many gourmet meals.

I thank Mrs. Tam for her kindness in providing nutritional supplies across the Pacific Ocean.

Finally, I thank my family -my grandpa and grandma, my uncles and aunts, my cousins, and last,

I thank my mom and dad, to whom this thesis is dedicated.

He who knows the truth is not equal to him who loves it; he who loves it is not equal to him who delights in it.

Confucius, *the Analects*

1

Optimal taper for impedance matching

1.1 Introduction to impedance matching

When a wave travels from one medium into another, a portion of the power is reflected because of impedance mismatch. This is a familiar concept in disciplines as diverse as electromagnetism, acoustics, and seismology. Minimizing the reflectance caused by impedance mismatch is therefore an extremely important issue in many fields: anti-reflective coatings are used on lenses (ranging from eyeglasses to telescopes); impedance matching in electrical transmission lines maximizes the power transfer between the source and the load [1]; microwave anti-reflective components are used in concealing military targets from radar detection as well as in construction of anechoic chambers for antenna measurements [2]; in acoustics, horns and megaphones amplify the sound coupling of human voice or

musical instruments to open space.

The impedance-matching components in general can be realized with the aid of interference. The quarter-wave coating on optical lenses offers a classic example: a single-layer coating with a thickness of one-quarter wavelength of light minimizes reflection of that particular wavelength (λ) by canceling out reflection from the front and the back of the coating [3]. The quarter-wave impedance transformer used in transmission line employs the same mechanism. However, such interference-based devices, by their nature, only operate within a narrow bandwidth, and in the case of optics over limited range of incident angles.

In contrast, a broadband impedance-matching component can be achieved by adiabatically coupling the wave from one medium to another through a graded-impedance taper. The tapered layer whose impedance varies continuously can be realized by a textured interface. When the feature size of the structured interface is much smaller than the wavelength, the effective impedance of the blended medium is determined by the weighted average of the impedance of the two media [4]. Such structured interface has been inspired by natural biological organisms (e.g. dragonfly wings, moth eyes) [5–8], and has been fabricated with different nanofabrication technologies, including focused ion beam [9], dry etching with self-assembled mask [10], colloidal lithography [11] and interference lithography [12], and nanoimprint from bio-template [13].

The performance of the taper is dependent on its tapered length (l), as well as the tapered impedance profile [14–17]. As the tapered length increases with respect to λ, reflection can be reduced because of the smoother adiabatic conversion. However, in practical realization, the tapered length is often limited by fabrication and/or other implementation constraints.

In this section, we seek the optimal impedance profile, which minimizes the reflectance across a broad frequency band for a given taper length. While we focus on the applications in optics, our approach is general and the results are applicable to a wide class of physical phenomena that involve wave propagation. For example, this work could lead to a significant improvement of performance in stealth technology, and photovoltaics [11, 18].

1.2 Derivation of Maxwell's equations

The behavior of electromagnetic wave propagating inside a medium with varied index can be described by 1D Maxwell's equations,

$$\begin{cases} -\dfrac{\partial}{\partial x}E(x,t) = \mu(x)\dfrac{\partial}{\partial t}H(x,t) \\ \\ -\dfrac{\partial}{\partial x}H(x,t) = \varepsilon(x)\dfrac{\partial}{\partial t}E(x,t) \end{cases} \tag{1.1}$$

where E and H are the electric and magnetic components and μ and ε are the medium permeability and permittivity. The telegrapher's equations of transmission lines and acoustic equations follow the same form. In an electrical transmission line, E and H are replaced by voltage V and current I respectively, while μ and ε are replaced by characteristic inductance L_0 and capacitance C_0 respectively. In acoustic theory E and H are replaced by acoustic pressure p and the acoustic fluid velocity vector v respectively, while μ and ε are replaced by mass density ρ and the inverse of bulk modulus κ^{-1} respectively.

For further insight into Eq. 1.1, we perform the following normalization: we define the optical length of the tapered section to be $L = \int_0^l n(x)dx$, where $n(x)$ is the material's refractive index. Next, we normalize the x-axis with respect to its optical length. The normalized unit $u \in [0, 1]$ is defined by

$$u = \frac{1}{L}\int_0^x n(x')dx' \tag{1.2}$$

With this normalized unit u, Eq. 1.1 (in the time-harmonic form) can be rewritten as,

$$\begin{cases} \dfrac{dE}{du} = i2\pi\dfrac{L}{\lambda}Z(u)H(u) \\ \\ \dfrac{dH}{du} = i2\pi\dfrac{L}{\lambda}\dfrac{1}{Z(u)}E(u) \end{cases} \tag{1.3}$$

where $Z = \sqrt{\mu/\varepsilon}$ is the material impedance. From Eq. 1.3, the electromagnetic wave can be separated into a forward propagating wave and a backward propagating wave with a coefficient r,

$$\begin{cases} E(u) = A[\exp(i2\pi\frac{L}{\lambda}u) + r\exp(-i2\pi\frac{L}{\lambda}u)] \\ \\ H(u) = \frac{A}{Z}[\exp(i2\pi\frac{L}{\lambda}u) - r\exp(-i2\pi\frac{L}{\lambda}u)] \end{cases} \tag{1.4}$$

Importantly, $r(0)$ describes the percentage of light in amplitude that reflects off from the $u = 0$ interface, and $r(1) = 0$ because we assume there is no backward propagating light incident from $u = 1$ interface.

From Eq. 1.4 we can derive

$$r(u) = \frac{E(u) - Z(u)H(u)}{E(u) + Z(u)H(u)} \tag{1.5}$$

Combining Eq. 1.3 and Eq. 1.5 leads to a nonlinear ordinary differential equation of $r(u)$.

$$r' + i4\pi\frac{L}{\lambda}r = -\frac{1}{2}(1 - r^2)p(u) \tag{1.6}$$

where $p = d\ln Z/du$ contains the information of the taper profile.

The goal is to find the optimal taper function $p(u)$ that results in minimal $r(0)$, given a certain bandwidth $[\lambda_{\min}, \lambda_{\max}]$. First, we employ an approximation to solve this problem semi-analytically, and then use numerical approaches to find the exact solutions. For a small r, using an approximation $r^2 \ll 1$, Eq. 1.6 can be reduced to a linear ordinary differential equation, which has the exact solution,

$$r(0) = \frac{1}{2}\int_0^1 p(u')\exp(i4\pi\frac{L}{\lambda}u')du' \tag{1.7}$$

Note that Eq. 1.7 is equivalent to Fourier transform (FT),

$$r(0) = \frac{1}{2}P(2L/\lambda) \tag{1.8}$$

where $P(u)$ is the Fourier transform of $p(u)$, and $2L/\lambda$ corresponds to the frequency of the Fourier transform. It is important to note that $P(0)$ is constrained to constant for any tapered function $p(u)$.

$$P(0) = \int_0^1 p(u')du' = \ln Z_2 - \ln Z_1 \tag{1.9}$$

where Z_1 and Z_2 are the impedance of the two media. This is because $P(0)$ approximates the reflection between the two media without taper.

Therefore the problem of finding the optimal taper profile that has minimum reflectance at bandwidth $[\lambda_{\min}, \lambda_{\max}]$ given the optical length L, is equivalent to finding the optimal window function $p(u)$, confined within $[0, 1]$, whose Fourier transform's sideband level R^* above cutoff frequency $f_c = L/\lambda_{\max}$ is minimal. $R^*(f_c)$ is defined as,

$$R^*(f_c) = \max\{|\frac{P(f)}{P(0)}|_{f>f_c}\} \tag{1.10}$$

1.3 Optimal taper function

Interestingly, the above-mentioned problem is analogous to the side-lobe suppression problem in signal-processing in order to minimize so-called "spectrum leaks" of digital signals that result in the cross-talk between different frequency bands [19]. Among the many window functions utilized in signal-processing, the Dolph-Chebyshev window function satisfies the above-mentioned requirements for $p(u)$: it minimizes the sideband level $R^*(f_c)$ for given cutoff frequency f_c [20]. Historically, Dolph-Chebyshev window has been used to optimize the directionality of phase antenna [20], and to design tapered section in electrical transmission line (Klopfenstein taper) [22]. In the latter case, the refractive index has been treated as constant throughout the tapering, which is only valid for TEM mode in co-axial metal waveguide. Here, we provide a generalized model for designing broadband anti-reflective device.

In Fig. 1.3.1 we compare different tapering profiles $\log Z(u)$, their respective

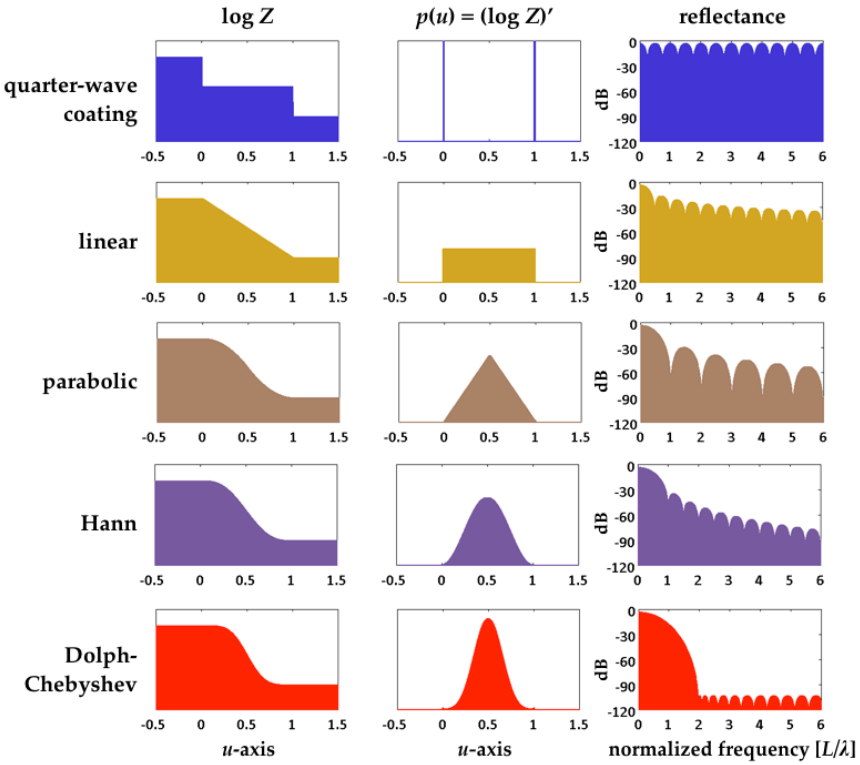

Figure 1.3.1: Comparison of different window functions $p(u)$ [21] for anti-reflective coatings at silicon/air interface, and their respective reflectance $R = |r(0)|^2$ predicted by the Fourier model.

window functions $p(u)$, and their reflectance spectra (in decibels). As a concrete example, we choose to maximize the transmission (minimize the reflection) between air ($n = 1$) and silicon ($n = 3.5$). In the case of a quarter-wave coating, the step function in the impedance profile results in two Dirac delta functions with a spacing of unity in $p(u)$. Its Fourier transform is the result of beating between two constant-amplitude functions with a frequency difference, leading to zero reflectance at $L/\lambda = 1/4 + m/2$ for $m \in \mathbb{N}$, which is consistent with the phenomenon in quarter-wave coating. At all other frequencies where this condition is not satisfied, the reflectance level remains high (30%, -5dB).

On the other hand, when tapering is applied, for example, reflectance side-lobes can be suppressed over a wide normalized frequency range (the height of the main

lobe remains the same as in the previous case). In addition, for all tapering profiles except for the Dolph-Chebyshev one, the height of the side-lobes decreases as the normalized frequency increases. This is expected since for given wavelength of incident wave, larger normalized frequencies mean longer structure with more adiabatic tapering. The Dolph-Chebyshev taper, specially, can have significantly smaller and frequency-independent side-lobes R_{sb}. As an example, in Fig. 1.3.1 we plot a Dolph-Chebyshev function that is optimized for a cutoff frequency of $L/\lambda_{\max} = 2$ and has a sideband reflectance of $R_{sb} = -105$dB.

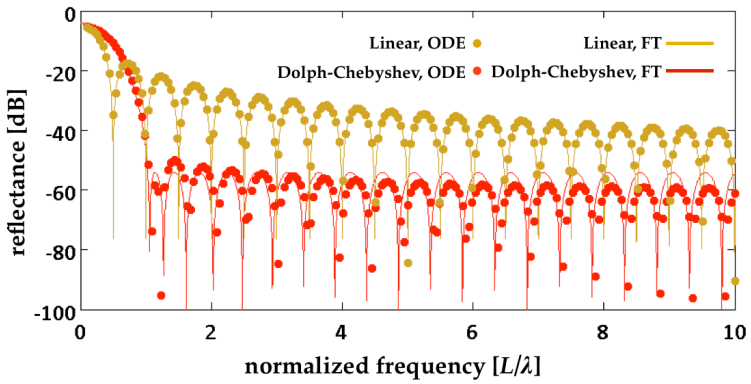

Figure 1.3.2: Comparison of power reflectance between that predicted by the Fourier model and that calculated by solving Maxwell's Equations. The Dolph-Chebyshev function in this Figure is optmized for a cutoff frequency of $L/\lambda_{\max} = 1$ and has a sideband reflectance of $R_{sb} = -55$dB.

1.4 Design and performance

Having identified Dolph-Chebyshev tapering profile as the most promising one, in Fig. 1.3.2 we evaluate the validity of our modeling. We compare the analytical solution predicted by the Fourier model (with the r^2 approximation in Eq. 1.6), with the numerical solution to Eq. 1.6. In Fig. 1.3.2, the result derived from the Fourier transform is plotted in solid line, while that produced by numeric solution is plotted in dots. Here, different from the one in Fig. 1.3.1, the Dolph-Chebyshev

function is optmized for a cutoff frequency of $L/\lambda_{\max} = 1$ and has a sideband reflectance of $R_{sb} = -55$dB. Fig. 1.3.2 shows that the Fourier model prediction is in excellent agreement with the simulation.

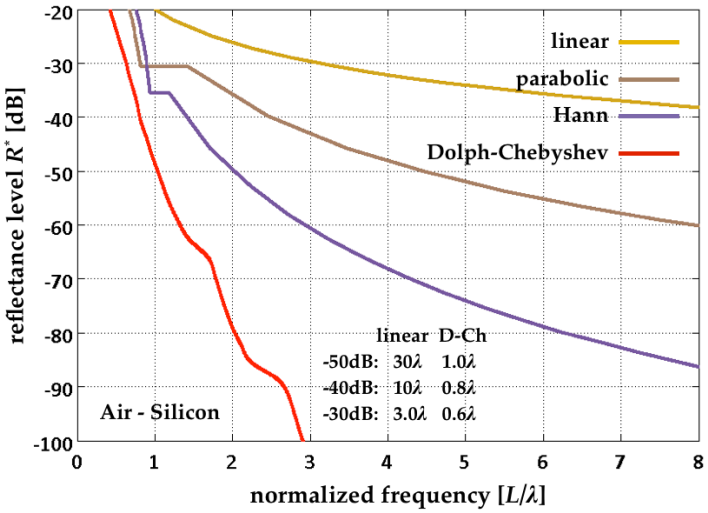

Figure 1.4.1: Comparison of different taper functions' performance, for silicon/air interface as an example.

Next, in Fig. 1.4.1 we compare the reflectance level $R^*(f_c)$ of Dolph-Chebyshev taper to other taper functions, calculated with numerical solution. It can be seen that the Dolph-Chebyshev taper outperforms the other impedance profiles. The difference in performance becomes increasingly dramatic as desired R^* decreases. For example, in order to reach a reflectance level of -50dB, implementing with a linear taper requires an optical length L longer than 30λ; the same reflectance can be achieved with a Dolph-Chebyshev taper of an optical length L of only 1.0λ.

Finally, we provide an example of a broadband wide-angle anti-reflective coating with Dolph-Chebyshev taper using our theory. We aim to minimizing the reflection loss between air and silicon across the solar spectrum from 300nm to 2000nm, with $R^* = -48$dB at normal incidence. We choose $L = 2.4\lambda_{\max} = 4.7\mu$m to satisfy this condition, which results in a coating thickness of $l = 2.8\mu$m. Fig. 1.4.2

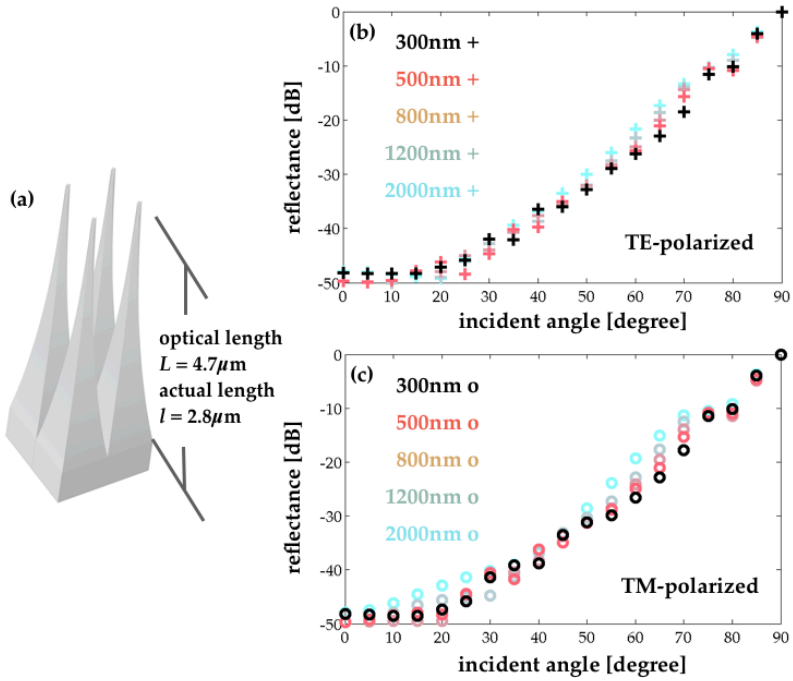

Figure 1.4.2: Example of a broadband wide-angle anti-reflective coating between air and silicon. (b)(c) Reflectance dependence on incident angle, at different wavelengths across the solar spectrum, for TE-and TM-polarized light.

shows the reflectance spectra as a function of the incident angle at different wavelengths, for TE-and TM-polarized light respectively. The result is obtained with finite-difference time-domain method (FDTD) code. As shown in Fig. 4, our design not only demonstrates high anti-reflective property at different wavelengths, as expected, but also performs well within a large incident angle range [17]. The power loss from reflectance can remain below 1% within an incident angle of 60^o across the entire solar spectrum for both polarizations.

In summary, starting with 1D Maxwell equations, we found semi-analytical solution of the optimal taper function, that minimizes the impedance mismatch (reflection) between two materials that light propagate in. We have demonstrated that Dolph-Chebyshev taper can achieve the same anti-reflective performance with a much shorter cones, compared with other taper functions. We believe this

work will shed light on designs of broadband anti-reflective components in various areas.

2

Arbitrary on-chip optical filters for ultrafast pulse shaping

Ever since discovering that pigmentation allowed selective reflection of colors from a surface, humankind has been actively developing new ways of controlling the wavelength and direction of reflected light. People have strived for increasingly finer control over light using anything from mirrors to photographic filters. The advent of photonic band-gap materials enabled the implementation of structural color as in the scales of a butterfly's wings [23]. Additional fields such as plasmonics and metamaterials [24, 25], alongside photonic band-gap materials, provide general rules for designing structural color but often require heavy computation in order to achieve precise wavelengths; even then there lacks sufficient flexibility that allows for arbitrary filter response. We present a method

for easily designing a structure that will reflect an arbitrary spectrum. While this method can be generally applied to any structure where the refractive index profile can be controlled, we have concentrated on implementing arbitrary reflective filters in compact, on-chip waveguides. These integrated filters have myriad applications from on-chip signal routing to compact, ultra-fast pulse shaping [26].

In our recent work we have studied a region with a refractive index modulation in one dimension [27] and derived the Fourier transform relationship between the reflectance spectrum and the refractive index profile. We show here that this principle can also be extended to optical waveguides on the SOI platform, where the refractive index profile is represented by the SOI waveguide-mode's (fundamental TE_{oo} mode) effective index. The modulation of the effective index is controlled by the variation in the width of the silicon waveguide $[W(x)]$.

We previously detailed [27] the derivation of the ordinary differential equation that describes the reflection coefficient, r, as a function of the index modulation $[n(x)]$ in time harmonic form. Eq. 2.1 shows a variation on this result,

$$r(\lambda) = \frac{1}{2} J(\lambda) \int_o^l \frac{dW}{dx} \exp(i2\pi \frac{2n_{eff}}{\lambda} x) dx \tag{2.1}$$

where $J(\lambda) = -\frac{1}{n_{eff}} \frac{dn_{eff}}{dW}$ takes into account the wavelength dispersion of the optical waveguide as well as the material dispersion. The former dispersion is calculated through an eigenfrequency analysis of the waveguide's cross-section. The integration in Eq. 2.1 is performed over the length of the width-modulated region of the waveguide. Note that Eq. 2.1 is of the form of a Fourier transform. (The integration limits can be extended to infinity as the integrand evaluates to zero everywhere outside the width modulated region.) This gives us a powerful method for solving for $W(x)$ -from a target $r(\lambda)$ spectrum -simply by inverting the Fourier transform. Fig. 2.0.1(c)(d) show a target spectrum and the corresponding width profile, and Fig. 2.0.1(b) shows the SEM micrograph of the width-modulation profile realized on the SOI platform.

It is important to note that Eq. 2.1 is only an approximate solution -its derivation relies upon small amplitudes of the reflection coefficient -and the target $r(\lambda)$

spectra are not exactly reproduced. The efficacy of the method can be tested by solving the exact Maxwell's equations numerically. As expected, our reverse design method's results start to diverge from the target spectra as the magnitude of r increases. Fig. 2.0.1(e) shows this trend and extends the target spectra into non-physical values greater than unity.

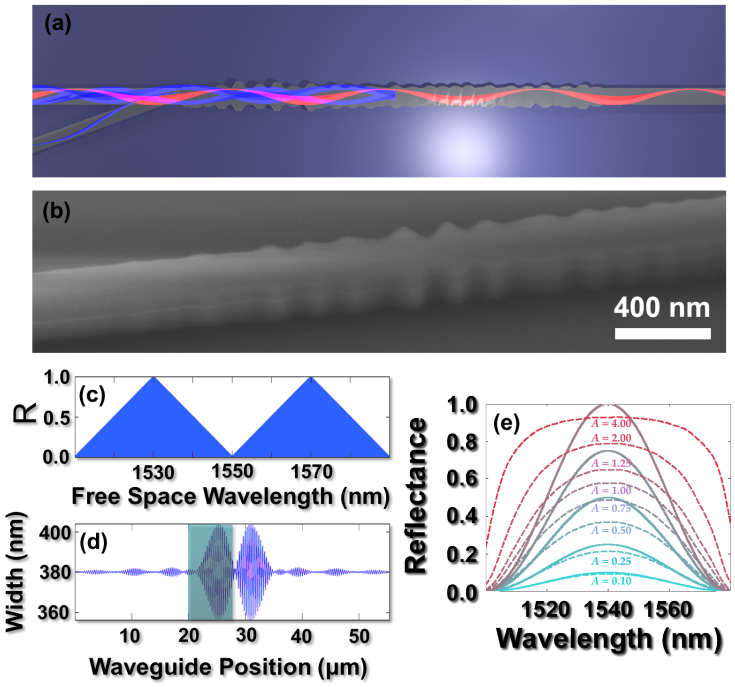

Figure 2.0.1: (a) A cartoon representation of the filter in action. The red light is transmitted through the width modulated region, whereas the blue light is reflected back. (b) An SEM micrograph of a fabricated waveguide showing the $W(x)$ profile. (c) An example target $R(\lambda)$. (d) The width profile $W(x)$ that is obtained by applying the inverse Fourier transform obtained from Eq. 2.1 to the spectrum from (c). (e) The solid lines are target amplitudes of labeled values A. The dashed lines show the resulting reflectance when the $W(x)$ profile is checked by solving the exact Maxwell's equations numerically. For small values of A the agreement is excellent, but increasingly larger values lead to distortion of the shape and discrepancies in the amplitude.

When transferring a continuous modulation of a waveguide width onto an SOI sample through electron-beam (e-beam) lithography, two problems occur. First, due to the finite length of the filter there is a truncation effect: if an r spectrum with large 'tails' in its Fourier transform is chosen, there will be significant degradation in the resulting spectrum because a large proportion of the Fourier components will be lost. Second, errors arise from the finite resolution of e-beam lithography. This leads to a washing out of the finer features in the r spectrum. Viewed through the prism of classical digital signal processing, these two issues would be equivalent to not sampling the data for a sufficiently long period in the time domain, and to obtaining an analog to digital conversion with insufficient bits to properly resolve the amplitude of the signal.

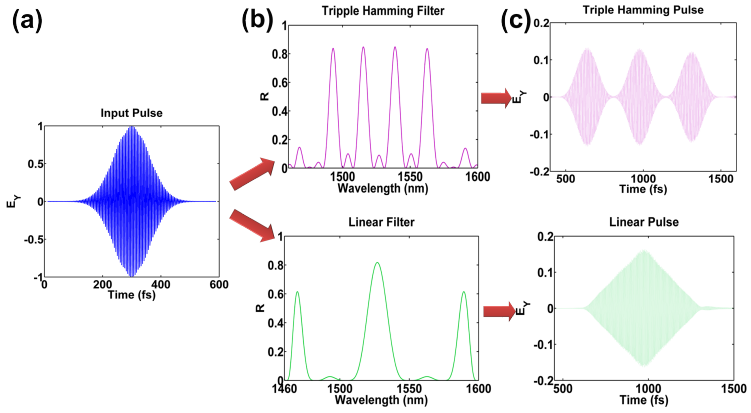

Figure 2.0.2: (a) Time domain Gaussian input pulse. (b) The wavelength domain reflectance filter shapes. Eq. 2.1 is used turn these filter shapes into $W(x)$ for the waveguides. (c) Time domain readout of the input pulse reflected off the filters. The results are a Hamming and linear pulse shape, respectively.

An important application for this method is in shaping ultra-fast pulses. Bulky apparatus is currently used for ultra-fast shaping, and it requires precision alignment [28, 29]. By using the SOI waveguide platform our filters allow us to generate arbitrary pulse shapes in an integrated, on-chip fashion. The small footprint of the filters additionally permits a single external pulse to excite many different

pulse shapes in parallel. The key to pulse shaping is the control of amplitude and phase over a wide wavelength range [30]. As Eq. 2.1 solves for r (the reflection coefficient) rather than R (the reflectance, or $|r|^2$), the necessary conditions for ultra-fast pulse shaping are met.

We now present finite difference time domain simulations showing a single Gaussian pulse is launched into two different width-modulated SOI waveguides, and is converted into three distinct Hamming pulses, and a linear (saw-tooth) pulse, respectively. Fig. 2.0.2 shows the time domain representation of the input and the two simulated reflected pulses. All simulations are three dimensional with the mesh grid size of 1nm, which is similar to the e-beam lithography resolution available to us.

For experimental demonstration, we have selected five arbitrary spectra, as shown in Fig. 2.0.3(b). The spectra were subsequently translated to different waveguides' width modulation shapes $[W(x)]$ using Eq. 2.1 . The devices were fabricated on SOI wafers (SOITEC) with a 220 nm device layer and a 2 μm buried oxide layer. The waveguides were written using a negative resist (XR 1541-6%) and 100 kV electron-beam lithography (Elionix 7000). The exposure window was a 300 μm square with a dot-pitch of 1.25 nm. After development (TMAH 2.5%) the pattern was transferred to the device layer using reactive-ion etching (C_4F_8 and SF_6). SU-8 Polymer waveguides were defined using e-beam lithography for spot size conversion. Finally, the device was capped using PE-CVD deposited silicon dioxide to enable facet polishing. Fig. 2.0.3(a) shows an SEM micrograph of an example device prior to PE-CVD deposition.

Filter characterization was performed with a scanned tunable laser (Agilent 81682). Light was coupled onto the chip through a tapered, lensed fiber (Oz optics). An on-chip, 3dB directional coupler was used to extract the reflected signal to an output arm and back to an SU-8 waveguide as depicted in Fig. 2.0.3(a). Fig. 2.0.3(b) and (c) show example target spectra alongside experimentally measured spectra; the agreement between the two is excellent. The signal can be distorted by Fabry-Perot resonances in the system as well as truncation effects due

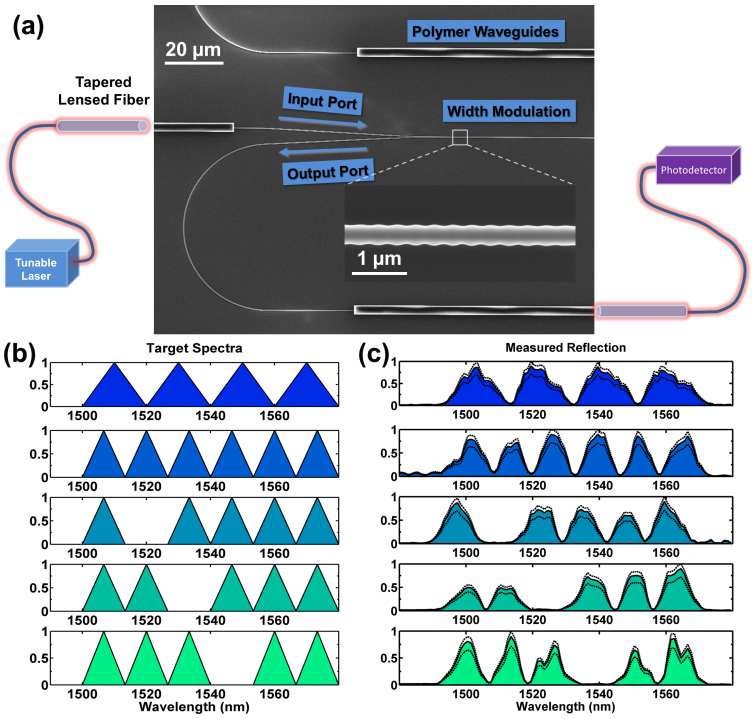

Figure 2.0.3: (a) SEM micrograph of example device; the inset shows a magnification of the width modulated region. Cartoons show flow of experiment. (b) A set of five target spectra. The intensity is in a linear saw-tooth pattern. (c) Normalized, measured reflections from fabricated devices. The dashed lines indicate the uncertainty in the normalization.

to the finite size and resolution of the width-modulated filters. The absolute values of measured reflectance are based on average values for transmission through un-modulated waveguides with the uncertainty in the measurement arising from variations in the polymer waveguide facets and insertion and extraction losses that arise from this coupling method.

In conclusion, we have demonstrated a reverse method for designing arbitrary filters with the footprint of an on-chip waveguide. In addition to allowing the design of arbitrary phase and amplitude filters these structures show great promise in shaping ultrafast pulses as demonstrated through FDTD simulations. We believe this system provides a novel and feasible platform for control of ultra-fast pulses

with vastly improved footprints and greatly reduced experimental complexity. In the future we will look to implementing ultra-fast pulse shaping as well as using dynamic methods to define the filters.

3

Impedance matching for designing ultrahigh-Q/V nanocavities

3.1 Ultrahigh-Q/V cavities based on nanowires

3.1.1 Introduction

Semiconductor nanowires have recently emerged as novel light sources for integrated photonics. Lasers and electrically-driven light emitting diodes have been reported in various material systems (CdS, ZnO, GaN, etc) [31–35]. In all of these studies, a semiconductor nanowire is used both as the active medium and

the Fabry-Perot optical cavity; the nanowire body serves as the optical waveguide, while its end facets serve as the mirrors bounding the optical cavity. However, due to the small diameter of a nanowire, significant evanescent field exists outside the nanowire body. This reduces the reflection of the nanowire facets and introduces significant losses, thus limiting the Quality factor, Q, of the cavity to $\sim$ 500 [36–40]. In addition, the large evanescent field results in the small modal gain of the nanowire [41]. Both of these effects can increase the lasing threshold of nanowire lasers. At the same time, the Fabry-Perot nature of the optical cavity can result in multi-mode lasing, with lasing wavelengths dependent on the length of nanowire. In many applications single-wavelength emission with well-defined lasing wavelength is desired. The properties of nanowire lasers and LEDs could be improved by embedding nanowires into optical structures including photonic-crystals and race-track resonators [42], metallic gratings [43], and micro-stadium resonators [44]. However, to the best of our knowledge all previously reported structures based on nanowires had $Q \geq 1,000$.

In addition to their promise as low-threshold and high switching-speed nanolasers, semiconductor nanowires offer an attractive platform for the realization of electrically-injected, on-demand, single-photon sources. A reliable and bright source of single photons would find immediate applications in spectroscopy, quantum information processing and quantum cryptography. Solid-state version of single-photon sources based on self-assembled epitaxially-grown quantum dots (QDs) have been demonstrated in different microcavity configurations [45–47]. In all of these cases, a high Q and small mode volume (V) of the microcavity were instrumental for achieving single-photon emission. Recently, there have been several proposals to achieve electrically-driven single-photon sources based on QDs embedded within semiconductor nanowires [48–55]. However, these reports did not consider the use of an optical cavity to improve the performance of such a source.

In this work, we propose an approach to significantly improve the Q of nanowire-based optical resonators, and we demonstrate cavities with $Q = 3 \times 10^5$ and $V < 0.2(\lambda/n)^3$. Our approach is based on engineering a cavity in a one-dimensional (1D) photonic crystal (PhC) [42, 56], which is patterned around the

nanowire. We demonstrate using numerical modeling that our platform coupled with a QD is well-suited for operation in the so-called strong-coupling limit of cavity quantum electrodynamics (QED), in which there is a coherent interaction between the photons confined to the optical nanowire cavity and excitons trapped in the QD [57].

3.1.2 Improvement of nanowire reflection using photonic crystals

In this work, we consider nanowires with a refractive index $n_{wire} = 2.8$ and emission wavelength of $\lambda \approx 500$nm (e.g. CdS nanowires). However, our approach is general and applicable to different material systems. We assume a circular cross-section of our nanowires [Fig. 3.1.1(a)]. This allows us to take advantage of the radial symmetry of the system and significantly simplify the analysis. The more typical hexagonal cross-section of a nanowire is taken into account in the later section, and good agreement with our simplified model is found.

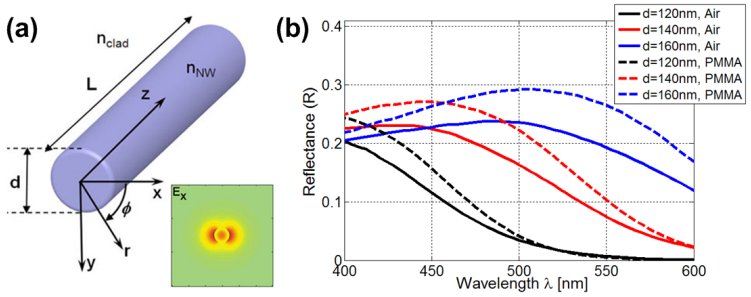

Figure 3.1.1: (a) Schematic of nanowire and mode profile (E_x components) for fundamental HE_{11} mode with $d = 120nm$ and $n_{clad} = 1$. (b) Reflectance of nanowire facets with air and PMMA cladding (HE_{11} mode).

First, we model nanowire as a cylindrical optical waveguide using Maxwell's equations in cylindrical coordinates [58, 59], considering the nanowire with air ($n_{clad} = 1$) and low-index material cladding (e.g. polymer, $n_{clad} = 1.5$). We find that nanowires with air (polymer) cladding support only the fundamental HE_{11} mode for $d < 150nm$ ($d < 160$nm). This single-mode regime of operation is precisely the region that we are interested in for this work. Next, the reflectance of

the nanowire facet was studied using the finite-difference time-domain (FDTD) method (grid size<8nm), and taking advantage of radial symmetry of the system. The fundamental HE_{11} nanowire mode is launched towards the nanowire end, and power reflected from the facet is monitored [Fig. 3.1.1(b)]. It can be seen that the nanowire facet reflectance is smaller than 25% (30%) for single-mode nanowires in air (polymer). Similar results have been found previously by other authors [37–39]. Such a poor facet reflection is responsible for large mirror losses and small quality factor ($Q \sim 500$) of the optical cavity formed by the nanowire.

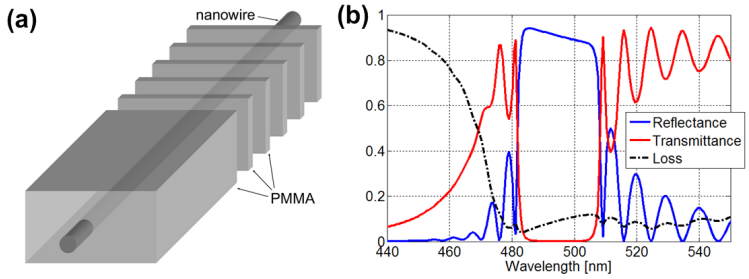

Figure 3.1.2: (a) Schematic of a semiconductor nanowire with 1D PhC defined at its end. (b) Transmittance and reflectance spectra for nanowire with PhC consisting of 30 PMMA/air pairs.

In order to increase facet reflection and overall Q of the nanowire-cavity, we consider the structure shown in Fig. 3.1.2(a) [42]. The system consists of a nanowire embedded within polymer cladding, with 1D PhC defined at the nanowire end. One particularly appealing approach is to use Poly(methyl methacrylate) (PMMA) electron-beam lithography resist as the cladding material. In this case, fabrication of the 1D PhC structure is very simple, and can be accomplished using electron-beam lithography, only.

In Fig. 3.1.2(b) we show the reflectance (R) and transmittance (T) spectra for the $d = 120$nm nanowire with a grating of periodicity $a = 160nm$. It can be seen that within the bandgap $\lambda \in (486\text{nm}, 507\text{nm})$, the reflectance can be as high as 95%, which is almost a 20-fold improvement over the facet reflection of bare nanowire. In Fig. 3.1.2(b) we also show the scattering loss, defined as $L = 1-R-T$

(absorption losses of the nanowire are neglected). This loss can be attributed to the scattering at the nanowire -1D PhC interface, due to a mismatch between the propagating fundamental HE_{11} mode inside the nanowire and the evanescent Bloch mode that exists inside the grating section [60]. In the next section we will show that this scattering loss can be significantly minimized using techniques similar to the ones developed by Lalanne and colleagues [61, 62]. Outside the bandgap, at the short-wavelength (high-frequency) end, the loss increases significantly due to coupling to the leaky modes that exist inside the mirror section (the Bloch modes of the photonic crystal cross the light line and radiate energy).

It is important to mention that the position and width of the photonic bandgap will depend strongly on the nanowire diameter. Therefore, in an experimental realization of our platform, it is important that nanowires are straight and without significant diameter variations. Sophisticated growth techniques that result in straight and uniform nanowires have recently been demonstrated [40, 51, 53, 63, 64]. Finally, we note that photonic bandgap can close when the nanowire diameter is larger than 160nm, due to the presence of higher order modes.

3.1.3 Suppressing the scattering losses by impedance matching

In this section we provide a detailed design of photonic crystal nanowire cavities taking advantage of the 1D PhC mirrors concept introduced in the previous section. We start with the Fabry-Perot cavity shown in Fig. 3.1.3(a) where the nanowire section of length s is sandwiched between two 1D PhC mirrors. We call such cavity guided-mode cavity. We select the same parameters used in Fig. 3.1.2(b) ($d = 120nm$, $a = 160nm$, 30 pairs of PMMA/air grating at each side), in order to assure single-mode behavior of the nanowire, as well as to position the emission wavelength of CdS (500nm) at the midgap of the PhC mirror. This provides the smallest penetration depth into the PhC mirror leading to a small mode volume, as well as minimizes the mirror transmission loss thus maximizing the overall Q. By tuning the cavity length (s), cavity modes with different symmetries can be formed and positioned precisely at the mid-gap frequency. The Q

factors of these modes are 300, 395 and 500, for $s/a = 1.27, 1.95, 2.85$, respectively. We note that using this simple guided-mode approach it is possible to realize cavities with higher Q at the expense of an enlarged mode volume, by tuning the cavity resonance closer to the air-band edge. However, these modes are not of interest in this work due to the reduced Q/V ratio.

The total Q factor of the 1D PhC cavity can be separated into transmission loss due to the finite length of the mirror, and the above-mentioned scattering:

$$\frac{1}{Q} = \frac{1}{Q_{sc}} + \frac{1}{Q_w} \tag{3.1}$$

In our case, 30 layers of PhC mirror result in quality factor from waveguide loss of $Q_w \sim 10^5$, which is significantly larger than the Q of guided-mode cavities obtained above. This implies that the dominant loss mechanism is scattering at mirror interfaces, as noted previously in Ref. [56]. In that work it was suggested that the mode profile mismatch between guided mode at the cavity region and Bloch mode is the main reason for large scattering losses. This mismatch can also be viewed as the effective impedance mismatch between cavity mode and the Bloch mode propagating in the mirror. From Fig. 3.1.3(c) we can see that the cavity guided mode has a mode index of $n_{cavity} = 1.72$, while the evanescent Bloch mode positioned at the midgap frequency has a mode index of $n_{mid-gap} = 1.55$.

To eliminate this index difference and the resulting mode mismatch, we substitute the uniform cavity region with a PMMA/air grating with the same duty cycle but a smaller period [Fig. 3.1.3(b)]. By choosing the period of this cavity section to be $w = 0.78a$, we tune the cavity resonance to the mid-gap frequency of the mirror. Fig. 3.1.3(c) shows the photonic bands of the cavity segment as well as the PhC mirror. The propagating dielectric-band Bloch mode supported in the cavity region couples to the evanescent Bloch mode that exists within the bandgap of the PhC mirror to form the cavity mode. In contrast with the former design, the cavity mode here is a Bloch mode (instead of guided mode), and therefore the cavity is referred to as Bloch-mode cavity. The Q factor of our Bloch-mode cavity

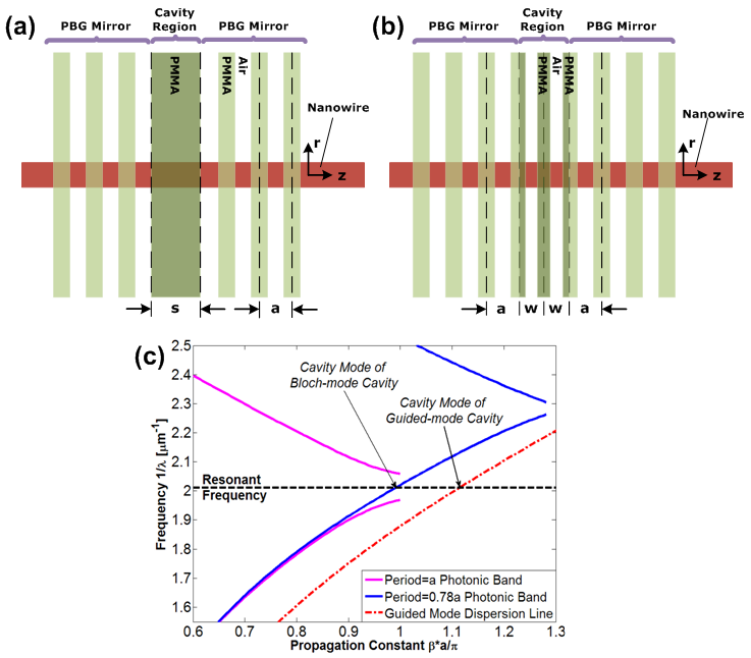

Figure 3.1.3: (a) Schematic of guided-mode cavity. (b) Schematic of Bloch-mode cavity. (c) Dispersion line of Bloch mode with periodicity of $0.78a$ (blue solid), Bloch mode with periodicity of a (pink solid), and guided mode of nanowire embedded in PMMA (red dash-dot).

is $2,430$ and the mode volume is $0.129(\lambda/n)^3$. As expected, the increase in Q is due to the reduced mode profile mismatch between the Bloch mode of the cavity and evanescent Bloch mode of the mirror. Recently another group have proposed similar cavity design in order to realize high-Q cavities [65].

Further Q enhancement can be realized by tapering the mode profile from the dielectric band to mid-bandgap by adding taper segments, as shown in Fig. 3.1.4(a). Two degrees of freedom are available to achieve the transition between the cavity Bloch mode and the evanescent Bloch mode of the mirror, namely the period (w) and the duty cycle of each segment. Here we keep the duty cycle fixed at 0.5, as we did in the cavity segment. Linear interpolation of grating constant ($2\pi/w$) of each segment is used to carry out the tapering process. Mid-bandgap resonance is achieved by altering the length of the central segment w_1. Similar tapering tech-

niques were previously used to realize high-Q heterostructure cavities based on 2D PhC waveguides [66–68].

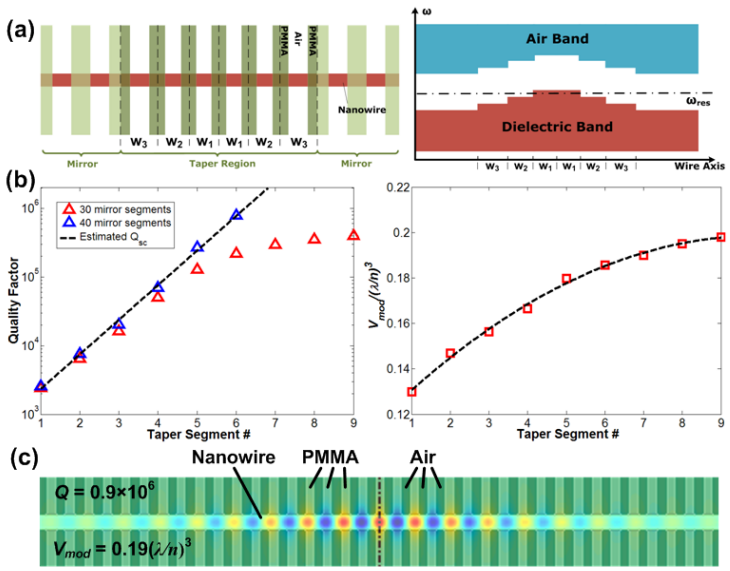

Figure 3.1.4: (a) Schematic of photonic band tapering. (b) Quality factor and mode volume as a function of number of taper segments. In all cases, the cavity was designed to support one resonance position at the mid-gap wavelength of 497nm. (c) Mode profile of cavity modes (E_φ component) with 6 taper segments and 40 mirror pairs. Configuration of the tapered gratings is also mapped as background.

In Fig. 3.1.4(b) we present the dependence of the Quality factor on the number of segments placed in the taper region (one-segment structure corresponds to Bloch-mode cavity). For the case of 30 mirror pairs at each end (not including taper segments), Q first increases logarithmically as the number of taper segments increases, and then levels off when the number of tapers is larger than 5. When we increase the number of PhC mirror pairs to 40, the logarithmic dependence of Q on number of segments is recovered. Therefore, we conclude that for large number of taper segments, transmission losses become dominant, and more mirror pairs are required. In Fig. 3.1.4(b), we also present the mode volume of the

cavity calculated using Eq. 3.2.

$$V = \frac{\int_V \varepsilon(\vec{r}) \left|E(\vec{r})\right|^3 dV}{\max\left[\varepsilon(\vec{r}) \left|E(\vec{r})\right|^3\right]} \tag{3.2}$$

As expected, the mode volume increases as the number of taper segments increases. However, the increase of V is modest, especially for large number of taper segments. Moreover, in all cases the mode volume is smaller than $0.2(\lambda/n)^3$. This is due to the fact that we deliberately positioned the cavity mode precisely at the midgap frequency, and therefore the cavity field decays rapidly inside the PhC mirror. In the case shown in Fig. 3.1.4(c), Q/V can be as high as 4.7×10^6 per cubic wavelength in material.

In previous paragraphs, we explained the ultra-high Q of our nanowire-based cavities using the mode-matching arguments. The high Q factor can also be explained by looking at the distribution of the cavity field energy in momentum space (k-space, spatial Fourier transform space) [47, 69–71]. In Fig. 3.1.5, we show the Fourier transform of the electric components E_φ of the cavity mode. $k_z = n_{clad}\omega/c_0$ defines the light line of the cladding. Components with k_z smaller than the light line support plane waves leaking energy radially into the cladding, and are responsible for scattering losses. The light cones in PMMA and air are colored in light green and dark green, respectively. We can see that as we include more taper segments, the Fourier spectrum of the mode profile concentrates more tightly around the edge of the Brillouin zone $k_z = \pi/a$, reducing the energy of the mode within the light cones, thus reducing the scattering. For comparison, the spatial spectrum of the guided-mode cavity, shown in black, extends significantly inside the air and polymer light line, indicating large scattering losses.

Our system is very similar to micropost (micropillar) optical microcavities that have been extensively used in vertical-cavity surface-emitting lasers [72] and single photon sources [45, 73–76], and more recently proposed in the context of semiconductor nanowires [77]. However, the big advantage of our approach that combines bottom-up synthesized nanowires with top-down fabricated photonic-crys-

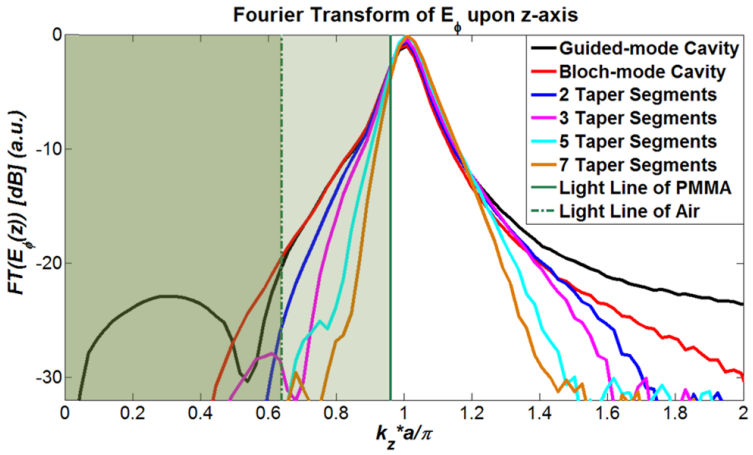

Figure 3.1.5: Fourier transform of E_φ along wire axis. k-space zones within the light line are shown in green (light green within PMMA light line, dark green within air light line).

tals (only electron-beam lithography step), is simple fabrication procedure [42]. Complicated epitaxial growth of Bragg mirror, typical for conventional micropost cavities, is not required. Our technique is therefore fully compatible with different nanowire growth approaches including solution-based synthesis, vapor-solid-liquid, etc.

Next, in Fig. 3.1.6 we show how the overall quality factor depends on the material losses of the cladding (red-square), in the case of the optimized cavity ($Q = 0.9 \times 10^6$). Refractive index of the cladding is assumed to be of the form $n_{clad} + i\kappa_{clad}$, resulting in loss $(1/Q)$ of the form $\eta \times 2\kappa_{clad}/n_{clad}$, where the coefficient η takes into account the overlap between the mode and lossy cladding ($\eta < 1$). Thus the overall Q factor can be derived using Eq. 3.3.

$$\frac{1}{Q} = \frac{1}{Q_{lossless}} + \eta \frac{2\kappa_{clad}}{n_{clad}} \tag{3.3}$$

Using FDTD we found that $\eta = 0.3$ (Fig. 3.1.6). In the case of PMMA cladding, κ_{clad} is smaller than 4×10^{-6} for wavelength of 500nm, that is the absorption coefficient of PMMA is smaller than $a = 0.1mm^{-1}$ [78]. As shown in Fig. 3.1.6,

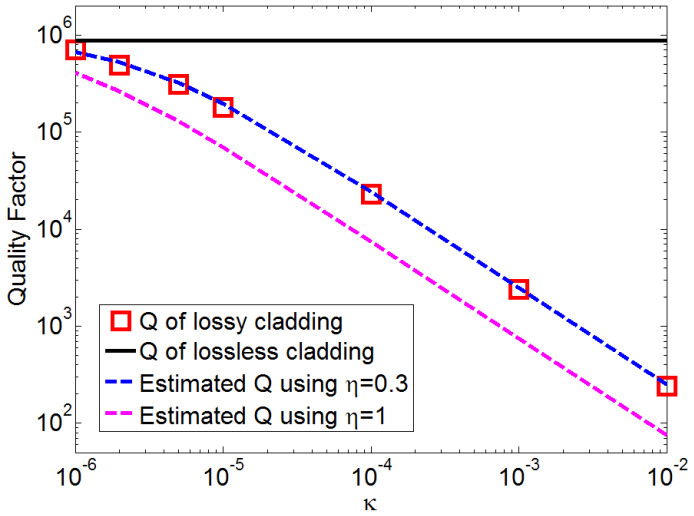

Figure 3.1.6: Quality factor (red-square) as a function of imaginary part of refractive index (κ). The Q value with lossless cladding is indicated in black line. The dash lines represent estimation of Q using Eq. 3.3, while $\eta = 0.3$ (blue) and 1 (magenta), respectively.

this loss results in small reduction of overall quality factor from $Q = 9 \times 10^5$ to $Q = 3 \times 10^5$. It is important to note that absorption coefficient of PMMA is even smaller (almost an order of magnitude) at red, near-infrared and telecom wavelengths (with the exception of two bands around 1100nm and 1400nm [78]) and therefore even higher quality factors can be obtained with nanowires emitting at these longer wavelengths.

Depending on the crystal structure of the nanowire material and the preferred growth direction, the nanowire cross-section can be triangular, square, hexagonal and so on. Here we consider nanowires with hexagonal cross-section embedded in our 1D PhC cavity [Fig. 3.1.7(a)]. First, the waveguide mode [Fig. 3.1.7(b)] and effective mode index of a nanowire with hexagonal cross-section is found. Next, the diameter of the equivalent cylindrical nanowire is chosen, so that it supports the mode with the same effective mode index. Then, a high-Q cavity is designed for the cylindrical nanowire by taking advantage of radial symmetry and using the optimization procedure described above. The same cavity design is then ap-

plied to the nanowire with hexagonal cross-section. In this way the optimization is done using 2D-FDTD with radial symmetry, which is significantly faster than performing a 3D-FDTD computation, which would be necessary for nanowires with hexagonal cross-section. Using this approach, we designed cavity for a nanowire with $d_{hex} = 130nm$, using 40 mirror pairs and 5 taper segments. The resonance at $\lambda = 497nm$ had a $Q = 9.4 \times 10^4$ and $V = 0.18(\lambda/n)^3$ [Fig. 3.1.7(c)]. Further optimization of the structure using 3D FDTD could result in even higher Q values.

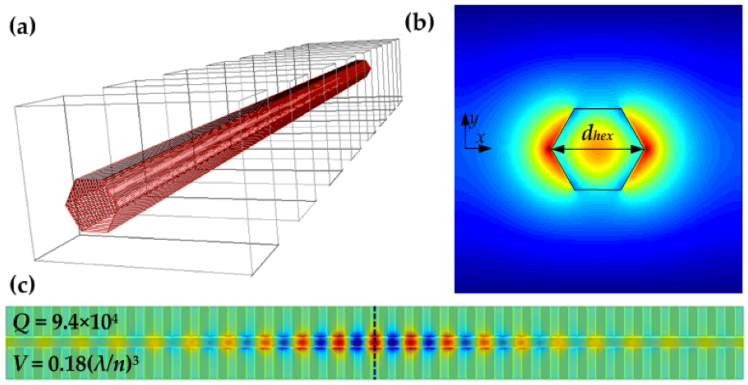

Figure 3.1.7: (a) Schematic of hexagonal cross-section nanowire embedded in air/PMMA grating. (b) Mode profile of E_x component of hexagonal cross-section nanowire embedded in PMMA cladding. (c) Mode profile of cavity modes (E_x component) with 5 taper segments and 40 mirror pairs.

3.1.4 Light-matter interaction in semiconductor nanowire cavities

As first noted by Purcell [79], the emission rate of a radiating dipole can be modified by placing the dipole inside an optical cavity. The enhancement of the radiative emission rate into the cavity mode, when compared to the spontaneous emission rate without the cavity, can be described by the Purcell factor where V is mode volume of the cavity and ε_M is the dielectric constant at the field intensity maximum point. If $F_o \gg 1$, the dipole will emit much faster into the cavity than into free space. This increase in the radiative recombination rate is beneficial for the reduction of nanowire lasers threshold, and could result in the realization of

threshold-less lasers [80]. In the case of a single-photon source based on a QD embedded within the semiconductor nanowire, the large Purcell factor means a high photon-production rate and a smaller probability for nonradiative recombination. Moreover, photons are preferentially emitted into the well-defined cavity modes and thus can easily be coupled out, using for example proximal optical waveguides, thereby increasing the overall collection efficiency of generated photons. In our system we find that Purcell factor ($F = F_o/n_{wire}$) can be as high as 1.3×10^5 when 6-segment taper is used with material losses considered. It drops to 2.7×10^4 and 3.0×10^3 when four and two taper segments are used, respectively. Large Purcell factor is due to the ultra-high Q and very small V in our cavity. The cavity may even enter the strong-coupling regime of light-matter interaction [57, 81], in which coherent exchange of energy between photon trapped in the cavity and exciton trapped in the QD exists. This happens when cavity field decay rate $\kappa = \omega/2Q$ and exciton decay rate γ (exciton loss due to the emission into non-cavity modes and non-radiative recombination channels) are smaller than exciton-photon coupling parameter g [76, 81]. For the cavity defined precisely around the quantum dot positioned in the center of the nanowire (at the electric field maximum), and transition dipole moment aligned with the electric field dipole, the coupling parameter can be expressed as $g = \Gamma\sqrt{V_o/4V}$, where g is the Rabi frequency of the system on resonance and $V_o = (3c_o\lambda^2\varepsilon_o)/(2\pi\Gamma\varepsilon_M)$. Here $\Gamma = n_{wire}\omega^3\mu^2/3\pi\varepsilon_o\hbar c^3$ is the spontaneous emission rate in the material. Assuming radiative life time of exciton without cavity to be 1ons, that is its radiative rate of $\Gamma = 0.1GHz$ we get coupling parameter $g = 190GHz$. Typical values for non-radiative decay rates of excitons are bellow this value [81], and therefore the limiting factor for strong-coupling regime is cavity field decay rate. Therefore, we conclude that in our system, $g > \kappa, \gamma$ when $Q > 10^4$ ($\kappa < 189GHz$), and the system is well into the strong coupling regime even when only three taper segments are used.

Finally, we note that the most promising material systems used for realization of heterostructure QDs within nanowires are based on semiconductors with refractive index larger than $n_{wire} \approx 2.8$ [53–55]. For example, in Ref. [54], the nanowire is based on GaP platform with $n_{wire} = 3.4$. Our hybrid nanowire-1D PhC platform

is general, and we confirmed that it can be used to realize cavities with high Q and small V with these nanowires with larger refractive index.

3.1.5 Conclusion

Design of an ultra-high Q optical nanocavity consisting of a semiconductor nanowire embedded in 1D photonic crystal has been demonstrated. The mechanism of effectively suppressing cavity losses has been theoretically analyzed, and a cavity with $Q = 3 \times 10^5$ and mode volume smaller than $0.2(\lambda/n)^3$ has been designed. Ultra-high Purcell factor, and operation in the strong-coupling regime are predicted in the proposed platform. High Q/V cavities based on nanowires with hexagonal cross-section have also been designed. Our system is similar to micropost (micropillar) optical resonators that have been used in vertical-cavity surface-emitting lasers and single photon sources. However, our approach requires simple fabrication procedure that combines bottom-up nanowire synthesis with top-down single-step e-beam lithography.

3.2 Ultrahigh-Q/V micropillar cavities

3.2.1 Introduction

Micropillar optical cavities, typically used in low-threshold vertical-cavity surface-emitting lasers (VCSELs) [82–84], have recently attracted considerable attention as a promising platform for solid-state implementations of cavity quantum electrodynamics (cQED) experiments [85, 86]. These applications benefit from large quality factor (Q) that can be obtained in micropillar cavities, which in turn results in a long photon life time $\kappa = \omega/2Q$ (ω is the radial frequency of the cavity mode). For example, high-Q micropillar cavities ($Q \sim 165,000$) have been demonstrated recently for large diameter ($d = 4$"μm) pillars, resulting in a relatively large mode volume [$V > 50(\lambda/n)^3$] [87]. However, for applications in cQED, coupling between an emitter and a photon localized in the cavity requires a large Rabi frequency g that is proportional to $1/\sqrt{(V)}$. In order to decrease the

mode volume, it is necessary to decrease the pillar diameter and thereby improve the radial confinement of light. However, this can lead to a significant reduction in the Q factor in the traditional micropillar designs [88], and the best Q factors reported in the case of sub-micron diameter micropillars have been theoretically limited to approximately 2,000 [89].

In this section, we theoretically demonstrate sub-micron diameter micropillar cavities with an ultra-high Q/V that is three orders of magnitude larger than previously reported. This is achieved by simultaneously increasing the Q ($Q \sim 3 \times 10^6$) and reducing the mode volume [$V \sim 0.1(\lambda/n)^3$], using a bandgap tapering method developed recently in 1D photonic crystal structures [90, 91]. While the proposed approach is general and can be applied to a range of material systems and applications, our cavities are designed to operate at 637nm wavelength and therefore are suitable for coupling to nitrogen-vacancy (NV) color centers embedded within diamond nanocrystals positioned at the middle of the cavity. NV color centers have recently attracted significant attention as promising quantum emitters [92]. NVs emission is broad band (630nm-750nm) with stable zero-phonon line at 637nm visible even at room temperature.

3.2.2 Design

Our micropillar is based on two distributed Bragg mirrors (DBR) that consists of TiO_2 ($n_{TiO_2} = 2.4$) and SiO_2 ($n_{SiO_2} = 1.5$) alternating layers, and a TiO_2 spacer of thickness s sandwiched between them [Fig. 3.2.1(a)]. The micropillar cavity Q is inversely proportional to the cavity losses that in turn can be separated into two components: the transmission losses due to the finite length of the DBRs, and the scattering losses at the spacer/mirror interfaces. The former can be minimized (for a given number of TiO_2/SiO_2 pairs) using a "quarter stack" DBR that consists of TiO_2/SiO_2 layers with thickness $\lambda/4n_{eff}$, where $\lambda = 637$nm. This also maximizes light confinement along the pillar axis, resulting in a minimized mode volume. For example, in the case of a micropillar with diameter $d = 340$nm, the thicknesses of TiO_2 and SiO_2 layers in DBR are 82.6nm and 147.4nm, respectively, resulting in

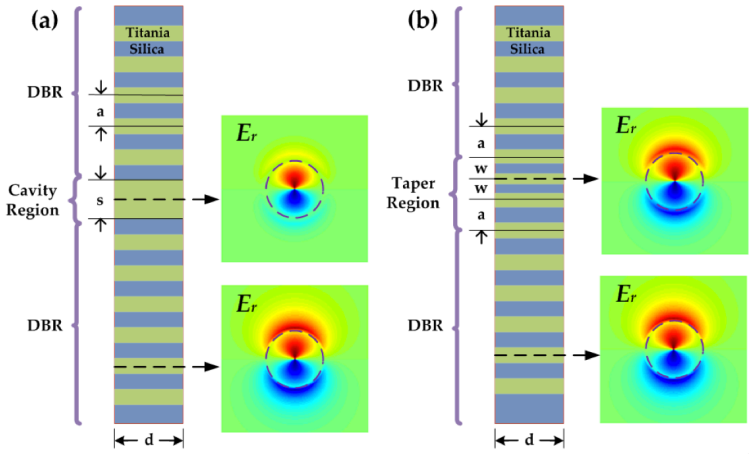

Figure 3.2.1: (a) Traditional design of micropillar cavities and (b) modified design where the center segment is substituted by titania/silica pairs. The lateral mode profile of E_r component for cavity mode and evanescent Bloch mode that exists inside DBRs are shown on the right of the cavity layout. Improved mode-matching can be seen in (b).

total DBR periodicity of $a = 230$nm. Next, the thickness of the spacer is chosen ($s = 220$nm) in order to position the cavity resonance at 637nm, and the quality factor (Q) of such cavity is obtained using finite-difference time-domain method (FDTD). We find $Q \sim 100$ which is consistent with previous reports [88]. The low Q is attributed to scattering losses arising from the mode profile mismatch between the localized cavity mode and evanescent Bloch mode inside the DBRs [56]. Fig. 3.2.1(a) illustrates the profile mismatch for E_r component. To suppress this mode mismatch and the resulting scattering losses, we use the mode matching technique previously developed for 1D photonic crystal cavities [90]. We substitute the uniform center segment with a single TiO_2/SiO_2 pair with the same aspect ratio as in the DBR but a smaller thickness w. When $w = 0.67a$, the cavity resonates at $\lambda = 637nm$ with $Q = 6,000$, a 60-fold improvement over the conventional design.

In order to increase the Q factor further, we incorporate more TiO_2/SiO_2 segments with varying the thicknesses w_i (i is the segment number). This can also

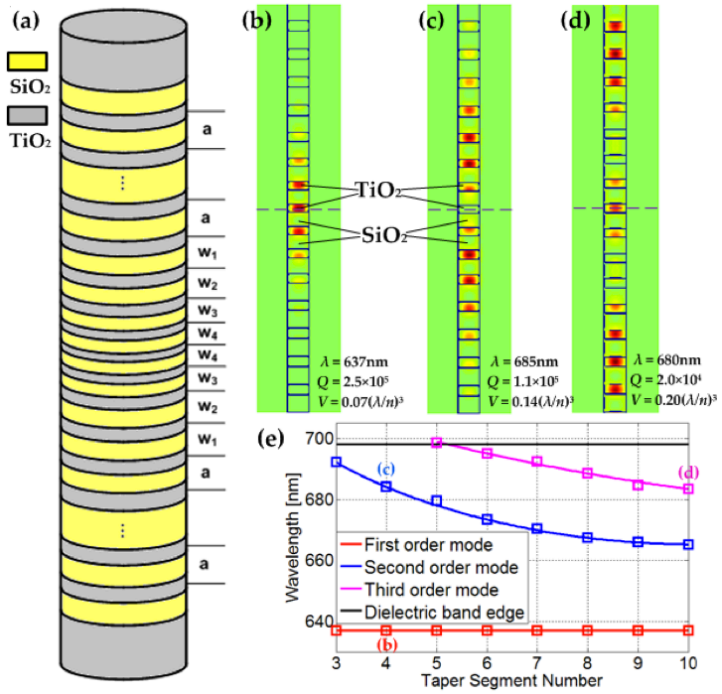

Figure 3.2.2: (a) Schematic of a 4-taper-segment micropillar cavity. (b)(c) Electric field density profile of the first and second order mode, respectively. (d) Electric field density profile of the third order mode of the 10-taper-segment micropillar cavity. (e) Mode diagram as a function of taper segment number.

be seen as a "tapered DBR" approach, where each taper section further reduces the mode mismatch in order to suppress the scattering losses. In Fig. 3.2.2(a), we use 4 tapered segments and 20 DBR pairs at each side. In order to set the resonating wavelength at 637nm, the thickness of each taper segment is precisely tuned to $w_1 = 215.3nm$, $w_2 = 202.4nm$, $w_3 = 191.0nm$, and $w_4 = 180.8nm$. The resulting mode has a Q factor of 250, 000 and a mode volume of $0.07(\lambda/n)^3$, which represents at least three orders of magnitude enhancement of Q/V compared to any previous micropillar designs. As shown in Fig. 3.2.2(b), this high-Q mode has an anti-node at the central TiO_2 segment and therefore is ideally suited for coupling to quantum emitters, such as an NV center in diamond or a semiconductor nanocrystal, embedded within this layer. We also find a second-order cavity

mode [Fig. 3.2.2(c)] at wavelength of 685nm with a respectable $Q = 110,000$. The Q factor of the fundamental mode can be enhanced by increasing the tapering process. For instance, we obtain $Q = 3,000,000$ and $V = 0.10(\lambda/n)^3$ with 10 taper segments. However, increasing the cavity length pulls higher-order modes from the dielectric band into the bandgap, as shown in Fig. 3.2.2(d) and (e). These higher order modes can potentially couple to the emitter placed at the center of the cavity and the resulting multi-mode cavity is not desirable. Therefore from here on, we only consider 4-taper-segment cavities, which limits our Q to 250,000.

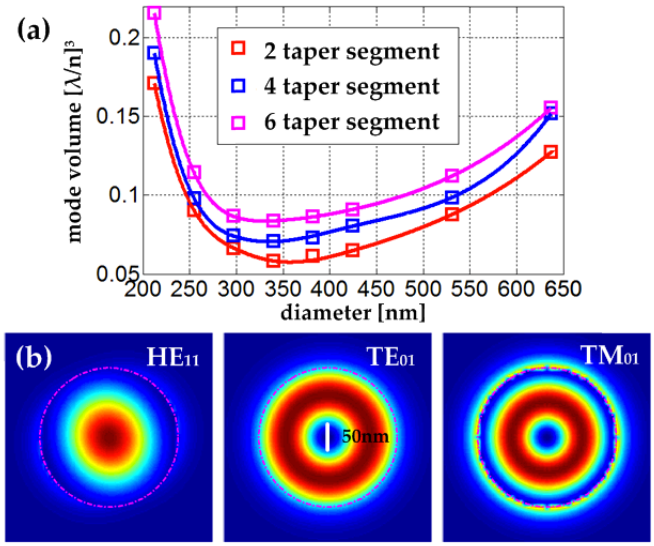

Figure 3.2.3: (a) Mode volume as a function of micropillar diameter. Here all the modes are first-order HE_{11} modes resonating at 637nm. (b) Lateral electric field density profiles of HE_{11} ($\lambda = 637nm$), TE_{01} ($\lambda = 578nm$) and TM_{01} ($\lambda = 492nm$) cavity modes.

Next, we optimize the diameter of our micropillar cavity to minimize its mode volume. It can be seen in Fig. 3.2.3(a) that the smallest mode volume is obtained at $d = 340nm$. For $d < 340nm$, V increases due to the reduced confinement in the axial direction: the effective impedance contrast between TiO_2 and SiO_2 is reduced for small diameters, and therefore the width of the bandgap decreases, resulting in deeper penetration of the cavity mode into the DBRs, thus increasing

V. For $d > 340nm$, however, the mode is almost completely confined within the pillar and the n_{eff} of each segment approach the refractive index of the material. Therefore, the width of the bandgap remains approximately constant as the pillar diameter increases and the axial confinement remains the same. However, V increases due to the larger mode cross-section (radial confinement increases). The trade-off between radial and axial confinement results in an optimized diameter of $d = 340nm$. For the 4-taper-segment cavity, we also find the cavity modes with TE_{01} and TM_{01} profiles at wavelengths of 578nm and 492nm, respectively. Both of these modes peak at the central TiO_2 segment. However, the lateral electric field density profiles shown in Fig. 3.2.3(b) indicate that these modes have a node at the center of the micropillar and therefore will not couple efficiently to the nano-emitter placed at the center. Moreover, these modes are detuned from the emission spectrum of an NV center and therefore are not of interest. It is also important to note that if the pillar diameter increases further, additional higher-order modes, with the same azimuthal order as HE_{11} (e.g. EH_{11}), are allowed. These modes can couple to the fundamental HE_{11} cavity mode and thus introduce additional loss mechanism [88], and reduce the Q factor of the fundamental cavity mode.

3.2.3 Conclusion

In conclusion, we have demonstrated that high Quality factor micropillar cavities can be realized with sub-micron diameter pillars. We have engineered the cavities with a record low mode volume of $V = 0.07(\lambda/n)^3$ and a Quality factor of $250,000$. We expect, however, that realistic fabricated structures will have reduced quality factors due to fabrication-related imperfections, including surface roughness, slanted walls and material absorption. One possible approach to overcome these problems is based on oxide-aperture design [93]. We predicted that by embedding a diamond nanocrystal with an NV color center at the middle of the cavity, the strong coupling limit of light-matter interaction can be achieved. Our method can be easily adapted to different material systems and enable realization of an ultra-high Q/V cavity in AlAs/GaAs platform suitable for realization of low-

threshold VCSELs, for example.

4

Photonic crystal lasers

4.1 Introduction

Photonic crystal (PhC) [94, 95], material with a periodic variation of refractive index, is a versatile platform for manipulating the propagation, reflection and refraction of light. Specifically, light can be localized within the photonic bandgap (PBG), where the propagation of light is prohibited via Bragg Scattering. This is of great interest for realization of functional optical devices including nanocavities and waveguides. Empowered by numerical simulation methods, such as the finite-difference time-domain (FDTD) and the finite element method (FEM), and state-of-the-art nano-fabrication techniques (e-beam lithography, reactive-ion etching, scanning electron microscopy, etc.), photonic crystal cavities can be designed and fabricated with ultra-high Quality factors (Q) of over a million and small mode volumes (V) close to the diffraction limit [$\sim (\lambda/2n)^3$]. Current tech-

nologies enable production of one-dimensional (1D) [62, 96, 97] and two-dimensional (2D) [67, 71, 98–103] PhC cavities with high integration capacity on a semiconductor chip. High-quality three-dimensional (3D) photonic crystal cavities have also been demonstrated [104], yet scalable productions of 3D-PhC devices still remains challenging.

Photonic crystal lasers (PhCLs) are lasers that utilize photonic crystal cavities to achieve the optical feedback. The history of developing lasers confined with photonic bandgap can be traced back to the vertical-cavity surface-emitting lasers (VCSELs) [105], where distributed Bragg reflectors (DBRs) are used to confine light in the vertical direction: in fact, the concept of Bragg reflector can be seen as an one-dimensional photonic crystal. On the other hand, typical VCSELs have their device diameters orders of magnitude larger than the operating wavelengths, resulting in weak photon confinement in the lateral directions and correspondingly a large mode volume.

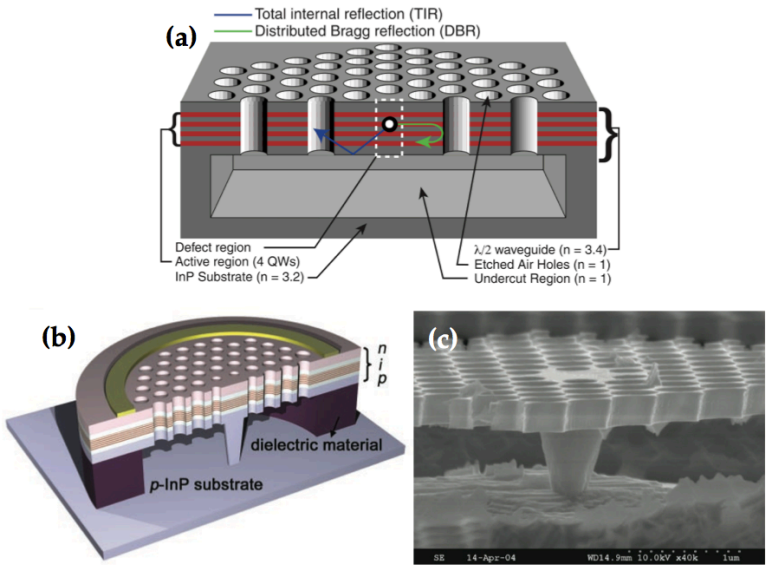

Figure 4.1.1: (a) Schematic diagram of the first reported PhC laser [106]. It is based on a 2D-PhC suspended membrane that contains four as-grown semiconductor QWs. (b)(c) Schematic diagram and scanning electron micrograph of the first electrically-injected PhC laser [107].

The first claimed photonic crystal laser was demonstrated in Axel Scherer's group at Caltech in year 1999 [106] using a 2D-PhC slab cavity. In this work, a suspended InGaAsP membrane perforated with a 2D triangular lattice of holes was used to localize a cavity mode within mode volume $V \sim 0.31(\lambda/n)^3$ using DBR in the lateral directions, and total internal reflection (TIR) in the vertical direction, as shown in Fig. 4.1.1(a). The suspended slab contained four as-grown quantum wells that provided the optical gain at telecommunication wavelength ($\sim$ 1500nm). The laser was pumped optically, using a pump laser operating at lower wavelength (830nm). Furthermore, the pumped laser was pulsed with 4% duty cycle and the substrate was cooled to 143K to avoid excessive heating of the device. Owing to their planar nature, large arrays of PhCLs can be easily fabricated and lithographically tuned to operate at different wavelengths. This is a clear advantage over VCSELs, for example, which require epitaxial growth of a large number of Bragg-mirror layers using metal-organic chemical vapor deposition (MOCVD) or molecular beam epitaxy (MBE).

Following this first demonstration, the PhCL operating at room temperature with continuous wave (CW) optical excitation was demonstrated by the Lee group at KAIST in year 2000 [108]. In this work, a 2D photonic crystal slab containing semiconductor QWs was fabricated on a low-index Al_2O_3 substrate to facilitate heat dissipation. The same group at KAIST later demonstrated the first electrically-driven PhCL in year 2004 [107]. The main difficulty associated with realization of electrically-driven PhCL was placement of electrodes close to the cavity to enable efficient carrier injection without inducing large optical losses due to metal absorption which can significantly reduce the cavity Q and be detrimental for the laser performance. In their work, the KAIST group solved the problem by leaving a small post at the center of the cavity supporting the 2D PhC slab, as shown in Fig. 4.1.1(b) and (c). The post acts as an electronic wire that delivers carriers directly in the center of the cavity without degrading the Q significantly.

Owing to their planar nature, PhCLs can easily be integrated with passive optical components. There are two main approaches demonstrated so far. The first

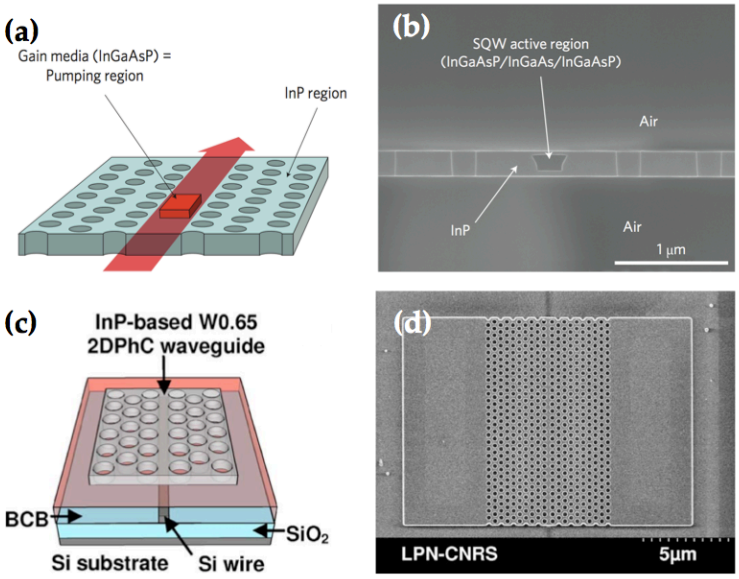

Figure 4.1.2: (a)(b) Schematic diagram and scanning electron (SEM) micrograph of the buried heterostructure PhCL. The active region is embedded in an InP layer [109]. (c)(d) Schematic diagram and SEM of the PhCL bonded on silicon-on-insulator wafer [110].

is based on the so-called buried heterostructure [109]: the as-grown InGaAsP quantum wells are first patterned into a quantum box and a passive InP layer is then re-grown on top of them, and the sample is planarized. The 2D-PhC cavity is then defined using e-beam lithography so that it spatially overlaps with the quantum wells. An optical waveguide is also realized in the same lithography step to enable efficient in-coupling of pump light and out-coupling of generated laser signal, as shown Fig. 4.1.2(a) and (b). This compact structure not only greatly improves the pumping and collection efficiency through direct waveguide coupling, but also avoids the excessive heating. The second example makes use of planarising BCB polymer to bond III-V active materials onto a silicon-on-insulator (SOI) wafer [110]. The process starts by defining an optical waveguide in the device layer of SOI, followed by planarization of the SOI wafer and bonding with III-V material. After the bonding, the PhCLs is fabricated in the active material, on top of the Si waveguide. In this way, PhC cavity is evanescently coupled to the silicon waveg-

uide, as shown in Fig. 4.1.2(c) and (d), which facilitates in-and out-coupling of light. This approach has reduced coupling efficiency than the first, direct waveguide coupling, method, but in turn enables PhCL integration with silicon photonics.

The advantages of photonic crystal lasers go well beyond their small footprints and integration capacity. The most prominent advantage of PhCLs is that they require low threshold powers, mostly attributed to their small mode volumes and high Quality factors. Optical pumping thresholds have been reported to be on the order of one microwatt for semiconductor quantum well lasers [109, 111] and as low as tens of nanowatts for semiconductor quantum dot (QD) lasers [112, 113]. In the case of electrical pumping, threshold currents as low as 181nA have been reported, which is orders of magnitude smaller than other laser devices [114]. In fact, theory predicts that threshold-less lasing is achievable in an ideal single-mode PhC cavity fabricated in perfect 3D photonic crystal with omni-directional bandgap. In this case, radiative emission coupled to all non-lasing optical modes is prohibited [115, 116]. A detailed theoretical analysis of lasing thresholds of PhCLs is presented in the next section.

In addition to low thresholds, PhC lasers can also be driven with a high modulation speed: the high Q/V ratio of PhC cavities result in cavity Purcell effect, which extensively reduces the radiative lifetime of carriers [117]. A modulation speed that exceeds 100GHz has been demonstrated based on a 2D PhC laser [118]. This feature is especially important for information processing applications. Moreover, the design flexibility of PhC cavities allows tailoring the lasers' polarizations [119] and far-field patterns [120]. Finally, the wavelength of PhCLs can be controllably tuned, by employing opto-mechanic effects [121] or liquid crystals [122].

4.2 Lasing threshold of photonic crystal lasers

It has been first predicted by Yamamoto et al. that a high spontaneous emission factor (β), defined as the fraction of spontaneous emission that couples to the lasing mode, is responsible for decreasing the lasing threshold [115]. In the ideal sce-

nario where the emitter does not suffer from non-radiative decay, a system with a $\beta = 1$ can achieve a fascinating effect: threshold-less lasing. This limit of β equals unity can be achieved using two vary different approaches, (i) by increasing the rate of spontaneous emission into the lasing mode, or (ii) by suppressing the spontaneous emission into all other non-lasing modes. Both approaches will be discussed in this work.

In conventional semiconductor lasers based on Fabry-Perot cavities for example, $\beta < 0.001$ due to a large number of cavity modes that are supported by the large cavity [123, 124]. Larger β factors can be achieved in microdisk lasers due to larger free-spectral range (FSR) of this geometry. For instance, for a small 2μ m-diameter microdisk lasing at 1.55μ m wavelength, β factor as high as ~ 0.1 was measured [125]. In contrast, as we will see, PhC cavity can be designed to have very few (or only one) cavity modes localized within the photonic bandgap. This extensively decreases the number of non-lasing modes coupled to the gain medium and increases β factor. Furthermore, PhC bandgap can decrease the optical density of states within the gain spectrum, therefore reducing the coupling to other radiative modes.

4.2.1 Purcell effect and β factor

First consider a basic model: a quantum emitter coupled with a single optical mode through cavity-induced interaction. Predicted by Purcell [117], the radiative lifetime of a quantum emitter located within a cavity can be altered. The dipole-cavity coupled system can be described using the Jaynes-Cummings Hamiltonian [126],

$$\hat{H} = \hbar\omega\hat{\sigma}_z + \hbar\omega(\hat{a}^+\hat{a} + \frac{1}{2}) + i\hbar g(\hat{\sigma}_-\hat{a}^+ + \hat{\sigma}_+\hat{a}) \tag{4.1}$$

where the first and second term represent the dipole and photon energy respectively, and the third term represents the coupled energy between the dipole and the photon. g is the Rabi frequency. Two decay channels can induce decoherence to the system: emitter's non-radiative decay (γ) and photon's cavity loss (κ). The

eigen-frequencies of the system can be derived as

$$\omega_{\pm} = \frac{\omega_c + \omega_e}{2} \pm \sqrt{g^2 + (\frac{\delta\omega}{2} - i\frac{\kappa - \gamma}{4})^2} - \frac{i}{4}(\kappa + \gamma) \tag{4.2}$$

To simplify the analysis, one can make the assumption that there is no frequency detuning between the emitter and the cavity ($\delta\omega = 0$), and the loss rate induced by the cavity overtakes the loss of the emitter ($\gamma \ll \kappa$). Then in the strong damping limit ($g \ll \kappa$), the emitter loss rate can be evaluated as

$$\Gamma_{sp} = 2\mathrm{Im}\{\omega_+\} = \frac{4g^2}{\kappa} \tag{4.3}$$

where g^2 is inversely proportional to V, and κ is inversely proportional to Q.

Two more assumptions are made: (i) the emitter is located at the optical mode's field maximum, and (ii) the dipole's oscillating direction is co-directional with the electric field. The Purcell factor can now be deduced by comparing Eq. 4.3 to the spontaneous emission rate of an emitter in a homogeneous medium with refractive index n_{ref}.

$$F = \frac{\Gamma_{sp}}{\Gamma_{sp,free}} = \frac{3}{4\pi^2}\frac{Q}{V/(\lambda/n_{ref})^3} \tag{4.4}$$

Note that all the foregoing derivations are under the assumption that ($\gamma \ll \kappa$). However, for most solid-state emitters (bulk semiconductor, semiconductor QWs, etc.), non-radiative intraband transition is considerable at room temperature. For instance, the InGaAsP QWs have a homogeneous broadening of $\sim$ 8.8nm at room temperature [111]. Therefore, for high-Q cavity with Q factor larger than 1000, the cavity mode linewidth is much narrower than the electric transition spectrum. The Purcell factor should thus be modified to the more general expression:

$$F = \frac{\Gamma_{sp}}{\Gamma_{sp,free}} = \frac{3}{4\pi^2}\frac{\lambda}{\Delta\lambda_M}\frac{1}{V/(\lambda/n_{ref})^3} \tag{4.5}$$

where $\Delta\lambda_M = \max\{\Delta\lambda_e, \Delta\lambda_c\}$.

Eq. 4.5 applies to all models where the emitter is coupled to a single cavity mode.

In reality, more than one optical mode can interact with the emitter. For instance, considering an ideal 3D photon gas model, where the photon is confined by metallic boundaries in all the three dimensions, the frequency spacing between two neighboring modes is calculated as,

$$\Delta\omega_{FSR} = \frac{2\pi^2 c^3}{n_{ref}^3 V \omega^2} \tag{4.6}$$

Suppose the emitter spectrally overlaps with one of the cavity modes (mode 0 with double degeneracy) at ω, then Eq. 4.5 is only valid under the single mode condition when $\Delta\omega_{FSR} \gg \Delta\omega$. If V is large enough, the mode spacing allows the emitter to couple to multiple modes, and the alteration ratio of the total spontaneous emission rate (F) should include the sum of all these interactions, i.e. $F^{'} = \frac{\Gamma_{sp}}{\Gamma_{sp,free}} = \sum_{i=0}^{N-1} F_i$. As V approaches infinity, the number of modes within the broadening $\Delta\omega M$ can be calculated as $N = \frac{\Delta\omega_M}{\Delta\omega_{FSR}} = 4\pi\frac{\Delta\lambda_M}{\lambda}\frac{V}{(\lambda/n_{ref})^3}$, and the total spontaneous emission ratio $F^{'} \approx NF_0$ approaches unity, as expected [127].

For a dielectric cavity, in addition to the discrete cavity modes, the emitter also can couple to a continuum of radiative modes, which cannot be neglected. Thus, Eq. 4.5 should be corrected as

$$F = \frac{\Gamma_{sp}}{\Gamma_{sp,free}} = \sum_{i=0}^{N-1} F_i + \zeta \tag{4.7}$$

where ζ denotes the ratio of the emitter's emission rate coupled to these radiative modes with respect to the emission rate in the homogeneous medium. If mode 0 denotes the lasing mode, the spontaneous emission factor β can be expressed as

$$\beta = \frac{\Gamma_{sp,0}}{\Gamma_{sp}} = \frac{F_0}{\sum_{i=0}^{N-1} F_i + \zeta} = \frac{F_0}{\alpha} \tag{4.8}$$

where α is defined as $\alpha = \sum_{i=1}^{N-1} F_i + \zeta$, which represents the spontaneous emission coupled to all the non-lasing modes.

4.2.2 Rate equations and lasing threshold

In this subsection, the lasing threshold is analyzed from the laser rate equations [115],

$$\begin{cases} \dfrac{dN}{dt} = \dfrac{\gamma_{in}\tilde{F}_{in}}{V} - \Gamma G(N)P - \dfrac{N}{\tau_r} - \dfrac{N}{\tau_{nr}} \\ \\ \dfrac{dP}{dt} = \Gamma G(N)P - \dfrac{P}{\tau_c} + \beta\dfrac{N}{\tau_r} \end{cases} \tag{4.9}$$

where N and P are the carrier and photon density that are confined in the mode volume V. $\Gamma G(N)P$ represents the stimulated emission, where Γ is the confinement factor and $G(N)$ is the gain coefficient. τ_r and τ_{nr} are the carrier radiative and non-radiative lifetime respectively. τ_c is the photon's cavity lifetime. $\tilde{F}_{in}$ is the pump flux (unit: s^{-1}) of either injected carriers or pumped photons, and $\tilde{F}_{out} = P/\tau_{out} \times V$ is the lasing output flux, where τ_{out} is the photon's out-coupling lifetime. Define γ_{in} as the pumping efficiency, and $\gamma_{out} = \tau_c/\tau_{out}$ as the output coupling efficiency. At steady state, Eq. 4.9 can be written as,

$$\begin{cases} \dfrac{\gamma_{in}\tilde{F}_{in}}{V} = \Gamma G(N)P + (F_\circ + a)\dfrac{N}{\tau_{r,free}} + \dfrac{N}{\tau_{nr}} \\ \\ \dfrac{\tilde{F}_{out}}{\gamma_{out}V} = \dfrac{P}{\tau_c} = \Gamma G(N)P + F_\circ\dfrac{N}{\tau_{r,free}} \end{cases} \tag{4.10}$$

Solving Eq. 4.10 leads to

$$P = F_\circ\frac{N}{\tau_{r,free}}[\frac{1}{\tau_c} - \Gamma G(N)]^{-1} \tag{4.11}$$

It is evident from Eq. 4.11 that, at steady state, the photon generation rate from the stimulated emission cannot exceed the photon cavity loss rate. Here define the saturation carrier density (N_s) that satisfies the following equation, $\Gamma G(N_s) = \frac{1}{\tau_c} = \frac{\omega}{Q}$. As the carrier density approaches N_s, the photon gain rate approaches the cavity loss rate, and the stimulated emission term overtakes other contributions in

the rate equations. In this saturation limit, all the pumped carriers predominantly recombine and emit to the lasing mode through stimulated emission, which results in a differential internal quantum efficiency of unity, or a linear light-in light-out (L-L) curve. In classical laser theory, this effect is also referred as "gain clamping" or "gain saturation" effect [128]. The rate equations in the saturation limit can be modified to

$$\begin{cases} \dfrac{\gamma_{in}\tilde{F}_{in}}{V} = \Gamma G(N_s)P + (F_\circ + a)\dfrac{N_s}{\tau_{r,free}} + \dfrac{N_s}{\tau_{nr}} \\ \\ \dfrac{\tilde{F}_{out}}{\gamma_{out}V} = \dfrac{P}{\tau_c} = \Gamma G(N_s)P + F_\circ\dfrac{N_s}{\tau_{r,free}} \end{cases} \tag{4.12}$$

The classical lasing threshold is defined as the pump level of the kink in L-L curve. From Eq. 4.12, the classical lasing threshold can be deduced as

$$\tilde{F}_{th,classical} = [(\sum_{i=1}^{N-1} F_i + \zeta)\frac{N_s}{\tau_{r,free}} + \frac{N_s}{\tau_{nr}}]V/\gamma_{in} \tag{4.13}$$

From Eq. 4.13, it is evident that the lasing threshold is dependent on multiple factors: (1) mode volume: the threshold scales linearly with mode volume; (2) saturation carrier density: N_s is inversely proportional to the Q factor. A high-Q cavity is desired to reduce N_s, though an ultrahigh-Q ($\sim 10^6$) is not necessary; (3) coupling to other cavity modes: this term can be eliminated by properly designing a single-mode PhC cavity; (4) coupling to radiative modes: ideally one needs an omni-directional PBG, that is a 3D-PhC cavity, to eliminate this term [129]. However, an incomplete PBG has also been shown to be able to largely suppress this radiative coupling [130]; (5) non-radiative recombination: most of the non-radiative recombination in a PhCL arises from surface recombination and Auger recombination. For QW-based PhCLs, Surface recombination is especially prominent because of the many perforated holes in PhC structures; and (6) external pump efficiency. From Eq. 4.13, it is interesting to notice that, the classical lasing threshold is independent of the cavity mode's Purcell factor $F_\circ$, though a

high F_0 results in a large β factor.

It is also important to mention that there is another definition of the lasing threshold [131], which corresponds to the pump level at which the number of stimulated emitted photons starts to exceed the number of spontaneously emitted photons. In contrast to the classical threshold definition, this threshold is referred as "quantum threshold". From Eq. 4.10, the quantum threshold can be deduced,

$$\tilde{F}_{th,quantum} = [(2F_0 + \sum_{i=1}^{N-1} F_i + \zeta)\frac{N_s}{\tau_{r,free}} + \frac{N_s}{\tau_{nr}}]V/\gamma_{in} \tag{4.14}$$

where N_q satisfies $\Gamma G(N_q) = \frac{1}{2\tau_c} = \frac{\omega}{2Q}$. It has a similar form as Eq. 4.13, with the exception that the quantum threshold increases as Purcell factor increases. This counter-intuitive effect can be explained as follows: at the quantum threshold condition, there are an equal number of photons emitted by spontaneous as by stimulated emission. The Purcell effect accelerates the spontaneous emission into the cavity mode. In order to reach the threshold condition for lasing in the presence of this effect, it is thus necessary to also increase the rate of stimulated emission.

To conclude, the ultimate low-threshold laser requires a cavity with small mode volume, relatively high Q factor, single-mode operation, and high pumping efficiency. PhC cavities, with their flexibility in engineering the photonic band, offer the possibility to approach this ultimate goal.

4.3 Photonic crystal nanobeam lasers

Photonic crystal nanobeam cavity is a type of 1D-PhC cavities. It is based on a ridge dielectric waveguide, with an array of perforated holes on top that form a PBG mirror [132]. Photonic crystal nanobeam lasers [133–135] recently have attracted a lot of interests because they can achieve high Q/V factors while occupying smaller footprints than 2D-PhC [136, 137] and 3D-PhC lasers [129]. Furthermore, nanobeam cavities can be designed to have no mode degeneracy, compared

with other designs [125, 138, 139]. This is crucial for nanolasers to operate in the single-mode regime, which is the key to achieving a large β factor and the reduction of lasing threshold.

4.3.1 Material system

There are many promising ways to realize a nanobeam photonic crystal laser. The one described here features semiconductor quantum wells (QWs) lattice-matched to an InP wafer. The QWs provide the optical gain. They contain four 8nm-thick compressively-strained $In_{0.58}Ga_{0.42}As$ layers, which are sandwiched in a 326nm thick $In_{0.53}(Al_{0.4}Ga_{0.6})_{0.47}As$ slab. Below the semiconductor QW slab, there is a 2μm thick InP sacrificial layer for selective wet etching. All the layers are grown with metal-organic chemical-vapor deposition (MOCVD) technique to minimize the crystalline defects [140].

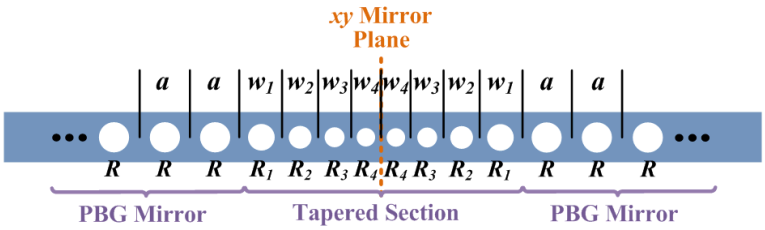

Figure 4.3.1: Layout of the material system of the semiconductor QWs sample used to realize nanobeam laser. The energy band of the semiconductor QWs are sketched on the right hand side.

The ratio of III-V components in the semiconductor QWs results in a 0.32% in-plane compressive strain while satisfying the lattice-matching condition. This compressive strain shifts the heavy-hole (HH) state to lie on top of the light-hole (LH) state, which leads to a dominantly TE-polarized gain. The TE-polarized modes favor vertical light emissions compared to the TM-polarized modes, and therefore are more suitable for surface-emitting lasers. Fig. 4.3.2(b) shows the photoluminescence (PL) spectrum of the sample. The emission spectrum ranges

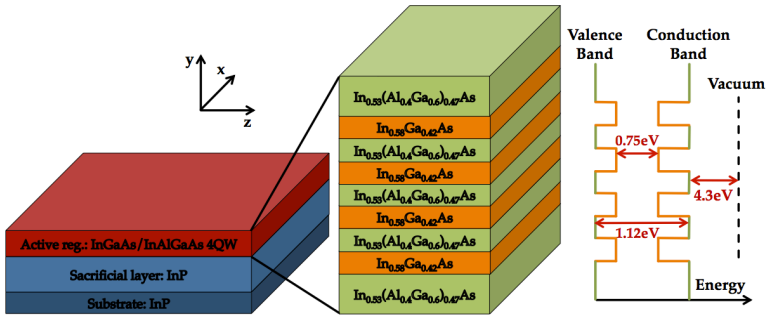

Figure 4.3.2: (a) Energy band diagram of electrons, light holes (LH) and heavy holes (HH) bands of the semiconductor QWs. (b) The PL emission spectrum of the quaternary QWs peaks at about 1.59μm.

from 1.40μm to 1.65μm, and peaks at 1.59μm.

4.3.2 Cavity design

The photonic crystal nanobeam design is based on a suspended ridge waveguide with an array of identical holes, which forms a PBG mirror. The refractive index of the dielectric is 3.5 (the index of InAlGaAs/InGaAs QWs at 1.55μm). The ridge is 500nm wide and 330nm thick, the periodicity of the holes is a = 400nm, and the hole's radius is set to be $r = 0.3a$ to optimize the bandgap.

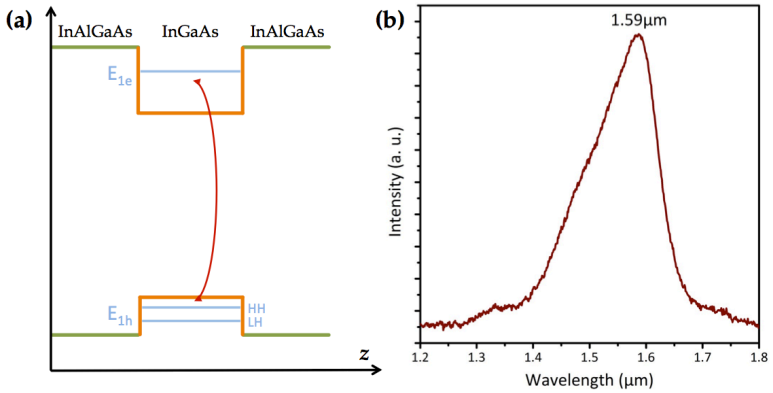

Figure 4.3.3: Layout of the photonic crystal nanobeam cavity design.

Introducing a lattice grading to the periodic structure creates a localized poten-

tial for the fundamental TE-polarized mode. To optimize the mode's Q factor, the bandgap-tapering technique [90, 141] is employed for suppressing the scattering losses that take place at the interface between the cavity section and the mirror section [56]. This design contains a four-segment tapered section with holes $R_1 - R_4$ and a 12-segment mirror section at each side of the cavity, as shown in Fig. 4.3.3. Two degrees of freedom are available to modify each tapered segment: the width w_k and the radius r_k. We keep the ratio r_k/w_k fixed at each segment and implement a linear interpolation of the grating constant $2\pi/w_k$. When the central segment w_4 is set to $0.72a$, a cavity mode is obtained to resonate at $1.59\mu m$ with an ultrahigh Q factor above $8,000,000$, and a very small mode volume of $0.28(\lambda/n)^3$ [Fig. 4.3.4(a)]. The ultrahigh Q factors can also be explained by looking at the momentum space of the cavity mode. Fig. 4.3.4(b) and (c) demonstrate the spatial Fourier transformation (FT) of the electric field components E_x and E_z in the xz plane ($y = 0$), with the light cone indicated by the white circle. It can be seen that both modes' Fourier components are localized tightly at the bandedge of the Brillouin zone on the k_z axis: $k_z = \pi/a$. This minimizes the amount of mode energy within the light cone that is responsible for scattering losses [71].

In addition to this fundamental mode, the cavity supports another mode at a longer wavelength $1.72\mu m$ with a larger mode volume of $0.67(\lambda/n)^3$. This is an extended mode with a node at the center of the cavity, as shown in Fig. 4.3.4(d). This mode resonates at a wavelength outside the gain spectrum of the quantum wells, and therefore does not affect the single-mode operation of our laser.

4.3.3 Fabrication

The nanobeam pattern is defined using a negative e-beam lithography resist [Hydrogen Silsesquioxane (HSQ)]. The e-beam resist is spun on the surface with a spinning speed of 3000rpm resulting in a thickness of $\sim 100 - 150$nm. The resist is subsequently cross-linked using a STS Elionix ELS-7000 e-beam writer at an acceleration voltage of 100kV and a beam current of 100pA.

Next, the pattern is transferred to the substrate with inductively coupled plasma

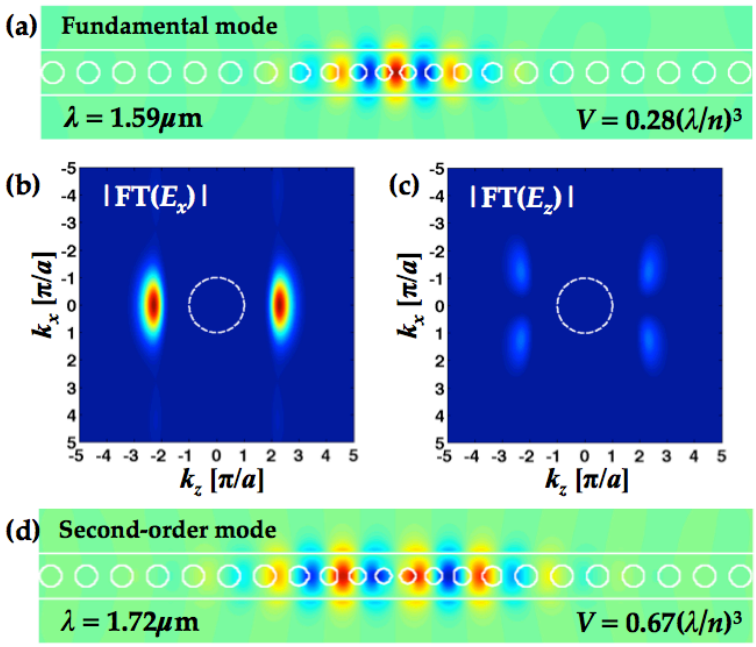

Figure 4.3.4: (a) Mode profile of the fundamental cavity mode of the nanobeam laser. (b)(c) Spatial Fourier transform of the electric field component E_x and E_z at $y = 0$ plane. (d) Mode profile of the second-order mode, resonating at a higher wavelength, outside the gain spectrum.

reactive ion etching (ICP-RIE) using $BCl_3/CH_4/Ar/HBr$ chemistry at 180°C. This anisotropic etching creates a mesa extended to the sacrificial layer. Hydrofluoric acid (HF) is then used to dissolve the e-beam resist. Finally the InP sacrificial layer is selectively wet-etched by $HCl:H_2O = 3:1$ solution. The crystal orientation dependent etch rate is about $100 - 120$nm/s at 8°C, which leads to an etch time of 40s for a completely suspended nanobeam structure. Fig. 4.3.5 shows the scanning electron micrographs of an array of fabricated nanobeam lasers. The two pads are designed to support the suspended PhC structures.

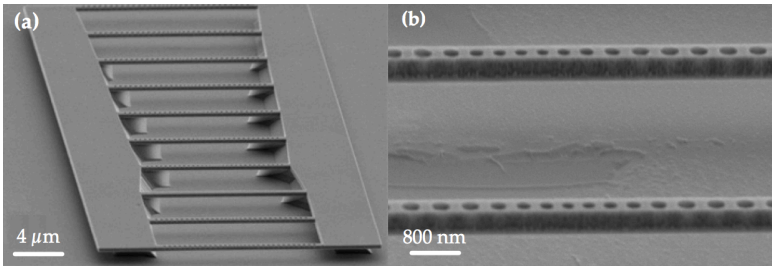

Figure 4.3.5: Scanning electron micrographs of the fabricated photonic crystal nanobeam lasers.

4.3.4 Characterization

The devices are optically pumped at room temperature using a 660nm pulsed laser diode. The pulse width is 9ns at a 300kHz repetition rate, which corresponds to a duty cycle of 0.27%. The pump beam is focused to the sample surface via a 100X objective lens, and the emitted light is collected via the same objective lens and analyzed using optical spectrum analyzer (OSA), near-infrared (NIR) camera, and a InGaAs detector.

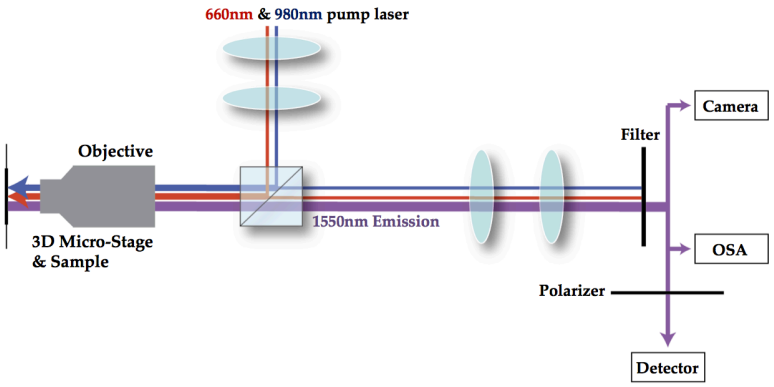

Figure 4.3.6: Illustration of the characterization setup.

In Fig. 4.3.7(a) we show the *L-L* (Light-in, Light-out) curve for one of the measured devices. It can be seen that there is no pronounced kink near the threshold. This soft turn-on of the laser indicates a large β factor. The lasing images taken at different pump levels, using the NIR camera, show that the emission spot is well

confined to the center of the nanobeam, which unambiguously proves that the lasing is from the localized defect mode. Fig. 4.3.7(b) shows the lasing spectrum near the threshold. The spectrum is fitted with a Lorentzian function with a full-width half-maximum (FWHM) of 0.11nm, which corresponds to a Q factor of 15, 000. The Q factor is likely limited by the resolution of the OSA used.

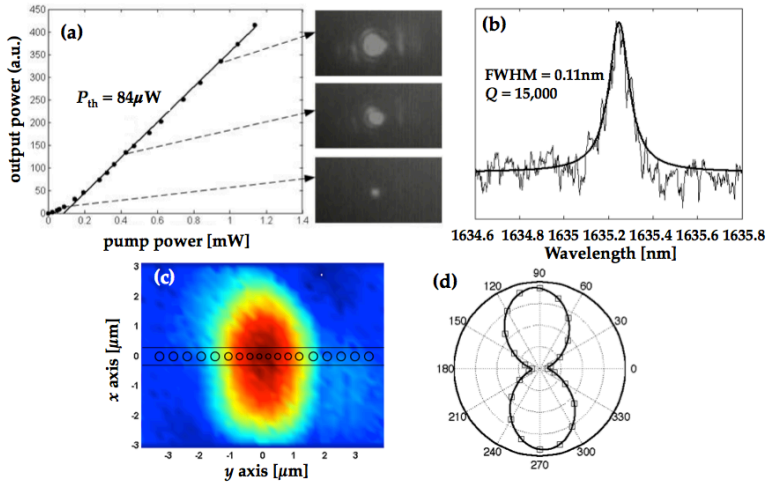

Figure 4.3.7: (a) Laser emitted power as a function of the incident pump power. The emission profiles obtained from the camera at different pump levels are shown on the right. (b) The spectrum of the emitted light near the threshold. (c) Output lasing power as a function of the pump beam position. The pattern of the nanobeam is superimposed as the background of the picture. (d) Polarization dependence of the lasing mode.

In addition, Fig. 4.3.7(c) shows the dependence of the output power on the pump beam position by scanning the sample in xy plane using a piezo-actuated stage with a spatial resolution of 6nm. As the pump beam is moved away from the center of the cavity, the beam intensity decreases rapidly and finally vanishes. This is a further confirmation of emission from the localized mode of the cavity instead of extended band-edge emission. Here the pump spot is much bigger than the cavity mode, so the cavity mode samples the pump beam. Therefore, Fig. 4.3.7(c) shows the shape of the pump spot as opposed to the profile of the lasing mode. This also allows us to evaluate the effective pump power, that is, the overlap of the pump

beam with the nanobeam, which is reported in Fig. 4.3.7(a). An effective threshold of 84μW is evaluated for this nanobeam laser, whereas the total power threshold measured behind the objective lens is 812μW. The threshold power is even smaller, considering that not all the pump power incident onto the nanobeam is absorbed by the cavity. Finally, Fig. 4.3.7(d) shows the polarization dependence of the laser emission. The emission is polarized along x-axis as expected, and exhibits a large polarization ratio of $\sim$ 10.

Next, the behaviors of this photonic crystal nanobeam laser is analyzed by fitting to the rate equation that is similar to Eq. 4.10,

$$\begin{cases} \dfrac{\gamma_{in}\tilde{F}_{in}}{V} = \Gamma G(N)P + AN + (F_o + \zeta)BN^2 + CN^3 \\ \\ \dfrac{\tilde{F}_{out}}{\gamma_{out}V} = \dfrac{P}{\tau_c} = \Gamma G(N)P + F_o BN^2 \end{cases} \tag{4.15}$$

where AN, $(F_o + a)BN^2$ and CN^3 represent the carrier loss rate through surface recombination, radiative recombination and Auger recombination, respectively. For this nanobeam cavity, ζ is evaluated as 0.91 through FDTD simulation. The lasing mode's Purcell factor is estimated to be $\sim$ 26, with taking into account the QW's homogeneous broadening at room temperature and the spatial overlap between the active medium and the optical mode. For other parameters, typical values for InP-based quantum wells at room temperature are applied [142].

Fig. 4.3.8 shows the measured L-L in log-log scale along with curves obtained from rate equations for different Purcell factors and spontaneous emission factors (β). It can be seen that the experimental data are in excellent agreement with the theoretical prediction of $F_o \sim 25$ and $\beta = 0.97$. This is in good agreement with the theoretical estimation of Purcell factor.

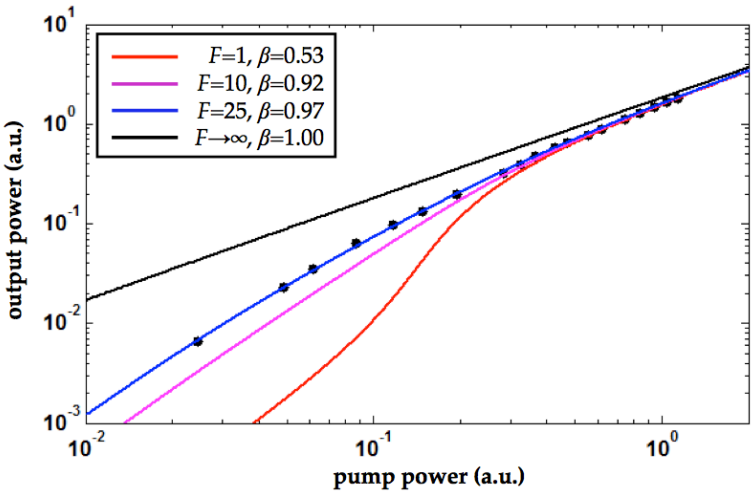

Figure 4.3.8: Log-log plot of the *L-L* curve (dots), with predictions from the rate equations using different β factors (solid lines).

4.4 Photonic crystal disk lasers

PhCLs based on 1D-PhC nanobeams and 2D-PhC slabs have proved to make good surface-emitter nanolasers with low threshold and high modulation speeds, but they have a few drawbacks. First, the footprint of the photonic crystal lasers is limited by the multiple periodic Bragg layers used to confine the cavity mode. Second, most photonic crystal cavities rely on suspended semiconductor membranes to provide a good index contrast, which makes efficient electrical injection of carriers into the cavity mode difficult. Microdisk lasers [143], on the other hand, rely on whispering gallery mode pinned via total internal reflection to the boundary of the disk. They offer a platform for very compact electrically-driven lasers, with footprint on the order of optical wavelength [144–146]. However, the whispering gallery mode travels through the whole circular edge of the microdisk, and therefore results in a relatively large mode volume [Fig. 4.4.1(c)]. Furthermore, the whispering gallery mode does not emit vertically, which makes the collection of photons difficult [147]. Normally evanescent coupling via a tapered fiber is used to collect the emitted photons efficiently [144]. This makes integration of large arrays

of microdisk lasers problematic. To overcome this, vertically-emitting microdisk laser uses a second-order metallic grating atop to extract the light out [148].

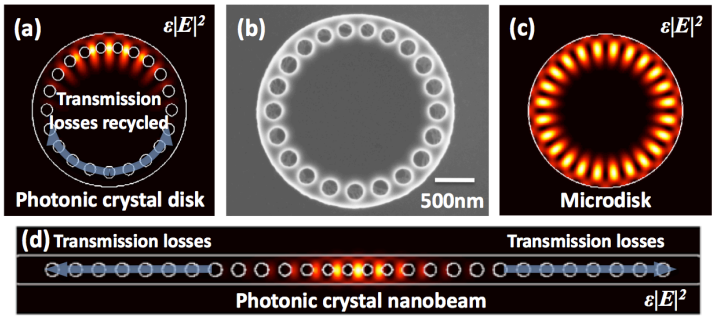

Figure 4.4.1: (a) Schematic of photonic crystal disk laser and (b) fabricated photonic crystal disk laser. The device can be viewed as a hybrid between (c) microdisk laser and (d) photonic crystal nanobeam laser with photonic crystal folded back to minimize the transmission losses.

In this section, we demonstrate nanolasers operated at room temperature based on a novel type of nanocavities, which combines the properties of microdisk and photonic crystal lasers. It incorporates an array of holes at the perimeter of the microdisk, in order to confine the whispering gallery mode in a limited angular range within a small mode volume. The design can also be understood as a photonic crystal nanobeam cavity [Fig. 4.4.1(d)] [133–135] bent into a disk [Fig. 4.4.1(a)]. In this way, Bragg mirrors at each end of the nanobeam are combined in one curved Bragg mirror. Therefore, the number of holes can be decreased because the transmission losses are cycled through the disk, which reduces the device footprint.

We start our design with a 2.56μm diameter, 325nm thick microdisk that supports a resonance of $TE_{1,10}$ mode at 1750nm. Next, we add 20 holes with equal angular spacing around the perimeter of the disk. This causes the two degenerate $TE_{1,10}$ modes, which propagate in clockwise and counter-clockwise direction, to split into two standing-wave modes: one mode with its field concentrated in the dielectric whereas the other in the hole region, as shown in Fig. 4.4.2(b) and (c). These modes are similar to the modes of microgear cavities [149]. In anal-

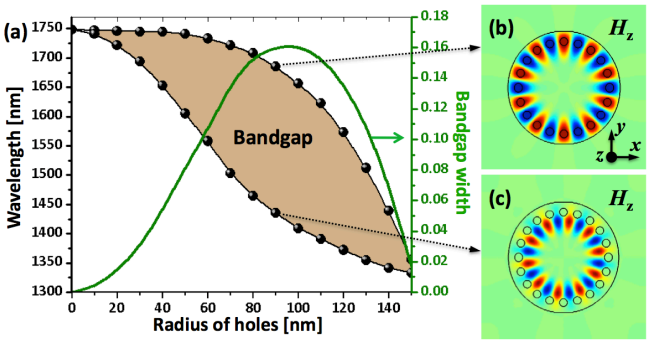

Figure 4.4.2: (a) Bangedge wavelength as a function of the radius of holes on photonic crystal disk (black), with the bandgap shaded in bronze. The green curve shows the corresponding normalized bandgap width. (b)(c) Resonant mode profiles at bandedge of H_z component, for dielectric-band (b) and air-band mode (c), respectively.

ogy to photonic crystals, these two modes correspond to the dielectric band-edge and air band-edge. Between these bandedges, the propagation of $TE_{1,10}$ mode is forbidden. In order to maximize the bandgap width, and thereby optimize the azimuthal confinement, we place the center of the holes at electric field maximum. Fig. 4.4.2(a) shows the band-edge wavelength and normalized bandgap width (ratio of the gap width to the midgap wavelength) as a function of the hole radius. It can be seen that the bandgap is maximized at 97nm, and the center of the bandgap is at $\sim$ 1550nm. We emphasize that the bandgap is not complete: there are higher-order modes with different radial field distribution that may exist in the wavelength of interest.

Next, we introduce the defect region to the disk, by modifying the hole-to-hole angular spacing as well as the holes' radii. The final structure is shown in Fig. 4.4.1(b), where there are 11 identical holes on the bottom half acting as Bragg mirrors, and 10 tapered holes on the top half to localize the mode while suppressing the scattering losses [90]. The cavity mode resonates at 1546nm, and, without considering material losses, has a Q factor of 1.0×10^5, and a modal volume of $0.52(\lambda/n)^3$. The mode volume is on the same order of photonic crystal nanobeam cavities [133–135].

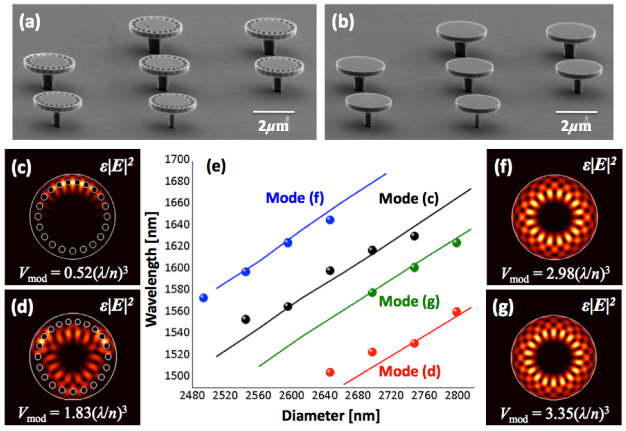

Figure 4.4.3: (a)(b) Images of photonic crystal disk and microdisk lasers with different scaling factors. (c)(d) Electric field density profiles of photonic crystal disk modes. (e) Experimental results of lasing wavelength dependence on diameter of photonic crystal disks (black-dot and red-dot) and microdisks (blue-dot and green-dot). The solid curves show the mode wavelength dependence obtained using simulations. (f)(g) Electric field density profiles of microdisk modes.

Our cavities are fabricated on commercial InP substrate. A 325nm thick $In_{0.53}(Al_{0.4}Ga_{0.6})_{0.47}As$ layer is epitaxially grown atop using metal-organic chemical vapor deposition. It contains four compressively strained $In_{0.58}Ga_{0.42}As$ quantum wells, which support TE-polarized gain covering the wavelength range from 1480nm to 1650nm. The pattern is defined with electron-beam lithography. The pattern is subsequently transferred to $In_{0.53}(Al_{0.4}Ga_{0.6})_{0.47}As$ slab and InP substrate with inductively coupled plasma reactive ion etching. The disk structure is finally realized by selectively wet etching the mesa with $3:1$ $HCl:H_2O$ solution [Fig. 4.4.3(a)]. We also fabricate microdisk without perforated holes with the same diameter to compare the results [Fig. 4.4.3(b)]. The two arrays are scaled linearly in size to vary the cavities' resonant wavelengths.

The devices are optically pumped at room temperature using a 980nm semiconductor laser, with 10ns pulses and 400kHz repetition rate. The pump beam is focused to a $3\mu m$ diameter spot using a 100X objective lens. The effective pump power is estimated with power measurement after the objective, while taking in

account the spatial overlap between the pump beam and the lasing mode. The emission beam is collected through the same objective lens from the top, and analyzed with an InGaAs detector filtered by a monochromator.

For both photonic crystal disks and microdisks, Fig. 4.4.3(e) depicts the lasing wavelength as a function of the diameter of the disk, where modes (c) and (d) are photonic crystal disk modes, and modes (f) and (g) are microdisk modes. It shows good agreement with simulation results plotted in solid lines, which verifies the lasing mode (c) is of the designed defect mode. We note that by controlling the position of the pump spot, lasing from two different photonic crystal disk modes could be obtained in some structures [Fig. 4.4.3(e)]. The nanolaser, however, does operate in single-mode regime in both cases (only one mode lases at one time). We also note that the two microdisk lasing modes are not the fundamental $TE_{1,m}$ modes, but the higher-order $TE_{2,8}$, and $TE_{2,9}$ modes. These modes have a node of electric field in the radial direction. The fundamental modes cannot be collected from top, because it emits in in-plane directions [147].

Next, we study the properties of the designed photonic crystal disk mode from one single device [Fig. 4.4.4(a)]. Fig. 4.4.4(b) shows the lasing power as a function of the effective pump power (also known as *L-L* curve), in comparison with a microdisk laser emitting at the same wavelength. The injection efficiencies are estimated to be 1.74% and 4.36% for photonic crystal disk mode and microdisk mode, respectively. From Fig. 4.4.4(b), the photonic crystal disk lasers have much better extraction efficiencies than microdisk lasers. We believe that this efficiency can be further boosted with subtle far-field engineering of photonic crystals [150]. Inset plots the spectrum at 3.2 times the threshold power of photonic crystal disk mode, which shows clear single-mode lasing emission. In Fig. 4.4.4(c) we plot the *L-L* curve for the photonic crystal disk laser in log-log scale (black dots), along with the L-L curves obtained from rate equations for different spontaneous emission factors (β). The experimental data show good agreement with a β factor of 0.087. More than ten-fold reduction in β-factor of this laser compared to nanobeam laser [133] can be attributed to the existence of higher-order modes. In Fig. 4.4.4(d)

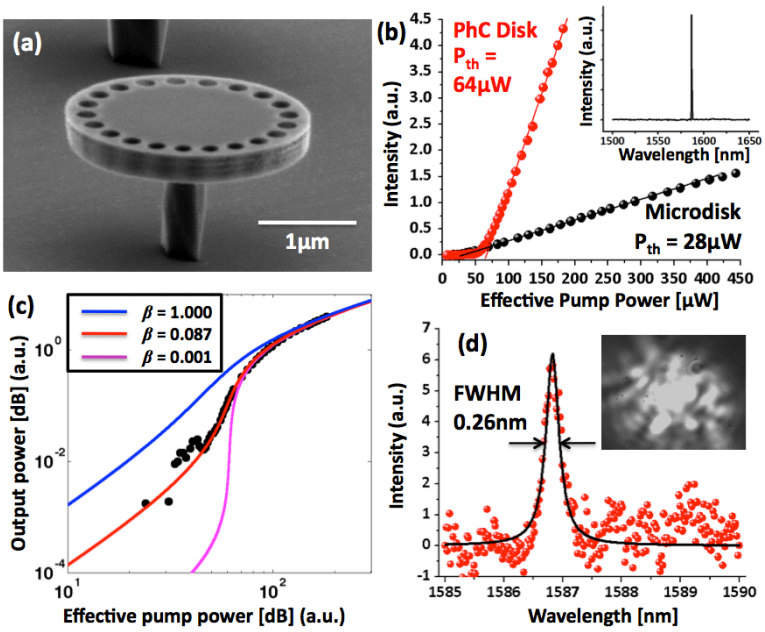

Figure 4.4.4: (a) Images of fabricated photonic crystal disk from scanning electron microscope. (b) Light-in light-out curve for photonic crystal disk laser and microdisk laser, respectively. Inset shows the spectrum of photonic crystal disk lasers at 3.2× lasing threshold. (c) Log-log plot of the photonic crystal disk laser's L-L curve (black-dots). The solid curves show L-L curves deduced from rate equations with different β factors. (d) Lineshape of the lasing mode above threshold (red-dot), fitted with a Lorentzian line function (red-solid). Inset shows the emission profile taken from an infrared camera.

we show the lasing spectrum of the photonic crystal disk lasers slightly above the lasing threshold (1.1×threshold). It has a full-width half-maximum (FWHM) of 0.26nm, which corresponds to a Quality factor of $\sim$ 6000. The Quality factor is limited by the resolution of the monochromator. Free-carrier absorption is also known to decrease the Q factor extensively below its passive value [144]. We also show the lasing emission profile of the photonic crystal disk laser in the inset of Fig. 4.4.4(d), which is taken from a near-infrared camera. Finally, we note that linewidth narrowing effect above threshold could not be observed, due to the strong heating effects in nanolasers, as previously reported [134].

In summary, we have demonstrated a novel type of photonic crystal lasers,

which takes advantage of both microdisk and photonic crystal geometries, and has a small footprint, small mode volume, and high extraction efficiency.

4.5 Graphene-contacted micro-LED

4.5.1 Introduction

Developing an electrically driven nanolaser is critical to making nanolaser a competitive technology. However, most of the nanolasers previously reported were optically pumped with another laser diode, with few exceptions [107, 114]. The big obstacle lies in configuring the electrical contacts to the optical cavity in order to effectively inject carriers into the cavity mode, but the large absorption of conventional metal or indium tin oxide (ITO) contacts will degrade the cavity's Quality factor dramatically, and prevent the lasing behavior.

Graphene, the one-atomic-thick layer of carbon atoms that are aligned in a honeycomb crystal lattice, on the other hand, has both high optical transparency over visible and infrared wavelengths and high electrical conductivity, and thus is an ideal material candidate for transparent conducting electrodes. Graphene has already been applied in devices, such as light emitting diodes [151], photovoltaic cells [152], and liquid crystal displays [153]. In addition, graphene has extremely high mechanical flexibility, and can conform to a patterned surface over large areas. Therefore, we believe, graphene could provide a promising solution to electrically driven nanolasers. In this section, we first demonstrated graphene-contacted LEDs based on microdisk structures.

4.5.2 Preparation and characterization of graphene

Our graphene is grown on single-crystalline copper foil with chemical vapor deposition [154]. A thin layer of PMMA (495-A4) is spun onto the graphene, and the PMMA/graphene film is then released in a copper etchant ($FeCl_3$) bath, and subsequently transferred onto the receiving substrate in deionized water environ-

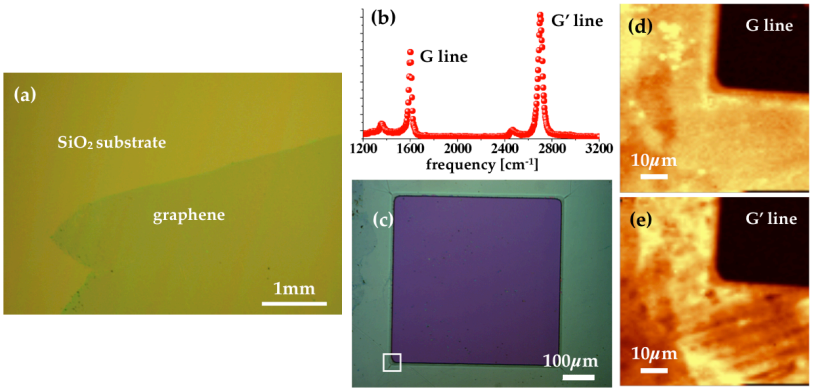

Figure 4.5.1: (a) Optical microscopic image of a graphene sheet transferred on a SiO_2 substrate. (b) Confocal Raman spectrum of monolayer graphene. (c) Optical micrograph of a photo-ligrography-patterned graphene after O_2 plasma treatment. (d)(e) Confocal Raman mapping of the patterned graphene. The Raman signal is spectrally integrated at G line and G' line resepctively. The white square in Fig. 4.5.1(c) indicates the spatial scanning range.

ment. Finally, the PMMA layer could be gently removed with acetone vapor.

In Fig. 4.5.1(a), we show the optical microscopic image of a graphene sheet transferred on a SiO_2 substrate. The substrate area with graphene atop shows a slightly different color compared to the bare substrate area. The quality of the graphene is tested using confocal Raman spectroscopy. The Raman signal is obtained with a pump laser of $\lambda = 532\text{nm}$ focused on the substrate. Fig. 4.5.1(b) shows the Raman spectrum of the transferred graphene on SiO_2 substrate, with two pronounced peaks identified as the G band at 1580cm^{-1} and the G' band at 2700cm^{-1}. The low G to G' peak intensity ratio (~ 0.7) and the narrow linewidth of the G' line ($\sim 45\text{cm}^{-1}$) are signatures of monolayer graphene [155].

The graphene film can be patterned with lithography and oxygen plasma treatment (20 sccm, 100 watt, 1 minute), as shown in Fig. 4.5.1(c). Confocal Raman mapping of the patterned graphene, demonstrated in Fig. 4.5.1(d) and (e), verifies the graphene exposed to O_2 plasma is etched away. The Raman signal is spectrally integrated at G line and G' line respectively. The spatial scanning range is indicated

by the white square in Fig. 4.5.1(c).

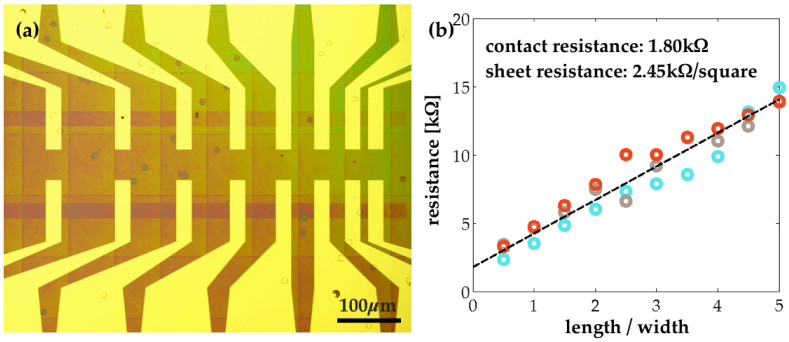

Figure 4.5.2: (a) Optical micrograph of patterned graphene stripe for resistivity measurement. (b) Graphene resistance of various lengths. The width of the stripe is fixed at 100μm. The black dash line shows the linear fitting of the measured data, resulting in a graphene resistivity of 2.45kΩ/square, and a contact resistance to be 1.80kΩ.

Next, we characterize the electronic properties of the graphene film. The receiving substrate is a silicon substrate covered with a 500nm thick SU-8 photoresist that acts as the insulating layer. In order to measure the resistivity of graphene, the graphene is patterned into a 100μm wide stripe, as shown in Fig. 4.5.2(a). The resistance of the graphene stripe whose length varies from 50μm to 250μm is measured with palladium / gold (25nm / 150nm) contact. By fitting the resistance measured with various length / width ratio, as shown in Fig. 4.5.2, the resistivity of graphene is evaluated to be 2.45kΩ / square, and the contact resistance to be 1.80kΩ.

4.5.3 Fabrication and measurement of graphene-contacted micro-LED

We adopt the simple prototype of microdisk structures to demonstrate graphene-contacted light-emitting devices. Fig. 4.5.3(a)-(d) shows the fabrication procedure of the proposed graphene injected micro-LED. The heterostructures have been grown epitaxially on n-doped InP substrates by metalorganic chemical vapor deposition, in order to provide the optical gain of the laser. A heavily p-doped

InP/InGaAs layer caps the quantum wells to provide efficient hole injection.

First, the microdisk with a radius of $2.2\mu m$ is defined with negative HSQ e-beam resist (Dow Corning Co., XR-1541). The pattern is transferred to the substrate with reactive ion etching. The etching depth is measured by scanning electron microscopy to be $\sim$ 750nm. Next, a 650nm thick SiO_2 layer and a 100nm thick Ti(10nm) / Au(80nm) / Pd(10nm) metal contact are deposited around the micropost, to provide the top contacts that are insulated from the substrate. The distance between the microdisk and the SiO_2 / metal sidewall is kept to be of $2-4\mu$m. At this distance, the metal does not affect the optical mode. Subsequently, the microdisk is finalized with selective wet etching in $HCl/H_2O = 3:1$ bath at 4^oC for 2 minutes. The thin post supporting the microdisk also provides the current path for electrical injection. Finally, a PMMA/graphene film is transferred to the sample, and patterned by e-beam lithography and oxygen plasma. Fig. 4.5.3(e) and (f) show the scanning electron micrograph and optical micrograph of the microdisk after wet etching. Fig. 4.5.3(g) shows the configuration of the final sample with patterned graphene on top.

We characterize the I-V characteristics of the fabricated microdisk structure. DC voltage is applied between the Au contact and the bottom of the substrate. The I-V curve of the the microdisk structure, as shown in Fig. 4.5.4, is in consistence with the p-i-n diode. We collect light emission from the microdisk with 100X objective lens, and monitor with an IR camera. The emission images are shown in the inset of Fig. 4.5.4. The turn-on voltage of the electroluminescence is measured at 0.8 volts, and the intensity of the electroluminescence increases as the voltage increases. The edge of the SiO_2/Au sidewall at the vicinity of the microdisk can also be seen from light scattering.

4.6 Conclusion and outlook

In this chapter, we introduced the basic concepts needed for development of photonic crystal lasers. As illustrated by the rate equation analysis, PhC cavities are an

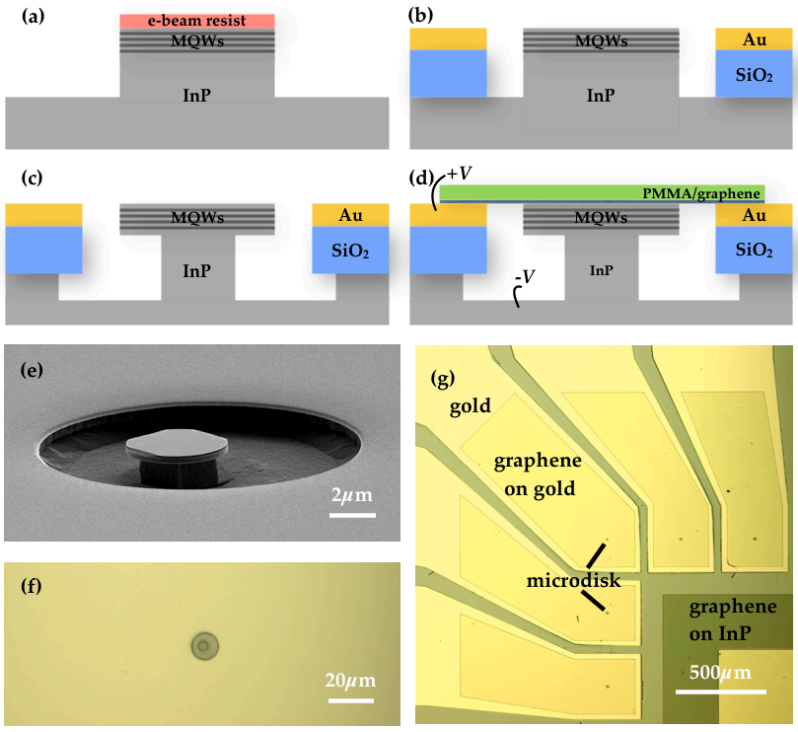

Figure 4.5.3: (a) The fabrication procedures of the graphene-injected microdisk laser. (b)(c) Scanning electron micrographs of the fabricated microdisk lasers, after wet etching (b), and graphene transfer (c).

ideal platform for the realization of the ultimate low-threshold nano-lasers, since they can support a single mode operation with a high Quality factor and a small mode volume across the gain spectrum. Furthermore, the high Q/V factor leads to strong cavity Purcell effect, which enables high-speed operation of directly-modulated lasers. Two examples of photonic crystal lasers, which operate with pulsed optical pumping at room temperature, are then demonstrated. The photonic crystal nanobeam laser shows a high spontaneous emission factor of 0.97 due to its single-mode nature; the photonic crystal disk laser has a small device footprint and higher collection efficiency than microdisk lasers.

During the last decade we witnessed rapid progress in the development of photonic crystal lasers: the reduced lasing threshold attributed to its PhC cavity's small mode volume and high Q factor [111, 113] and the nano-scale footprint, the

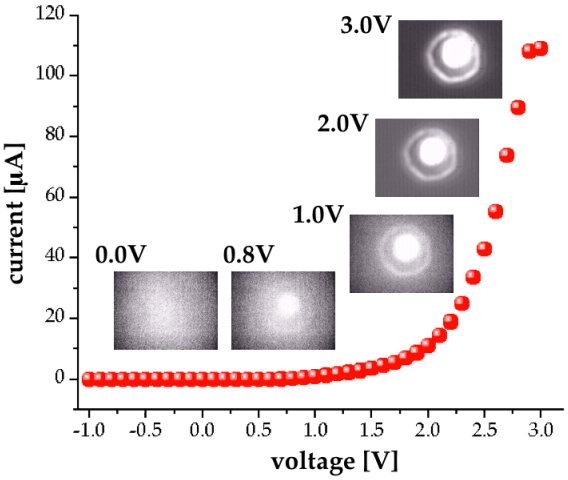

Figure 4.5.4: I-V characteristics of a microdisk device. Inset shows the emission image taken from an IR camera.

boosted modulation speed resulting from Purcell effect [109, 118], the controllable laser polarizations [119], the wavelength tunability integrated with optomechanics [121], and so forth. Extensive research has revealed interesting underlying physics, including the strong coupling limit of cavity QED [112], and has also inspired applications such as those in bio-chemical sensing [156].

Nevertheless, several challenges still remain to be solved. First, the current state-of-the-art technologies cannot produce photonic crystal lasers that operate at the designed wavelength, due to fabrication imperfections. This is especially important when the gain medium consists of quantum emitters with a very narrow gain spectrum (semiconductor QD, for instance). Second, while a couple of electrically driven PhCLs have been reported so far [107, 114], the reliable production of the large-scale electrically pumped PhCL array calls for more research efforts. Finally, PhCLs need to find a niche in the commercial market for applications ranging from bio-chemical sensors to on-chip interconnects.

5

Photonic crystal cavities at microwave frequencies

5.1 Introduction

Photonic crystal cavities with high Quality factors (Qs) are capable of extending the lifetime of cavity photons confined within mode volumes (V) of the order of a cubic-wavelength, and hence can greatly enhance the interaction between electromagnetic fields and matter. Recently, high Q/V photonic crystal cavities have been extensively investigated with various geometries at optical frequencies, acting as a powerful platform for studying cavity quantum electrodynamics (cQED) [157] and developing a myriad of nano-photonic devices. Yet few photonic crystal cavities have been reported at microwave frequencies [158–163].

A high Q/V microwave cavity is demanded for a number of applications. In

atomic physics, a single Rydberg atom coupled to a single photon is the fundamental system for cavity QED studies, especially when one reaches the interesting strong coupling regime where energy can be coherently exchanged between the two. For strong coupling to occur, the atom-photon coupling rate g (inversely proportional to square root of V) must exceed both the photon leakage rate (inversely proportional to Q) and the atom decoherence rate. Since the frequency difference of Rydberg states is in the microwave region [164], a high Q/V microwave cavity is crucial to achieve this type of coupling. Strong coupling in Rydberg atoms has been previously observed in large-scale Fabry-Perot cavities and superconducting circuits [164, 165]. Photonic crystal cavities, in contrast, offer an alternative platform that is more compact and can be operated at room temperature.

Secondly, given the cavity's intrinsic field enhancement factor, there are also significant advantages in practical applications such as tunable microwave filters and antennas, where the efficiency of a radiator can be significantly improved by coupling with the cavity mode [166]; fluorescence microscopy for biological systems, where a high Q/V microwave cavity can be used to control the temperature and drive the biological reactions [167]; resonance-enhanced microwave detectors [159]; particle accelerators [161, 162]; and refractive index sensors.

In this chapter, we have designed and experimentally demonstrated an all-dielectric photonic crystal microwave cavity. The cavity can be fabricated with a variety of materials using conventional machining techniques. We report a cavity mode at 17.4GHz with a very small mode volume limited to about one cubic-wavelength and a record-high Q-factor of $26,400$ at room temperature. Besides the high Q/V factor, the defect mode has a TM-polarized electric field concentrated in the air region [168], as opposed to most photonic crystal cavities designs with TE-polarized electric field concentrated in the host dielectric [141]. These features are crucial for effectively coupling microwaves to matter in a number of applications. Moreover, when a center-fed antenna is placed inside the cavity acting as a radiating dipole, we observe a strong signature of the cavity's Purcell enhancement factor. In summary, we believe this type of device offers great promise for studying cavity QED phenomena as well as for enabling novel applications at

microwave frequencies.

5.2 Design

The structure we propose starts from a so-called rectangular dielectric rod waveguide with a periodic array of circular holes, as shown in Fig. 5.2.1(a) [96, 97, 132, 133, 141]. We choose a refractive index of 3.1 for the rod, which corresponds to the refractive index of alumina (Al_2O_3) at microwave frequencies. The rectangular waveguide has an aspect ratio (thickness/width) of 2 : 1, and supports a fundamental TM-polarized mode with its major component aligned along the y-axis [Fig. 5.2.1(c)]. From our previous work [141], introducing a suitable periodic array of holes in the bulk materials of this high aspect-ratio waveguide results in a relatively wide bandgap for TM-polarized modes. Here we select the thickness to be $w = 4.72$mm, depth $h = 9.43$mm, and hole periodicity $a = 4.15$mm. The radius of the holes is chosen as $r = 1.25$mm.

Next, we introduce a defect region into the cavity by gradually increasing the periodicity (hole-to-hole distance) and hole diameter for each segment starting from a pair of outer holes and symmetrically moving towards the center. When the feature size of a segment is enlarged, the band-gap is red-shifted, resulting in a graded photonic band, as shown in Fig. 5.2.1(b). This allows confining an air-band mode in the defect region: the air-band mode is coupled to the evanescent Bloch modes within the band-gaps at each end, effectively trapping it between a pair of Bragg mirrors.

A three-dimensional finite-difference time-domain (FDTD) code was used to calculate the resonant frequency and the Q factor of the cavity mode. On each side of the cavity we introduce 10 segments with progressive tapering of the hole diameter and spacing, in order to adiabatically couple the cavity mode to the evanescent Bloch mode. This adiabatic process is tuned to suppress the scattering loss resulting from the effective index mismatch between the two modes [56, 90]. Without material losses, the cavity mode has an ultra-high Q factor of 2, 500, 000, limited by

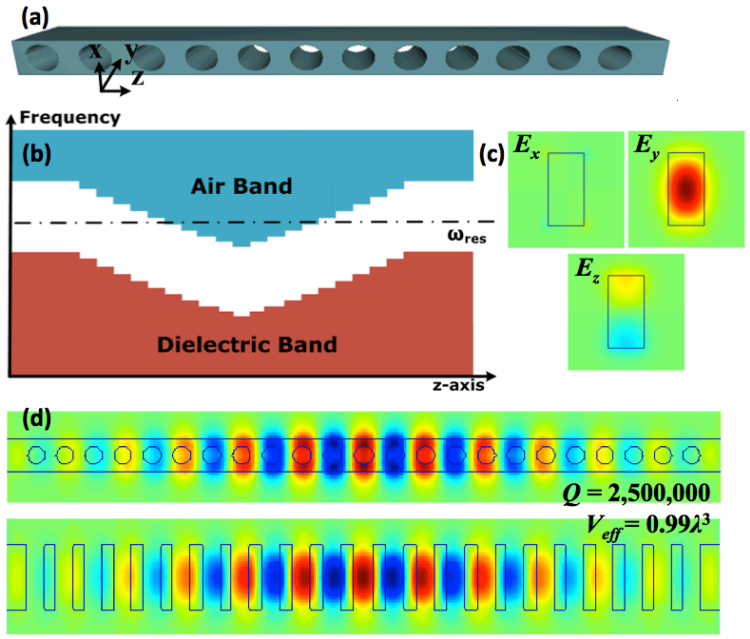

Figure 5.2.1: (a) Schematic of the device. (b) Diagram of tapered photonic bandgap. (c) Transverse mode profile of the fundamental TM-polarized mode. (d) Mode profile of the cavity mode.

scattering alone ($Q = Q_{sc}$). The cavity mode profiles are shown in Fig. 5.2.1(d), where the E_y component is plotted at the mirror plane of y-axis and x-axis, respectively. The tapered section's parameters are tailored to localize an air-band mode resonating at $17.4GHz$ by maximizing confinement along the z-axis, which results in a small cavity mode volume. As expected from the general features of air-band modes, the electric field concentrates in the air-region. However, the maximum of the electric field density $[\varepsilon |E|^2]$ is not in the air region, so we define the effective cavity mode volume as,

$$V_{\text{eff}} = \frac{\int \varepsilon |E|^2 \, dV}{|E_{\max,air}|^2} \tag{5.1}$$

where $E_{\max,air}$ is the electric field maximum in the air region, located at the center of the cavity. For our cavity we found an effective mode volume of $0.99\lambda^3$.

The cavity mode is normally excited from an external waveguide port. The amount of energy stored (U) is proportional to the launched power (P_o) [169],

$$U = \frac{2}{\omega_0}\frac{Q^2}{Q_w}P_0 \tag{5.2}$$

In Eq. 5.2 Q_w denotes the quality factor responsible for the field energy leakage from the cavity section via the dielectric waveguide. The total cavity quality factor Q, including material losses, can be written as

$$\frac{1}{Q} = \frac{1}{Q_{sc}} + \frac{1}{Q_m} + \frac{1}{Q_w} \tag{5.3}$$

where Q_{sc} accounts for scattering losses due to mode mismatch in the tapered section and Q_m for material losses in the dielectric. Substituting Eq. 5.2 into Eq. 5.1, we have

$$U = U_{\max} = \frac{P_0}{\omega_0}Q \tag{5.4}$$

when $Q_w = \frac{Q_{sc}Q_m}{Q_{sc}+Q_m}$. Therefore, for given Q_{sc} and Q_m, it is important to tune Q_w by fixing the number of Bragg mirror pairs on each side of the resonator so as to achieve optimal critical coupling conditions by satisfying Eq. 5.4.

5.3 Fabrication and measurement

The resonator was fabricated with ultra-high purity alumina from Coorstek (AD998 PlasmaPure). This material has a relatively high refractive index of 3.1 at microwave frequencies and very small dielectric losses. Dielectric losses are important as they ultimately limit the quality factor of the resonator. The material that we use has a nominal loss factor of $tan(\delta) = 2.5 \times 10^{-5}$ at 6GHz, which results in $Q_m = 44,000$. For our device, we put 14 Bragg mirror pairs at each side, which corresponds to $Q_w = 210,000$. Therefore, the total Q factor is expected to be $36,000$. Fabrication was done with standard computer-numerical-control (CNC) milling techniques, with a nominal positional accuracy of $\sim 10\mu m$ for each hole.

The fabricated structure is shown in Fig. 5.3.1(a), and the setup used for our two-port transmittance measurements in Fig. 5.3.1(b). The device was connected

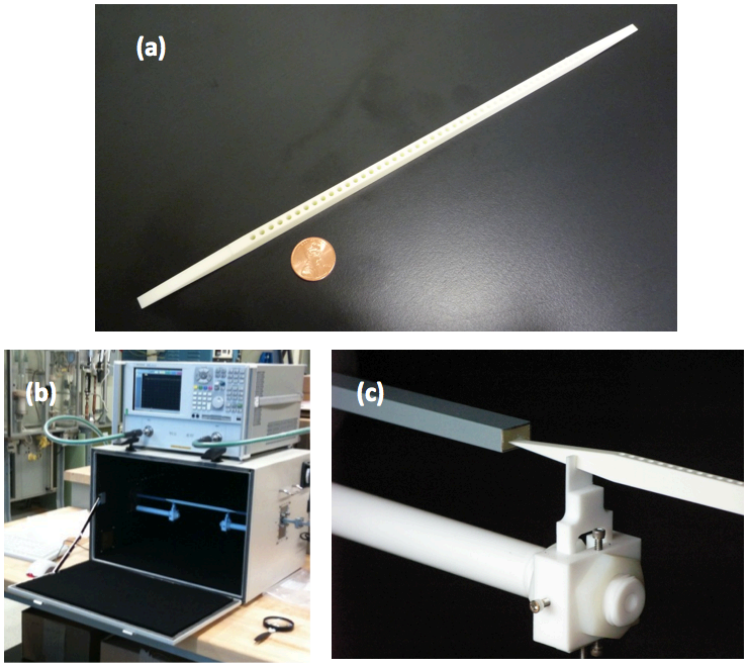

Figure 5.3.1: (a) Images of the fabricated alumina cavity with slant sections at both ends to facilitate coupling to metallic waveguides. (b) Setup for transmittance measurement. (c) Coupling components between the metallic waveguide and the dielectric rod.

to a network analyzer via conventional WR62 microwave waveguides placed at each end. Because of the geometrical mismatch between the metallic waveguide ($15.8\text{mm} \times 7.9\text{mm}$) and our dielectric waveguide resonator ($4.72\text{mm} \times 9.43\text{mm}$), we designed slant sections at both ends of the resonator to allow partial insertion into the WR62 waveguide and thereby facilitate coupling [Fig. 5.3.1(c)]. In Fig. 5.3.2(a), we show the amplitude spectrum from the transmission measurement. It demonstrates a large bandgap from 15.4GHz to 17.7GHz, which is consistent with the theory. The transmission coefficient of the cavity mode can be generally fitted using a Fano model [170, 171],

$$t = A\left[\eta \exp\left(i\phi\right) + \frac{1}{1 + i\frac{\omega - \omega_0}{\Delta\omega_{\text{FWHM}}/2}}\right] \tag{5.5}$$

where A is a constant representing system loss, η^2 denotes the ratio of power coupled to other channels (direct transmission, higher-order modes, etc.), ϕ is the phase difference, ω_o is the resonant frequency, and $\Delta\omega_{FWHM}$ is the cavity full-width half-maximum linewidth.

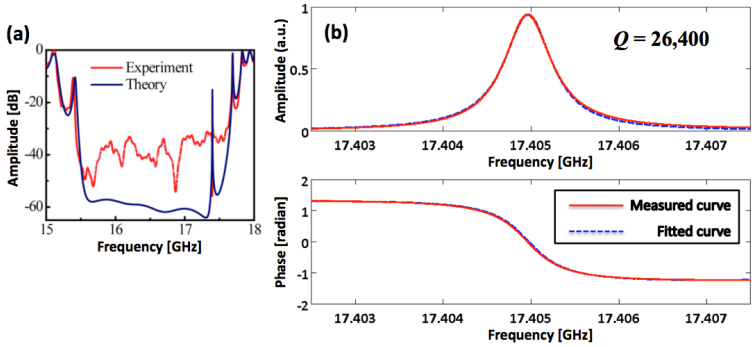

Figure 5.3.2: (a) Amplitude spectrum with a large frequency range from 15GHz to 18GHz, showing the bandgap of the structure. (b) Amplitude and phase spectra of the cavity mode from the transmittance measurement. The dashed curves are fitted with Eq. 5.5.

Unlike most photonic crystal cavity experiments at optical frequencies, here both amplitude and phase of the transmittance can be obtained. By varying the position of the resonator with respect to the waveguide ports, both η and φ can be modified, whereas ω_o and $\Delta\omega_{FWHM}$ stay constant. Here we select a set of data with minimized coupling to direct, non-resonant channels (negligible η), which results in a Lorentzian resonance lineshape. We plot the resulting spectra in Fig. 5.3.2(b), where the cavity resonance is clearly seen at 17.405GHz, in good agreement with the design value. By fitting the measured data with Eq. 5.5 we obtain a full-width half-maximum linewidth $\Delta\omega_{FWHM}$ of 0.659MHz, corresponding to a Q factor of $26,400$, which is slightly smaller than the expected Q value of $36,000$. With the resonator end-coupled to a larger WR90 waveguide, we observed Q values up to $29,500$ albeit with a less symmetrical line-shape. The observed discrepancy of Q factor can be attributed to higher dielectric losses in the bulk material at this frequency, to fabrication tolerances on the holes position and size and to resonant

losses at the transition between waveguide and dielectric. In general, a higher Q factor can be obtained with less lossy materials or at cryogenic temperatures.

Next, we insert a small antenna inside the cavity in order to study the interaction between the cavity mode and a radiating dipole. The antenna is constructed by stripping both the outer conductor and the dielectric core of a coaxial cable (Megaphase Corp., model ClearPath-A06), exposing the inner conductor for a total length of 9mm. The relatively small diameter (0.305mm) of the inner conductor was chosen to minimize any perturbation of the cavity mode.

In Fig. 5.3.3(a), we plot the reflectance spectrum measured with a network analyzer connected to the above mentioned center-fed antenna, when this is placed in free space (red) and in the center hole of cavity (blue). A clearly visible reflectance dip with a 2.2dB depth at $\sim$ 17.43GHz is observed, which we interpret as a convincing signature of the Purcell effect of the cavity. When the antenna is coupled to the cavity mode, the radiation rate is enhanced, and thus the load impedance is modified. This results in a variation of the reflectance at the analyzer port, due to the impedance mismatch between the antenna load and the cable. From Fig. 5.3.3(a), we also note that there is a change in the resonant frequency of the system, from 17.40GHz to 17.43GHz. This is due to the small but non-negligible perturbation of the metallic antenna, which blue-shifts the resonance. The free-space background in Fig. 5.3.3(a) (red-solid curve) arises from the small reflectance between the network analyzer/cable connection, and the cable/antenna connection. This background prevents us from accurately quantifying the load impedance variation and subsequently extracting a numerical value for the Purcell enhancement factor.

Next, we scanned the antenna in z-direction along the length of the dielectric rod to probe the electric field distribution of the cavity mode. This is analogous to near-field scanning optical microscopy (NSOM) [172, 173]. In Fig. 5.3.3(b), we plot the measured reflectance depth as a function of the z-position (blue-solid). In comparison, we also plot the electric field amplitude (black-dash). It can be seen that the two curves follow the same z-dependence, which verifies that the S_{11} dip

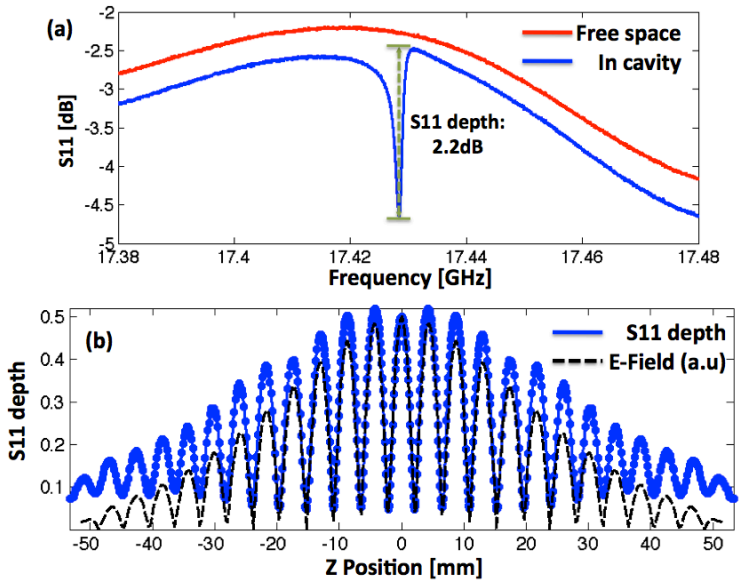

Figure 5.3.3: (a) Reflectance measurement of the center-fed antenna, with and without the cavity. (b) Reflectance depth as a function of the z-position. Also shown (dashed line), the simulated electric-field amplitude along the resonator.

we observe is due to coupling to the cavity mode.

5.4 Summary

A high-Q microwave resonator with a mode volume smaller than one cubic wavelength has been designed and fabricated. A record high Quality factor ($Q = 26,400$) for photonic crystal cavities at microwave frequencies has been measured at room temperature. In addition to its ultra-high Q/V factor, the cavity is uniquely designed to have its electric field concentrated in air. Coupling to this cavity mode is enhanced by the Purcell factor. We believe that this device is well suited for conducting microwave cavity QED experiments and for developing a variety of novel microwave devices.

6

Dual-polarized photonic crystal cavities for nonlinear applications

6.1 Introduction

Ultra-high Quality factor (Q) photonic crystal nanocavities, which are capable of storing photons within a cubic-wavelength-scale volume (V), enable enhanced light-matter interactions, and therefore provide an attractive platform for cavity quantum electrodynamics [157, 174] and nonlinear optics [175–181]. In most cases, high Q/V nanocavities are achieved with planar photonic crystal platform based on thin semiconductor slabs perforated with a lattice of holes. These struc-

tures favor transverse-electric-like (TE-like) polarized modes (the electric field in the central mirror plane of the photonic crystal slab is perpendicular to the air holes). In contrast, the transverse-magnetic-like (TM-like) polarized bandgap is favored in a lattice of high-aspect-ratio rods [169, 182]. TM-like cavities have been designed in an air-hole geometry, as well [183–185], but the Q factors of these cavities were limited to the order of 10^3. In addition, the lack of vertical confinement of these cavities results in large mode volumes [183]. Though it is possible to employ surface plasmons to localize the light tightly in the vertical direction, the lossy nature of metal limits the Q to about 10^2 [185].

In this chapter, we report a one-dimensional (1D) photonic crystal nanobeam cavity design that supports an ultra-high-Q ($Q > 10^6$) TM-like cavity mode with $V \sim (\lambda/n)^3$. This cavity greatly broadens the applications of optical nanocavities. For example, it is well-suited for photonic crystal quantum cascade lasers, since the inter-subband transition in quantum cascade lasers is TM-polarized [186–188]. We also demonstrate that our cavity simultaneously supports two ultra-high-Q modes with orthogonal polarizations (one TE-like and one TM-like). The frequency difference of the two modes can be widely tuned while maintaining the high Q factor of each mode, which is of interest for applications in nonlinear optics.

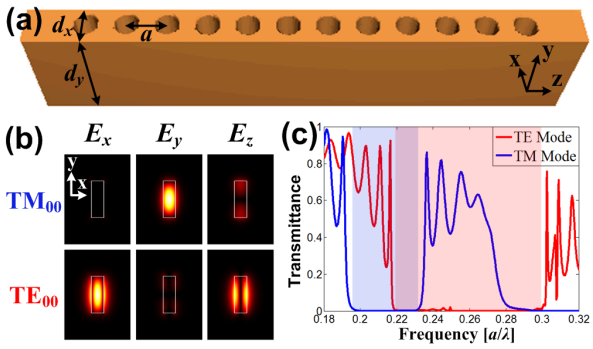

Figure 6.1.1: (a) Schematic of the nanobeam design, showing the nanobeam thickness (d_y) and width (d_x), and the hole spacing (a). (b) TE_{oo} and TM_{oo} transverse mode profiles for a ridge waveguide with $d_y = 3d_x$. (c) Transmission spectra for the TE_{oo} (red) and TM_{oo} (blue) Bloch modes. The shaded areas indicate the bandgaps for both modes.

6.2 Design

Our design is based on a dielectric suspended ridge waveguide with an array of uniform holes of periodicity, a, and radius, R, which form a 1D photonic crystal Bragg mirror [132], as shown in Fig. 6.1.1(a). The refractive index of the dielectric is set to $n = 3.4$ (similar to Si and GaAs at $\sim 1.5\mu m$). We first start with a ridge of height:width:period ratio of 3:1:1 ($d_x = a$, $d_y = 3a$) and $R = 0.3a$. Fig. 6.1.1(b) shows the transverse profiles of the fundamental TM-like and TE-like modes (TM_{oo} and TE_{oo}) supported by the ridge waveguide. The TM_{oo} mode has its major component (E_y) lined along the hole axis, whereas the TE_{oo} mode's major component (E_x) is perpendicular to the air holes. Using the three-dimensional (3D) finite-difference time-domain (FDTD) method, the transmittance spectra are obtained of the TM_{oo} and TE_{oo} modes launched towards the Bragg mirror. Fig. 6.1.1(c) shows the TM_{oo} and TE_{oo} bandgaps, respectively. In contrast to two-dimensional (2D) photonic crystal slabs, where the photon is localized in the xz plane via Bragg scattering, here we only require Bragg confinement in the longitudinal (z) direction, as light is transversely confined in the other two dimensions by total internal reflection. It has also been shown experimentally that 1D photonic

crystal nanobeam cavities have comparable Q/V ratios to 2D systems [96, 97].

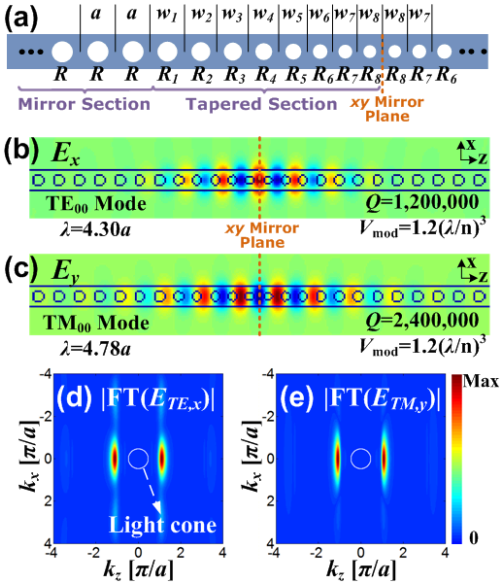

Figure 6.2.1: (a) Schematic of the 1D photonic crystal nanobeam cavity, with the tuning parameters R_k and w_k in the 8-segment tapered design. (b,c) Mode profiles of the electric field components $E_{\mathrm{TE},x}$ and $E_{\mathrm{TM},y}$ for the cavity design with $d_x = a$, $d_y = 3a$. (d,e) Spatial Fourier transform of the electric field component profiles ($E_{\mathrm{TE},x}$ and $E_{\mathrm{TM},y}$) in the xz plane ($y = 0$).

Introducing a lattice grading to the periodic structure creates a localized potential for both TE- and TM-like modes. To optimize the mode Q factors, we apply the bandgap-tapering technique that is well-developed in previous work [65, 90, 91, 189, 190]. We use an 8-segment tapered section with holes (R_1-R_8) and a 12-period mirror section at each side. Two degrees of freedom are available for each tapered segment: the length (w_k) and the radius (R_k). We keep the ratio R_k/w_k fixed at each segment, and then implement a linear interpolation of the grating constant ($2\pi/w_k$). When the central segment w_8 is set to $0.84a$, we obtain ultra-high Qs and low mode volumes for both TE- and TM-polarized modes ($Q_{\mathrm{TE}} = 1.2 \times 10^6$, $Q_{\mathrm{TM}} = 2.4 \times 10^6$, $V_{\mathrm{TE}} = V_{\mathrm{TM}} = 1.2(\lambda/n)^3$), with free-space wavelengths $4.30a$ and $4.78a$, respectively. Fig. 6.2.1(b) and (c) show the mode profiles of the major components of the two modes in the xz mirror plane.

The ultra-high Q factors can also be interpreted in momentum space [70, 71, 183]. Fig. 6.2.1(d) and (e) demonstrate the Fourier transformed (FT) profiles of the electric field components $E_{TE,x}$ and $E_{TM,y}$ in the xz plane ($y = 0$), with the light cone indicated by the white circle. It can be seen that both modes' Fourier components are localized tightly at the bandedge of the Brillouin zone on the k_z-axis ($k_z = \pi/a$). This reduces the amount of mode energy within the light cone that is responsible for scattering losses. It is also worthwhile to note that higher-longitudinal-order TE_{00} and TM_{00} cavity modes with different symmetry with respect to the xy mirror plane exist [189]. For example, the second-order TE_{00} mode, which has a node at the xy mirror plane, resonates at a wavelength of $4.43a$. It has a higher Q factor of 4.7×10^6, but a larger mode volume of $2.1(\lambda/n)^3$.

For a number of applications of interest, control of the frequency spacing between the two modes is required. Examples include polarization-entangled photon generation for degenerate modes [191], and terahertz generation for $0.1 - 10$THz mode splitting [179]. We tune the frequency separation of the two modes by varying the thickness of the structure while keeping the other parameters constant. In Fig. 6.2.2(a), the cavity resonances of the TE_{00} and TM_{00} modes are traced as a function of the nanobeam thickness (d_y/a). The TM-like modes have a much larger dependence on the thickness than the TE-like modes. The modes are degenerate at $d_y = 1.26a$, and for thicknesses beyond this value, ω_{TE} is larger than ω_{TM}. As d_y increases, the splitting increases until it saturates when the system approaches the 2D limit (structure is infinite in the y-direction). In this limit, we find that $\lambda_{TE} = 4.4a$ and $\lambda_{TM} = 5.1a$. The frequency separation ($\delta\omega = |\omega_{TE} - \omega_{TM}|$) of this design ranges from 0THz to 20THz, with the TE-like mode wavelength fixed at $1.5\mu m$ by scaling the structure accordingly. Fig. 6.2.2(b) shows the thickness dependence of the Q factor for the xz design specifications listed above. It can be seen that the Q factors of both TE- and TM-polarized modes stay above 10^5 for the $\omega_{TE} > \omega_{TM}$ branch.

Decreasing d_y causes the width of the TM bandgap to sharply decrease, whereas the width of the TE bandgap remains almost constant. The narrowed TM bandgap

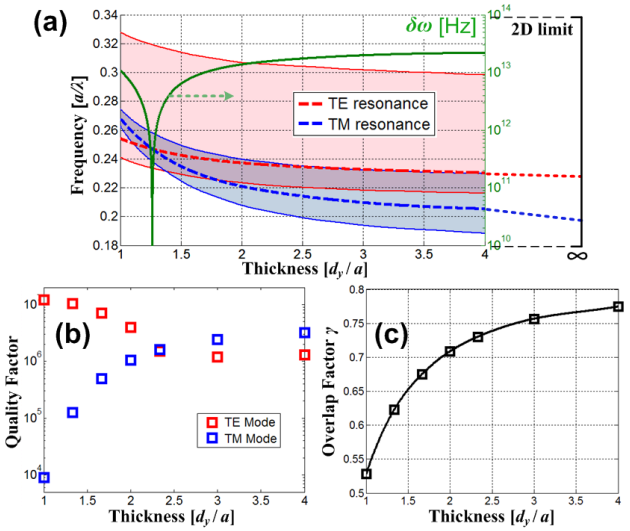

Figure 6.2.2: (a) TE_{oo} (red) and TM_{oo} (blue) cavity mode resonant frequencies (dotted lines) as a function of the nanobeam thickness. The bandgap regions of the two modes are shaded. The frequency separation ($\delta\omega$) of the two modes with the TE-like mode wavelength fixed at $1.5\mu m$ by scaling the structure accordingly is plotted in green. (b,c) Dependence of the Q factor and nonlinear overlap factor γ on the nanobeam thickness.

results in a reduced Bragg confinement, which increases the transmission losses through the Bragg mirrors. This is evidenced by the Q factor of the TM mode, which drops to $9,000$ when the thickness:width ratio is $1:1$. Though this leakage can be compensated for, in principle, by increasing the number of periods of the mirror sections, the length of the structure also increases, which makes fabrication more challenging for a suspended nanobeam geometry. A narrow bandgap also leads to large penetration depth of the mode into the Bragg mirrors, thereby increasing the mode volume.

6.3 Application for nonlinear optics

Next, we examine the application of our dual-polarized cavity for the resonance enhancement of nonlinear processes. To achieve a large nonlinear interaction in materials with dominant off-diagonal nonlinear susceptibility terms (e.g. $\chi^{(2)}_{ijk}, i \neq j \neq k$), such as III-V semiconductors [180, 181, 192], it is beneficial to mix two modes with orthogonal polarizations. As shown in our previous work [179], the strength of the nonlinear interaction can be characterized by the modal overlap, which can be quantified using the following figure of merit,

$$\gamma \equiv \varepsilon_{r,d} \frac{\int_d d^3\mathbf{r} \sum_{i,j,i\neq j} E_{\mathrm{TE},i} E_{\mathrm{TM},j}}{\sqrt{\int d^3\mathbf{r} \varepsilon_r |\mathbf{E}_{\mathrm{TE}}|^2} \sqrt{\int d^3\mathbf{r} \varepsilon_r |\mathbf{E}_{\mathrm{TM}}|^2}}. \tag{6.1}$$

where $\int_d$ denotes integration over only the regions of nonlinear dielectric, and $\varepsilon_{r,d}$ denotes the maximum dielectric constant of the nonlinear material. Note that we have normalized γ so that $\gamma = 1$ corresponds to the theoretical maximum overlap. For the TE_{00} and TM_{00} modes we studied, the two major components ($E_{\mathrm{TE},x}$ and $E_{\mathrm{TM},y}$) share the same parity (have anti-nodes in all the three mirror planes), and only two overlap components, $E_{\mathrm{TE},x}E_{\mathrm{TM},y}$ and $E_{\mathrm{TE},y}E_{\mathrm{TM},x}$, in Eq. 6.1 do not vanish. This allows a large nonlinear spatial overlap. We obtain $\gamma = 0.76$ for the cavity shown in Fig. 6.2.1. The overlap approaches $\gamma = 0.78$ in the limit $d_y \to \infty$. We find that the overlap factor, γ, stays at a reasonably high value

(> 0.6) across the full range of the frequency difference tuning (for $\omega_{TE} > \omega_{TM}$ branch) [Fig. 6.2.1(c)].

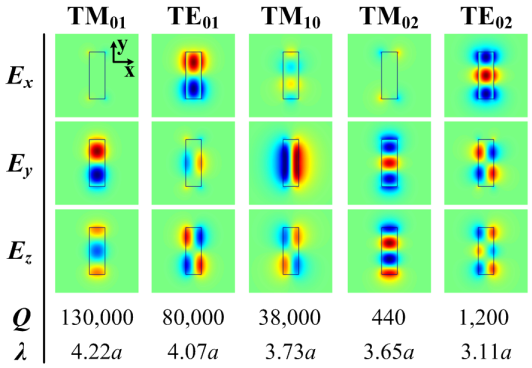

Figure 6.3.1: Parameters of the higher-order cavity modes for the design with $d_x = a$, $d_y = 3a$.

Finally, it is important to note that thick nanobeams can support higher-order modes with a different number of nodes in the *xy* plane, as well. These higher-order modes are also confined in the tapered section within their respective bandgaps, with the Q factors and wavelengths listed in Fig. 6.3.1 for the $d_x = a$ and $d_y = 3a$ case. These modes can offer a broader spectral range than the fundamental modes, which is of great interest to nonlinear applications requiring a large bandwidth [181].

6.4 Summary

In conclusion, we have demonstrated that ultra-high-Q TE- and TM-like fundamental modes with mode-volumes $\sim (\lambda/n)^3$ can be designed in 1D photonic crystal nanobeam cavities. We have shown that the frequency splitting of these two modes can be tuned over a wide range without compromising the Q factors. We have also shown that these modes can have a high nonlinear overlap in materials with large off-diagonal nonlinear susceptibility terms across the entire tuning range of the frequency spacing. We expect these cavities to have broad applications in the enhancement of nonlinear processes.

References

[1] R. Ludwig, P. Bretchko, "RF Circuit design theory and applications", (Prentice Hall Inc., Englewood Cliffs, NJ Vol. 175, 2002).

[2] D. C. Harris, "Materials for infrared windows and domes: properties and performance", (SPIE: Bellingham, WA, 1999).

[3] M. Born, E. Wolf, "Principles of Optics" (Cambridge University Press, Cambridge, England, 1999).

[4] G. A. Niklasson, C. G. Granqvist, O. Hunderi, "Effective medium models for the optical properties of inhomogeneous materials," Appl. Opt. **20**, 26 (1981).

[5] I. R. Hooper, P. Vukusic, R. J. Wootton, "Detailed optical study of the transparent wing membranes of the dragonfly Aeshna cyanea," Opt. Express **14**, 4891 (2006).

[6] P. B. Clapham, M. C. Hutley, "Reduction of lens reflexion by the 'moth eye' principle," Nature **244**, 281 (1973).

[7] S. J. Wilson, M. C. Hutley, "The optical properties of 'moth eye' antireflection surfaces," Opt. Acta **29**, 993 (1982).

[8] M. Srinivasarao, "Nano-optics in the biological world: Beetles, butterflies, birds, and moths," Chem. Rev. **99**, 1935 (1999).

[9] T. Søndergaard, S.M. Novikov, T. Holmgaard, R. L. Eriksen, J. Beermann, Z. Han, K. Pedersen, S.I. Bozhevolnyi, "Plasmonic black gold by adiabatic nanofocusing and absorption of light in ultra-sharp convex grooves," Nat. Comm. **3**, 969 (2012).

[10] Y. F. Huang, S. Chattopadhyay, Y. J. Jen, C. Y. Peng, T. A. Liu, Y. K. Hsu, C. L. Pan, H. C. Lo, C. H. Hsu, Y. H. Chang, C. S. Lee, K. H. Chen, L. C. Chen, "Biomimetic broadband antireflection gratings on solar-grade multicrystalline silicon wafers," Nat. Nanotechnol. **2**, 770 (2007).

[11] H.L. Chen, S.Y. Chuang, C.H. Lin, Y.H. Lin, "Using colloidal lithography to fabricate and optimize sub-wavelength pyramidal and honeycomb structures in solar cells," Opt. Express **15**, 14793 (2007).

[12] K. C. Park, H. J. Choi, C. H. Chang, R. E. Cohen, G. H. McKinley, G. Barbastathis, "Nanotextured silica surfaces with robust superhydrophobicity and omnidirectional broadband supertransmissivity," ACS Nano **6**, 3789 (2012).

[13] G. Xie, G. Zhang, F. Lin, J. Zhang, Z. Liu, S. Mu, "The fabrication of subwavelength anti-reflective nanostructures using a bio-template," Nanotechnology **19**, 095605 (2008).

[14] B. Sheldon, J. S. Haggerty, A.G. Emslie, "Exact computation of the reflectance of a surface layer of arbitrary refractive-index profile and an approximate solution of the inverse problem," J. Opt. Soc. Am. **72**, 1049 (1982).

[15] W. H. Southwell, "Gradient-index antireflection coatings," Opt. Lett. **8**, 584–586 (1983).

[16] E. B. Grann, M. G. Moharam, D. A. Pommet, "Optimal design for antireflective tapered two-dimensional subwavelength grating structures," J. Opt. Soc. Am. A **12**, 333 (1995).

[17] S. Chattopadhyay, Y. F. Huang, Y. J. Jen, A. Ganguly, K. H. Chen, L. C. Chen, "Anti-reflecting and photonic nanostructures," Mater. Sci. Eng. Rep. **69**, 1 (2010).

[18] K. X. Wang, Z. Yu, V. Liu, Y. Cui, S. Fan, "Absorption Enhancement in Ultra-Thin Crystalline Silicon Solar Cells with Anti-Reflection and Light-Trapping Nanocone Gratings," Nano Lett. **12**, 1616 (2012).

[19] P. S. R. Diniz, E. A. B. D. Silva, S. L. Netto, "Digital Signal Processing: System Analysis and Design", (Cambridge University Press, New York, 2002).

[20] C. L. Dolph, "A current distribution for broadside arrays which optimizes the relationship between beam width and side-lobe level", Proc. IRE **34**, 335 (1946).

[21] Hann window function follows a cosine curve, $p(u) \sim 1 - \cos(2\pi u)$.

[22] R. W. Klopfenstein, "A transmission line taper of improved design," Proc. IRE **44**, 31 (1956).

[23] S. Kinoshita, S. Yoshioka, Y. Fujii, N. Okamoto, "Photophysics of Structural Color in the Morpho Butterflies," Forma **17**, 103-121 (2002).

[24] E. Ozbay, "Plasmonics: Merging Photonics and Electronics at Nanoscale Dimensions," Science **311**, 189 (2006).

[25] D. R. Smith, J. B. Pendry, M. C. K. Wiltshire, "Metamaterials and Negative Refractive Index," Science **305**, 788 (2004).

[26] G. A. Steinmeyer, "review of ultrafast optics and optoelectronics," J. Opt. A: Pure Appl. Opt. **5**, R1-R5 (2003).

[27] Y. Zhang, C. Li, M. Loncar, "Optimal Broadband Antireflective Taper," Opt. Lett. **38**, 646 (2013).

[28] A. M. Weiner, "Femtosecond pulse shaping using spatial light modulators," Rev. Sci. Inst. **71**, 1929 (2000).

[29] A. Prakelt, M. Wollenhaupt, A. Assion, Ch. Horn, C. Sarpe-Tudoran, "Compact, robust, and flexible setup for femtosecond pulse shaping," Rev. Sci. Instrum **74**, 4950 (2003).

[30] A. Monmayrant, S. Weber, B. Chatel, "A newcomer's guide to ultrashort pulse shaping and characterization," J. Phys. B: At. Mol. Opt. Phys. **43**, 103001 (2010).

[31] M. H. Huang, S. Mao, H. Feick, H. Yan, Y. Wu, H. Kind, E. Weber, R. Russo, and P. Yang, "Room-temperature ultraviolet nanowire nanolasers," Science **292**, 1897-1899 (2001).

[32] X. Duan, Y. Huang, R. Agarwal, and C. M. Lieber, "Single-nanowire electrically driven laser," Nature **421**, 241-245 (2003).

[33] R. Agarwal, C. J. Barrelet, and C. M. Lieber, "Lasing in single cadmium sulfide nanowire optical cavities," Nano. Lett. **5**, 917-920 (2005).

[34] S. Gradecek, F. Qian, Y. Li, H. G. Park, and C. M. Lieber, "GaN nanowire lasers with low lasing threshold," Appl. Phys. Lett. **87**, 173111 (2005).

[35] J. M. Bao, M. Zimmler, F. Capasso, X. Wang, and Z. F. Ren, "Broadband ZnO single-nanowire light-emitting diode," Nano. Lett. **6**, 1719-1722 (2006).

[36] J. C. Johnson, H. Yan, P. Yang, and R. J. Saykally, "Optical cavity effects in ZnO nanowire lasers and waveguides," J. Phys. Chem. B **107**, 8816-8828 (2003).

[37] A. Maslov and C. Ning, "Reflection of guided modes in a semiconductor nanowire laser," Appl. Phys. Lett. **83**, 1237-1239 (2003).

[38] Z. Y. Li and K. M. Ho, "Bloch mode reflection and lasing threshold in semiconductor nanowire laser arrays," Physical Review B **71**, 045315 (2005).

[39] M. Q. Wang, Y. Z. Huang, Q. Chen, and Z. P. Cai, "Analysis of mode quality factors and mode reflectivities for nanowire cavity by FDTD technique," IEEE J. Quantum Electron. 42, 146-151 (2006).

[40] Y. Ding, J. Motohisa, B. Hua, S. Hara, and T. Fukui, "Observation of microcavity modes and waveguides in InP nanowires fabricated by selective-area metalorganic vapor-phase epitaxy," Nano. Lett. 7, 3598-3602 (2007).

[41] A. Maslov and C. Ning, "Modal gain in a semiconductor nanowire laser with anisotropic bandstructure," IEEE J. Quantum Electron. **40**, 1389-1397 (2004).

[42] C. Barrelet, J. Bao, M. Loncar, H. G. Park, F. Capasso, and C. M. Lieber, "Hybrid single-nanowire photonic crystal and microresonator structures," Nano. Lett. **6**, 11-15 (2006).

[43] O. L. Muskens, J. Treffers, M. Forcales, M. T. Borgstrom, E. P. A. M. Bakkers, and J. G. Rivas, "Modification of the photoluminescence anisotropy of semiconductor nanowires by coupling to surface plasmon polaritons," Opt. Lett. **32**, 2097-2099 (2007).

[44] H. G. Park, F. Qian, C. J. Barrelet, and Y. Li, "Microstadium single-nanowire laser," Appl. Phys. Lett. **91**, 251115 (2007).

[45] M. Pelton, C. Santori, J. Vuckovic, B. Zhang, G. S. Solomon, J. Plant, and Y. Yamamoto, "Efficient source of single photons: A single quantum dot in a micropost microcavity," Phys. Rev. Lett. **89**, 233602 (2002).

[46] P. Michler, A. Kiraz, C. Becher, W. V. Schoenfeld, P. M. Petroff, L. Zhang, E. Hu, and A. Imamoglu, "A quantum dot single-photon turnstile device," Science **290**, 2282-2285 (2000).

[47] D. Englund, D. Fattal, E. Waks, G. Solomon, B. Zhang, T. Nakaoka, Y. Arakawa, Y. Yamamoto, and J. Vuckovic, "Controlling the spontaneous

emission rate of single quantum dots in a two-dimensional photonic crystals," Phys. Rev. Lett. **95**, 013904 (2005).

[48] M. S. Gudiksen, L. J. Lauhon, J. Wang, D. C. Smith, and C. M. Lieber, "Growth of nanowire superlattice structures for nanoscale photonics and electronics," Nature **415**, 617-620 (2002).

[49] M. T. Bjork, B. J. Ohlsson, T. Sass, A. I. Persson, C. Thelander, M. H. Magnusson, K. Deppert, L. R. Wallenberg, and L. Samuelson, "One-dimensional heterostructures in semiconductor nanowhiskers," Appl. Phys. Lett. **80**, 1058-1060 (2002).

[50] N. Panev, A. I. Persson, N. Skold, and L. Samuelson, "Sharp exciton emission from single InAs quantum dots in GaAs nanowires," Appl. Phys. Lett. **83**, 2238-2240 (2003).

[51] L. Samuelson, M. T. Bjork, K. Deppert, M. Larsson, B. J. Ohlsson, N. Panev, A. I. Persson, N. Skold, C. Thelander, and L. R. Wallenberg, "Semiconductor nanowires for novel one-dimensional devices," Physica E **21**, 560-567 (2004).

[52] M. T. Bjork, C. Thelander, A. E. Hansen, L. E. Jenson, M. W. Larsson, L. R. Wallenberg, and L. Samuelson, "Few-electron quantum dots in nanowires," Nano. Lett. **4**, 1621-1625 (2004).

[53] C. P. T. Svensson, W. Seifert, M. W. Larsson, L. R. Wallenberg, J. Stangl, G. Bauer, and L. Samuelson, "Epitaxially grown GaP/ GaAs1-xPx/GaP double heterostructure nanowires for optical applications," Nanotechnology **16**, 936-939 (2005).

[54] M. T. Borgstrom, V. Zwiller, E. Muller, and A. Imamoglu, "Optically bright quantum dots in single nanowires," Nano. Lett. **5**, 1439-1443 (2005).

[55] E. D. Minot, F. Kelkensberg, M. v. Kouwen, J. A. v. Dam, L. P. Kouwenhoven, V. Zwiller, M. T. Borgstrom, O. Wunnicke, M. A. Verheijen, and E.

P. A. M. Bakkers, "Single quantum dot nanowire LEDs," Nano. Lett. **7**, 367-371 (2007).

[56] P. Lalanne and J. P. Hugonin, "Bloch-wave engineering for high-Q, small-V microcavities," IEEE J. Quantum Electron. **39**, 1430-1438 (2003).

[57] H. J. Kimble, in Cavity Electrodynamics, P. Berman, ed. (Academic Press, San Diego, 1994).

[58] A. Yariv, Photonics: Optical electronics in modern communications, 6 ed. (Oxford University Press, 2006).

[59] L. Tong, J. Lou, and E. Mazur, "Single-mode guiding properties of subwavelength-diameter silica and silicon wire waveguides," Opt. Express **12**, 1025-1035 (2004).

[60] M. Palamaru and P. Lalanne, "Photonic crystal waveguides: Out-of-plane losses and adiabatic modal conversion," Appl. Phys. Lett. **78**, 1466-1468 (2001).

[61] C. Sauvan, G. Lecamp, P. Lalanne, and J. P. Hugonin, "Modal-reflectivity enhancement by geometry tuning in Photonic Crystal microcavities," Opt. Express **13**, 245-255 (2005).

[62] P. Velha, E. Picard, T. Charvolin, E. Hadji, J. C. Rodier, P. Lalanne, and D. Peyrade, "Ultra-high Q/V Fabry-Perot microcavity on SOI substrate," Opt. Express **15**, 16090-16096 (2007).

[63] A. I. Persson, M. T. Bjork, S. Jeppesen, J. B. Wagner, L. R. Wallenberg, and L. Samuelson, "InAs1-xPx nanowires for device engineering," Nano. Lett. **6**, 403-407 (2006).

[64] S. K. Lim, M. J. Tambe, M. M. Brewster, and S. Gradecak, "Controlled growth of ternary alloy nanowires using metalorganic chemical vapor deposition," Nano. Lett. **8**, 1386-1392 (2008).

[65] M. Notomi, E. Kuramochi, and H. Taniyama, "Ultrahigh-Q nanocavity with 1D photonic gap," Opt. Express **16**, 11095-11102 (2008).

[66] T. Asano, B. S. Song, Y. Akahane, and S. Noda, "Ultrahigh-Q nanocavities in two-dimensional photonic crystal slabs," IEEE J. Sel. Top. Quantum Electron. **12**, 1123-1134 (2006).

[67] B. S. Song, S. Noda, T. Asano, and Y. Akahane, "Ultra-high-Q photonic double-heterostructure nanocavity," Nat. Mater. **4**, 207-210 (2005).

[68] Y. Tanaka, T. Asano, and S. Noda, "Design of photonic crystal nanocavity with Q-factor of similar to 10(9)," J. Lightwave Technol. **26**, 1532-1539 (2008).

[69] D. Englund, I. Fushman, and J. Vuckovic, "General recipe for designing photonic crystal cavities," Opt. Express **13**, 5961-5975 (2005).

[70] J. Vuckovic, M. Loncar, H. Mabuchi, and A. Scherer, "Optimization of the Q factor in photonic crystal microcavities," IEEE J. Quantum Electron. **38**, 850-856 (2002).

[71] K. Srinivasan and O. Painter, "Momentum space design of high-Q photonic crystal optical cavities," Opt. Express **10**, 670-684 (2002).

[72] J. L. Jewell, J. P. Harbison, A. Scherer, Y. H. Lee, and L. T. Florez, "Vertical-cavity surface-emitting lasers - design, growth, fabrication, characterization," IEEE J. Quantum Electron. **27**, 1332-1346 (1991).

[73] J. P. Reithmaier, G. Sek, A. Loffler, C. Hofmann, S. Kuhn, S. Reitzenstein, L. V. Keldysh, V. D. Kulakovskii, T. L. Reinecke, and A. Forchel, "Strong coupling in a single quantum dot-semiconductor microcavity system," Nature **432**, 197-200 (2004).

[74] S. Reitzenstein, C. Hofmann, A. Gorbunov, M. Strauss, S. H. Kwon, C. Schneider, A. Loffler, S. Hofling, M. Kamp, and A. Forchel, "AlAs/GaAs mi-

cropillar cavities with quality factors exceeding 150,000," Appl. Phys. Lett. **90**, 251109 (2007).

[75] J. M. Gerard, B. Sermage, B. Gayral, B. Legrand, E. Costard, and V. Thierry-Mieg, "Enhanced spontaneous emission by quantum boxes in a monolithic optical microcavity," Phys. Rev. Lett. **81**, 1110-1113 (1998).

[76] J. Vuckovic, M. Pelton, A. Scherer, and Y. Yamamoto, "Optimization of three-dimensional micropost microcavities for cavity quantum electrodynamics," Phys. Rev. A **66**, 023808 (2002).

[77] L. Chen and E. Towe, "Photonic band gaps in nanowire superlattices," Appl. Phys. Lett. **87**, 10311 (2005).

[78] O. Beyer, I. Nee, F. Havermeyer, and K. Buse, "Holographic recording of Bragg gratings for wavelength division multiplexing in doped and partially polymerized poly(methyl methacrylate)," Appl. Opt. **42**, 30-37 (2003).

[79] E. M. Purcell, "Spontaneous emission probabilities at radio frequencies " Phys. Rev. **69**, 681-681 (1946).

[80] T. Baba, "Photonic crystals and microdisk cavities based on GaInAsP-InP system," IEEE J. Quantum Electron. **3**, 808-830 (1997).

[81] G. Khitrova, H. M. Gibbs, M. Kira, S. W. Koch, and A. Scherer, "Vacuum Rabi splitting in semiconductors," Nature Phys. **2**, 81-90 (2006).

[82] K. Iga, "Vertical-cavity surface-emitting laser: Its conception and evolution," Jpn. J. Appl. Phys. **47**, 1-10 (2008).

[83] D. L. Huffaker, Z. Zou, and D. G. Deppe, "Reduced cavity loss for ultra-low threshold vertical cavity surface emitting lasers," in 12th Annual Meeting IEEE Lasers and Electro-Optics Society, LEOS '99., 391-392, 1999.

[84] S. Reitzenstein, C. Bockler, A. Bazhenov, A. Gorbunov, A. Loffler, M. Kamp, V. D. Kulakovskii, and A. Forchel, "Single quantum dot controlled lasing effects in high-Q micropillar cavities," Opt. Express **16**, 4848-4857 (2008).

[85] J. P. Reithmaier, G. Sek, A. Loffler, C. Hofmann, S. Kuhn, S. Reitzenstein, L. V. Keldysh, V. D. Kulakovskii, T. L. Reinecke, and A. Forchel, "Strong coupling in a single quantum dot-semiconductor microcavity system," Nature **432**, 197-200 (2004).

[86] D. Press, S. Gotzinger, S. Reitzenstein, C. Hofmann, A. Loffler, M. Kamp, A. Forchel, and Y. Yamamoto, "Photon antibunching from a single quantum-dot-microcavity system in the strong coupling regime," Phys. Rev. Lett. **98**, 117402 (2007).

[87] S. Reitzenstein, C. Hofmann, A. Gorbunov, M. Gorbunov, M. Straub, S. H. Kwon, C. Schneider, A. Loffler, S. Hofling, M. Kamp, and A. Forchel, "AlAs/GaAs micropillar cavities with quality factors exceeding 150.000," Appl. Phys. Lett. **90**, 251109 (2007).

[88] P. Lalanne, J. P. Hugonin, and J. M. Gerard, "Electromagnetic study of the quality factor of pillar microcavities in the small diameter limit," Appl. Phys. Lett. **84**, 4726-4728 (2004).

[89] G. Lecamp, J. P. Hugonin, P. Lalanne, R. Braive, S. Varoutsis, S. Laurent, A. Lemaitre, I. Sagnes, G. Patriarche, I. Robert-Philip, and I. Abram, "Submicron-diameter semiconductor pillar microcavities with very high quality factors," Appl. Phys. Lett. **90**, 091120 (2007).

[90] Y. Zhang and M. Loncar, "Ultra-high quality factor optical resonators based on semiconductor nanowires," Opt. Express **16**, 17400-17409 (2008).

[91] M. W. McCutcheon and M. Loncar, "Design of a silicon nitride photonic crystal nanocavity with a Quality factor of one million for coupling to a diamond nanocrystal," Opt. Express **16**, 19136-19145 (2008).

[92] L. Childress, M. V. G. Dutt, J. M. Taylor, A. S. Zibrov, F. Jelezko, J. Wrachtrup, P. R. Hemmer, and M. D. Lukin, "Coherent dynamics of coupled electron and nuclear spin qubits in diamond," Science **314**, 281-285 (2006).

[93] N. G. Stoltz, M. Rakher, S. Strauf, A. Badolato, D. D. Lofgreen, P. M. Petroff, L. A. Coldren, and D. Bouwmeester, "High-quality factor optical microcavities using oxide apertured micropillars," Appl. Phys. Lett. **87**, 031105 (2005).

[94] E. Yablonovitch, "Inhibited spontaneous emission in solid-state physics and electronics," Phys. Rev. Lett. **58**, 2059-2062 (1987).

[95] S. John, "Strong localization of photons in certain disordered dielectric superlattices," Phys. Rev. Lett. **58**, 2486-2489 (1987).

[96] A. Zain, N. P. Johnson, M. Sorel, and R. M. De la Rue, "Ultra high quality factor one dimensional photonic crystal/photonic wire micro-cavities in silicon-on-insulator (SOI)," Opt. Express **16**, 12084-12089 (2008).

[97] P. B. Deotare, M. W. McCutcheon, I. W. Frank, M. Khan, and M. Loncar, "High quality factor photonic crystal nanobeam cavities," Appl. Phys. Lett. **94**, 121106 (2009)

[98] O. Painter, J. Vuckovic, and A. Scherer, "Defect modes of a two-dimensional photonic crystal in an optically thin dielectric slab," J. Opt. Soc. Am. B **16**, 275-285 (1999).

[99] T. Yoshie, J. Vuckovic, A. Scherer, H. Chen, and D. Deppe, "High quality two-dimensional photonic crystal slab cavities," Appl. Phys. Lett. **79**, 4289-4291 (2001).

[100] Y. Akahane, T. Asano, B. S. Song, and S. Noda, "High-Q photonic nanocavity in a two-dimensional photonic crystal," Nature **425**, 944-947 (2003).

[101] K. Srinivasan, P. E. Barclay, O. Painter, J. X. Chen, A. Y. Cho, and C. Gmachl, "Experimental demonstration of a high quality factor photonic crystal microcavity," Appl. Phys. Lett. **83**, 1915-1917 (2003).

[102] E. Kuramochi, M. Notomi, S. Mitsugi, A. Shinya, T. Tanabe, and T. Watanabe, "Ultrahigh-Q photonic crystal nanocavities realized by the local width modulation of a line defect," Appl. Phys. Lett. **88**, 041112 (2006).

[103] M. Notomi, E. Kuramochi, and T. Tanabe, "Large-scale arrays of ultrahigh-Q coupled nanocavities," Nat. Photonics **2**, 741-747 (2008).

[104] K. Aoki, D. Guimard, M. Nishioka, M. Nomura, S. Iwamoto, and Y. Arakawa, "Coupling of quantum-dot light emission with a three-dimensional photonic-crystal nanocavity," Nat. Photonics **2**, 688-692 (2008).

[105] K. Iga, F. Koyama, and S. Kinoshita, "Surface Emitting Semiconductor-Lasers," IEEE J. Quantum Electron. **24**, 1845-1855 (1988).

[106] O. Painter, R. K. Lee, A. Scherer, A. Yariv, J. D. O'Brien, P. D. Dapkus, and I. Kim, "Two-dimensional photonic band-gap defect mode laser," Science **284**, 1819-1821 (1999).

[107] H. G. Park, S. H. Kim, S. H. Kwon, Y. G. Ju, J. K. Yang, J. H. Baek, S. B. Kim, and Y. H. Lee, "Electrically driven single-cell photonic crystal laser," Science **305**, 1444-1447 (2004).

[108] J. K. Hwang, H. Y. Ryu, D. S. Song, I. Y. Han, H. K. Park, D. H. Jang, and Y. H. Lee, "Continuous room-temperature operation of optically pumped two-dimensional photonic crystal lasers at 1.6 mu m," IEEE. Photon. Tech. Lett. **12**, 1295-1297 (2000).

[109] S. Matsuo, A. Shinya, T. Kakitsuka, K. Nozaki, T. Segawa, T. Sato, Y. Kawaguchi, and M. Notomi, "High-speed ultracompact buried heterostructure photonic-crystal laser with 13 fJ of energy consumed per bit transmitted," Nat. Photonics **4**, 648-654 (2010).

[110] Y. Halioua, T. J. Karle, F. Raineri, P. Monnier, I. Sagnes, G. Roelkens, D. Van Thourhout, and R. Raj, "Hybrid InP-based photonic crystal lasers on silicon on insulator wires," Appl. Phys. Lett. **95**, 201119 (2009).

[111] K. Nozaki, S. Kita, and T. Baba, "Room temperature continuous wave operation and controlled spontaneous emission in ultrasmall photonic crystal nanolaser," Opt. Express **15**, 7506-7514 (2007).

[112] M. Nomura, N. Kumagai, S. Iwamoto, Y. Ota, and Y. Arakawa, "Photonic crystal nanocavity laser with a single quantum dot gain," Opt. Express **17**, 15975-15982 (2009).

[113] M. Nomura, Y. Ota, N. Kumagai, S. Iwamoto, and Y. Arakawa, "Zero-cell photonic crystal nanocavity laser with quantum dot gain," Appl. Phys. Lett. **97**, 191108 (2010).

[114] B. Ellis, M. A. Mayer, G. Shambat, T. Sarmiento, J. Harris, E. E. Haller, and J. Vuckovic, "Ultralow-threshold electrically pumped quantum-dot photonic-crystal nanocavity laser," Nat. Photonics **5**, 297-300 (2011).

[115] Y. Yamamoto, S. Machida, and G. Bjork, "Microcavity Semiconductor-Laser with Enhanced Spontaneous Emission," Phys. Rev. A **44**, 657-668 (1991).

[116] H. Yokoyama, K. Nishi, T. Anan, Y. Nambu, S. D. Brorson, E. P. Ippen, and M. Suzuki, "Controlling spontaneous emission and threshold-less laser oscillation with optical microcavities," Opt. Quant. Electron. **24**, S245-S272 (1992).

[117] E. M. Purcell, "Spontaneous emission probabilities at radio frequencies," Phys. Review **69**, 681-681 (1946).

[118] H. Altug, D. Englund, and J. Vuckovic, "Ultrafast photonic crystal nanocavity laser," Nat. Physics **2**, 484-488 (2006).

[119] S. Noda, M. Yokoyama, M. Imada, A. Chutinan, and M. Mochizuki, "Polarization mode control of two-dimensional photonic crystal laser by unit cell structure design," Science **293**, 1123-1125 (2001).

[120] J. H. Kang, M. K. Seo, S. K. Kim, S. H. Kim, M. K. Kim, H. G. Park, K. S. Kim, and Y. H. Lee, "Polarized vertical beaming of an engineered hexapole mode laser," Opt. Express **17**, 6074-6081 (2009).

[121] R. Perahia, J. D. Cohen, S. Meenehan, T. P. M. Alegre, and O. Painter, "Electrostatically tunable optomechanical "zipper" cavity laser," Appl. Phys. Lett. **97**, 191112 (2010).

[122] B. Maune, M. Loncar, J. Witzens, M. Hochberg, T. Baehr-Jones, D. Psaltis, A. Scherer, and Y. M. Qiu, "Liquid-crystal electric tuning of a photonic crystal laser," Appl. Phys. Lett. **85**, 360-362 (2004).

[123] K. Petermann, "Calculated Spontaneous Emission Factor for Double-Heterostructure Injection-Lasers with Gain-Induced Waveguiding," IEEE J. Quantum Electron. **15**, 566-570 (1979).

[124] Y. G. Zhao, J. G. Mcinerney, and R. A. Morgan, "Measurement of Spontaneous Emission Factor for Vertical-Cavity Surface-Emitting Semiconductor-Lasers," IEEE Photon. Tech. Lett. **7**, 1231-1233 (1995).

[125] M. Fujita, R. Ushigome, and T. Baba, "Large spontaneous emission factor of 0.1 in a microdisk injection laser," IEEE Photon. Tech. Lett. **13**, 403-405 (2001).

[126] J. M. Gerard, "Solid-state cavity-quantum electrodynamics with self-assembled quantum dots," Single Quantum Dots: Fundamentals, Applications and New Concepts **90**, 269-314 (2003).

[127] T. Baba, "Photonic crystals and microdisk cavities based on GaInAsP-InP system," IEEE J. Sel. Top. Quant. **3**, 808-830 (1997).

[128] W. W. Rigrod, "Gain Saturation and Output Power of Optical Masers," J. Appl. Phys. **34**, 2602, (1963).

[129] A. Tandaechanurat, S. Ishida, D. Guimard, M. Nomura, S. Iwamoto, and Y. Arakawa, "Lasing oscillation in a three-dimensional photonic crystal nanocavity with a complete bandgap," Nat. Photonics **5**, 91-94 (2011).

[130] M. Fujita, S. Takahashi, Y. Tanaka, T. Asano, and S. Noda, "Simultaneous inhibition and redistribution of spontaneous light emission in photonic crystals," Science **308**, 1296-1298 (2005).

[131] G. Bjork, A. Karlsson, and Y. Yamamoto, "Definition of a Laser Threshold," Phys. Rev. A **50**, 1675-1680 (1994).

[132] J. S. Foresi, P. R. Villeneuve, J. Ferrera, E. R. Thoen, G. Steinmeyer, S. Fan, J. D. Joannopoulos, L. C. Kimerling, H. I. Smith, and E. P. Ippen, "Photonic-bandgap microcavities in optical waveguides," Nature **390**, 143-145 (1997).

[133] Y. Zhang, M. Khan, Y. Huang, J. Ryou, P. Deotare, R. Dupuis, and M. Loncar, "Photonic crystal nanobeam lasers," Appl. Phys. Lett. **97**, 051104 (2010).

[134] Y. Gong, B. Ellis, G. Shambat, T. Sarmiento, J. Harris, and J. Vuckovic, "Nanobeam photonic crystal cavity quantum dot laser," Opt. Express **18**, 8781-8789 (2010).

[135] B. H. Ahn, J. H. Kang, M. K. Kim, J. H. Song, B. Min, K. S. Kim, and Y. H. Lee, "One-dimensional parabolic-beam photonic crystal laser," Opt. Express **18**, 5654-5660 (2010).

[136] R. K. Lee, O. J. Painter, B. Kitzke, A. Scherer, and A. Yariv, "Photonic bandgap disk laser," Electron. Lett. **35**, 569-570 (1999).

[137] M. Loncar, T. Yoshie, A. Scherer, P. Gogna, and Y. M. Qiu, "Low-threshold photonic crystal laser," Appl. Phys. Lett. **81**, 2680-2682 (2002).

[138] J. M. Gerard, B. Sermage, B. Gayral, B. Legrand, E. Costard, and V. Thierry-Mieg, "Enhanced spontaneous emission by quantum boxes in a monolithic optical microcavity," Phys. Rev. Lett. **81**, 1110-1113 (1998).

[139] J. Vuckovic, O. Painter, Y. Xu, A. Yariv, and A. Scherer, "Finite-difference time-domain calculation of the spontaneous emission coupling factor in optical microcavities," IEEE J. Quant. Electron. **35**, 1168-1175 (1999).

[140] Y. Huang, J. H. Ryou, R. D. Dupuis, C. Pflugl, F. Capasso, K. W. Sun, A. M. Fischer, and F. A. Ponce, "Optimization of growth conditions for InGaAs/InAlAs/InP quantum cascade lasers by metalorganic chemical vapor deposition," Journal of Crystal Growth **316**, 75-80 (2011).

[141] Y. Zhang, M. W. McCutcheon, I. B. Burgess, and M. Loncar, "Ultra-high-Q TE/TM dual-polarized photonic crystal nanocavities," Opt. Lett. **34**, 2694-2696 (2009).

[142] H. G. Park, J. K. Hwang, J. Huh, H. Y. Ryu, S. H. Kim, J. S. Kim, and Y. H. Lee, "Characteristics of modified single-defect two-dimensional photonic crystal lasers," IEEE J. Quant. Electron. **38**, 1353-1365 (2002).

[143] S. L. McCall, A. F. J. Levi, R. E. Slusher, S. J. Pearton, and R. A. Logan, "Whispering-gallery mode microdisk lasers," Appl. Phys. Lett. **60,** 289-291 (1992).

[144] M. Fujita, A. Sakai, and T. Baba, "Ultrasmall and ultralow threshold GaInAsP-InP microdisk injection lasers: design, fabrication, lasing characteristics, and spontaneous emission factor," IEEE J. Sel. Top. Quant. Electron., **5,** 673-681 (1999).

[145] Z. Liu, J. M. Shainline, G. E. Fernandes, J. Xu, J. Chen, and C. F. Gmachl, "Continuous-wave subwavelength microdisk lasers at $\lambda = 1.53\ \mu$m," Opt. Express, **18,** 19242-19248 (2010).

[146] A. Levi, R. Slusher, S. McCall, T. Tanbun-Ek, D. Coblentz, and S. Pearton, "Room temperature operation of microdisc lasers with submilliamp threshold current," Electron. Lett. **28,** 1010-1012 (1992).

[147] T. D. Lee, P. H. Cheng, J. S. Pan, R. S. Tsai, Y. Lai, and K. Tai, "Far-field emission narrowing effect of microdisk lasers," Appl. Phys. Lett. **72,** 2223 (1998).

[148] L. Mahler, A. Tredicucci, F. Beltram, C. Walther, J. Faist, B. Witzigmann, H. E. Beere, and D. A. Ritchie, "Vertically emitting microdisk lasers," Nat. Photon. **3,** 46-49 (2009).

[149] M. Fujita, and T. Baba, "Microgear laser," Appl. Phys. Lett. **80,** 2051 (2002).

[150] S. H. Kim, S. K. Kim, and Y. H. Lee, "Vertical beaming of wavelength-scale photonic crystal resonators," Phys. Rev. B **73,** 235117 (2006).

[151] D. Zhang, K. Ryu, X. Liu, E. Polikarpov, J. Ly, M. E. Tompson, and C. Zhou, "Transparent, conductive and flexible carbon nanotube films and their application in organic light emitting diodes," Nano Lett. **6,** 1880-1886 (2006).

[152] X. Wang, L. Zhi, and K. M'ullen, "Transparent, conductive graphene electrodes for dye-sensitized solar cells," Nano Lett. **8,** 323-327 (2008).

[153] P. Blake, P. D. Brimicombe, R. R. Nair, T. J. Booth, D. Jiang, F. Schedin, L. A. Ponomarenko, S. V. Morozov, H. F. Gleeson, E. W. Hill, A. K. Geim, and K. S. Novoselov, "Graphene-based liquid crystal device," Nano Lett. **8,** 1704-1708 (2008).

[154] S. Bhaviripudi, X. Jia, M.S. Dresselhaus, and J. Kong, "Role of kinetic factors in chemical vapor deposition synthesis of uniform large area graphene using copper catalyst," Nano Lett. **10,** 4128-4133 (2010).

[155] A. Reina, X. Jia, J. Ho, D. Nezich, H. Son, V. Bulovic, M. S. Dresselhaus, and J. Kong. "Large area, few-layer graphene films on arbitrary substrates by chemical vapor deposition." Nano Lett. **9,** 30-35 (2008).

[156] S. Kita, K. Nozaki, and T. Baba, "Refractive index sensing utilizing a cw photonic crystal nanolaser and its array configuration", Opt. Express, **16**, 8174-8180 (2008).

[157] T. Yoshie, A. Scherer, J. Hendrickson, G. Khitrova, H. M. Gibbs, G. Rupper, C. Ell, O. B. Shchekin, and D. G. Deppe, "Vacuum Rabi splitting with a single quantum dot in a photonic crystal nanocavity," Nature **432**, 200-203 (2004).

[158] E. Yablonovitch, T. J. Gmitter, R. D. Meade, A. M. Rappe, K. D. Brommer, and J. D. Joannopoulos, "Donor and Acceptor Modes in Photonic Band-Structure," Phys. Rev. Lett. **67**, 3380-3383 (1991).

[159] B. Temelkuran, E. Ozbay, J. P. Kavanaugh, G. Tuttle, and K. M. Ho, "Resonant cavity enhanced detectors embedded in photonic crystals," Appl. Phys. Lett. **72**, 2376-2378 (1998).

[160] M. A. Shapiro, W. J. Brown, I. Mastovsky, J. R. Sirigiri, and R. J. Temkin, "17 GHz photonic band gap cavity with improved input coupling," Phys. Rev. Spec. Top-Ac. **4**, 042201 (2001).

[161] E. I. Smirnova, A. S. Kesar, I. Mastovsky, M. A. Shapiro, and R. J. Temkin, "Demonstration of a 17-GHz, high-gradient accelerator with a photonic-band-gap structure," Phys. Rev. Lett. **95**, 074801 (2005).

[162] E. Di Gennaro, S. Savo, A. Andreone, V. Galdi, G. Castaldi, V. Pierro, and M. R. Masullo, "Mode confinement in photonic quasicrystal point-defect cavities for particle accelerators," Appl. Phys. Lett. **93**, 164102 (2008).

[163] C. Jin, B. Cheng, B. Man, Z. Li, and D. Zhang, "Two-dimensional dodecagonal and decagonal quasiperiodic photonic crystals in the microwave region," Phys. Rev. B **61**, 10762-10767 (2000).

[164] J. M. Raimond, M. Brune, and S. Haroche, "Colloquium: Manipulating quantum entanglement with atoms and photons in a cavity," Rev. Mod. Phys. **73**, 565-582 (2001).

[165] A. Wallraff, D. I. Schuster, A. Blais, L. Frunzio, R. S. Huang, J. Majer, S. Kumar, S. M. Girvin, and R. J. Schoelkopf, "Strong coupling of a single photon to a superconducting qubit using circuit quantum electrodynamics," Nature **431**, 162-167 (2004).

[166] A. Petosa, A. Ittipiboon, Y. M. M. Antar, D. Roscoe, and M. Cuhaci, "Recent advances in dielectric-resonator antenna technology," IEEE Antennas Propag. **40**, 35-48 (1998).

[167] M. J. R. Previte, and C. D. Geddes, "Fluorescence microscopy in a microwave cavity," Opt. Express **15**, 11640-11649 (2007).

[168] Y. Zhang, I. Bulu, T. Botto, B. Levitt, J. Shah, W. M. Tam, and M. Loncar, "TM-Polarized air-band-mode photonic crystal cavities at microwave frequency for cQED applications," in International Conference on Photonic and Electromagnetic Crystal Structure (Granada, 2010).

[169] J. D. Joannopoulos, and J. N. Winn, Photonic crystals: molding the flow of light (Princeton University Press, 2008).

[170] M. Galli, S. L. Portalupi, M. Belotti, L. C. Andreani, L. O'Faolain, and T. F. Krauss, "Light scattering and Fano resonances in high-Q photonic crystal nanocavities," Appl. Phys. Lett. 94, 071101 (2009).

[171] Lj. Babic, and M. J. A. de Dood, "Interpretation of Fano lineshape reversal in the reflectivity of photonic crystal slabs", Opt. Express **18**, 26569-26582 (2010).

[172] U. Durig, D. W. Pohl, and F. Rohner, "Near-Field optical-Scanning microscopy," J. Appl. Phys. **59**, 3318-3327 (1986).

[173] L. Lalouat, B. Cluzel, P. Velha, E. Picard, D. Peyrade, J. P. Hugonin, P. Lalanne, E. Hadji, and F. de Fornel, "Near-field interactions between a subwavelength tip and a small-volume photonic-crystal nanocavity," Phys. Rev. B **76**, 041102 (2007).

[174] A. Faraon, I. Fushman, D. Englund, N. Stoltz, P. Petroff, and J. Vuckovic, "Coherent generation of non-classical light on a chip via photon-induced tunnelling and blockade," Nature Phys. **4**, 859-863 (2008).

[175] M. Soljacic and J. D. Joannopoulos, "Enhancement of nonlinear effects using photonic crystals," Nature Mater. **3**, 211-219 (2004).

[176] F. Raineri, C. Cojocaru, P. Monnier, A. Levenson, R. Raj, C. Seassal, X. Letartre, and P. Viktorovitch, "Ultrafast dynamics of the third-order nonlinear response in a two-dimensional InP-based photonic crystal," Appl. Phys. Lett. **85**, 1880 (2004).

[177] M. Liscidini, and L. Andreani, "Highly efficient second-harmonic generation in doubly resonant planar microcavities," Appl. Phys. Lett. **85**, 1883-1885 (2004).

[178] J. Bravo-Abad, A. Rodriguez, P. Bermel, S. G. Johnson, J. D. Joannopoulos, and M. Soljacic, "Enhanced nonlinear optics in photonic-crystal microcavities," Opt. Express **15**, 16161-16176 (2007).

[179] I. B. Burgess, A. W. Rodriguez, M. W. McCutcheon, J. Bravo-Abad, Y. Zhang, S. G. Johnson, and M. Loncar, "Difference-frequency generation with quantum-limited efficiency in triply-resonant nonlinear cavities," Opt. Express **17**, 9241-9251 (2009)

[180] M. W. McCutcheon, J. F. Young, G. W. Rieger, D. Dalacu, S. Frederick, P. J. Poole, and R. L. Williams, "Experimental demonstration of second-order processes in photonic crystal microcavities at submilliwatt excitation powers," Phys. Rev. B. **76**, 245104 (2007).

[181] M. W. McCutcheon, D. E. Chang, Y. Zhang, M. D. Lukin, and M. Loncar, "Broad-band spectral control of single photon sources using a nonlinear photonic crystal cavity," arXiv:0903.4706, submitted (2009).

[182] S. G. Johnson, A. Mekis, S. Fan, and J. D. Joannopoulos, "Multipole-cancellation mechanism for high-Q cavities in the absence of a complete photonic band gap," Appl. Phys. Lett. **78**, 3388-3390 (2001)

[183] Y. Wakayama, A. Tandaechanurat, S. Iwamoto, and Y. Arakawa, "Design of high-Q photonic crystal microcavities with a graded square lattice for application to quantum cascade lasers," Opt. Express **16**, 21321-21332 (2008)

[184] L. C. Andreani and D. Gerace, "Photonic-crystal slabs with a triangular lattice of triangular holes investigated using a guided-mode expansion method," Phys. Rev. B **73**, 235114 (2006)

[185] M. Bahriz, V. Moreau, R. Colombelli, O. Crisafulli, and O. Painter, "Design of mid-IR and THz quantum cascade laser cavities with complete TM photonic bandgap," Opt. Express **15**, 5948-5965 (2007)

[186] L. A. Dunbar, V. Moreau, R. Ferrini, R. Houdre, L. Sirigu, G. Scalari, M. Giovannini, N. Hoyler, and J. Faist, "Design, fabrication and optical characterization of quantum cascade lasers at terahertz frequencies using photonic crystal reflectors," Opt. Express **13**, 8960-8968 (2005)

[187] S. Hofling, J. Heinrich, H. Hofmann, M. Kamp, J. P. Reithmaier, A. Forchel, and J. Seufert, "Photonic crystal quantum cascade lasers with improved threshold characteristics operating at room temperature," Appl. Phys. Lett. **89**, 191113 (2006).

[188] M. Loncar, B. G. Lee, L. Diehl, M. A. Belkin, F. Capasso, M. Giovannini, J. Faist, and E. Gini, "Design and fabrication of photonic crystal quantum cascade lasers for optofluidics," Opt. Express **15**, 4499-4514 (2007).

[189] Y. Zhang and M. Loncar, "Sub-micron diameter micropillar cavities with high Quality factors and ultra-small mode volumes," Opt. Lett. **34**, 902-904 (2009).

[190] J. Chan, M. Eichenfield, R. Camacho, and O. Painter, "Optical and mechanical design of a "zipper" photonic crystal optomechanical cavity," Opt. Express **17**, 3802-3817 (2009)

[191] K. Hennessy, C. Högerle, E. Hu, A. Badolato, and A. Imamoglu, "Tuning photonic nanocavities by atomic force microscope nano-oxidation," Appl. Phys. Lett. **89**, 041118 (2006).

[192] S. Singh, "Nonlinear optical materials" in *Handbook of laser science and technology, Vol. III: Optical Materials, Part I*, M. J. Weber eds. (CRC Press 1986).

Author List

The following authors contributed to Chapter 1:
Changlin Li.

The following authors contributed to Chapter 2:
Ian Frank.

The following authors contributed to Chapter 4:
Mughees Khan, Parag Deotare, Yong Huang, Jae-Hyun Ryou, Russell Dupuis, Yi Song, Jing Kong.

The following authors contributed to Chapter 5:
Irfan Bulu, Tancredi Botto, Wai-Ming Tam, Ben Levitt.

The following authors contributed to Chapter 6:
Ian Burgess, Murray McCutcheon.